# Heat Transfer Measurements in Subsonic Transitional Boundary Layers

C.J. Hogendoorn

Dit proefschrift is goedgekeurd door de promotoren:

   prof.dr.ir. A.A. van Steenhoven
   prof.dr.ir. M.E.H. van Dongen

Copromotor:

   dr.ir. H.C. de Lange

# Heat Transfer Measurements in Subsonic Transitional Boundary Layers

PROEFSCHRIFT

ter verkrijging van de graad van doctor aan de
Technische Universiteit Eindhoven, op gezag van
de Rector Magnificus, prof.dr. M. Rem,
voor een commissie aangewezen door het College
van Dekanen in het openbaar te verdedigen op
woensdag 21 mei 1997 om 16.00 uur

door

Cornelis Johannes Hogendoorn

geboren te Rotterdam.

*Hoe groot zijn Uw werken, o HEERE! Gij hebt ze alle met wijsheid gemaakt.*
*Ps 104:24a*

*aan Trijntje*
*aan mijn ouders*

# Contents

# Chapter 1

# Introduction

About 60 years after its introduction, the gas turbine is a widely applied engine nowadays [*Mayle*, 1991]. Gas turbines are compact power sources with a high conversion efficiency, which makes application very successful in a range of operation conditions. As a result of technological development the performance has been strongly improved in recent years. The thermodynamic state inside the gas turbine is becoming more and more extreme, particularly with respect to gas temperatures. Higher gas temperatures contributes to higher efficiencies and a higher specific power production. At the entrance of the turbine, behind the combustion chamber (figure 1.1), temperatures of $1400^{\circ}C$ no longer are exceptional.

One of the major difficulties in this hot gas flow is the heat transfer rate
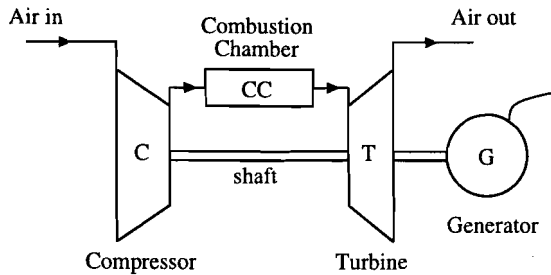


*Figure 1.1: Schematic representation of a gas turbine.*

to turbine blades. The thermal load due to the highly convective flows is very large, whereas the permitted blade temperature is limited. To control the blade temperature a good prediction of heat transfer is essential. This is very difficult as it is governed by a number of flow phenomena. The flow phenomena around turbine blades (left-hand figure 1.2) includes horse-shoe vortices, blade wakes, secondary flow, boundary layer transition, tip flow, film cooling, etc. Nevertheless, the heat transfer towards turbine blades can be divided into two zones: an

end wall region and a midspan region [*Simoneau and Simon*, 1993]. The midspan
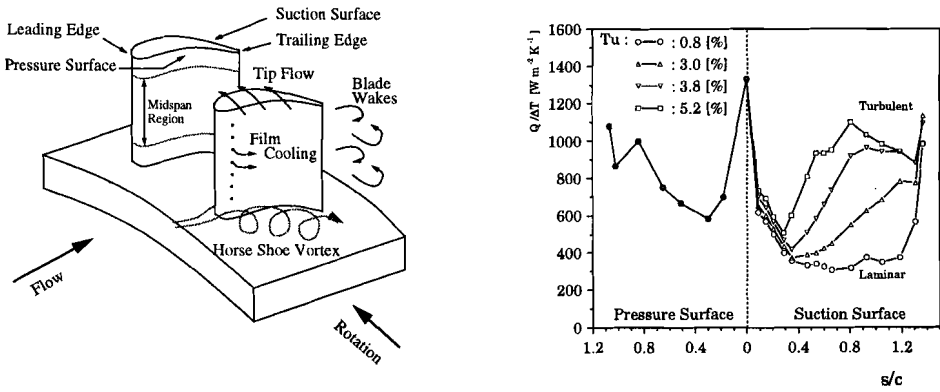


*Figure 1.2: Different flow phenomena involved in the turbine gas path (left-hand). The featuring heat transfer rate in the midspan region [Consigny and Richards, 1982] (right-hand). Here, s is the coordinate along the blade starting from leading edge, while c is the straight length between the leading and trailing edge.*

region covers about 50 to 75 percent of the blade span. In this region the end wall boundary layer has a negligible influence and the flow can be considered two-dimensional. The heat transfer process in this area is dominated by the transition of the boundary layer from a laminar to a turbulent type. The heat transfer rate is strongly related to the character of the boundary layer. For a turbulent boundary layer the heat transfer can easily be three times higher than that of the laminar boundary layer. This is shown in figure 1.2 (right-hand), which represents the featuring heat transfer rate over the blade length. Another aspect that turns up is that transition depends on the free stream turbulence level. A higher turbulence level leads to earlier transition. An accurate prediction of the transition start and length is still not possible because good transition models are lacking [*Hirsch*, 1994]. Many experiments are required to investigate the individual influence of free stream turbulence at higher intensities, pressure gradients and compressibility.

This thesis starts with the investigation of the influence of high free stream turbulence levels and compressibility on boundary layer transition. The need for experiments will be pointed out at the end of chapter 2. This chapter starts with the boundary layer transition process in general. Different transition mechanisms are discussed, with the emphasis on the so-called bypass transition scenario. This is the main mechanism to break down at higher free stream turbulence levels. The breakdown, which is the start of transition, leads to the generation of small turbulent areas that are convected with the main flow. These are the so-called turbulent spots. The specific features of these spots are also discussed in this

chapter. A phenomenological description of these spots together with the mutual interaction lead to a widely used transition model. For the practical application of this model more physical information is required. The latter is missing for the flow regime discussed.

In chapter 3 it will be shown that the atmospheric wind tunnel as an experimental facility is inadequate to study boundary layer transition at higher subsonic Mach numbers and that the Ludwieg tube is more suitable for this research. This experimental facility has not been applied yet in any subsonic/transonic boundary layer transition research at high free stream turbulence levels. Therefore, the performance of the Ludwieg tube was closely examined with respect to available test times, accuracy of reproduction, variation of flow conditions, available ranges for Reynolds number, Mach number and free stream turbulence level, etc.

Due to the relatively low heat flux levels in the Ludwieg tube an improved method to measure transient heat fluxes with thin film gauges is presented in chapter 4. A design strategy of these gauges is also discussed in this chapter.

In chapter 5 the preliminary results with respect to boundary layer transition at different Mach numbers and turbulence levels are discussed. Chapter 6 finishes with conclusions and recommendations.

# Chapter 2

# Boundary Layer Transition

## 2.1 Introduction

During the transition from a laminar to turbulent boundary layer many properties change. A general sketch of a transitional boundary layer on a flat plate is shown in figure 2.1. The initial boundary layer is laminar. At the start of
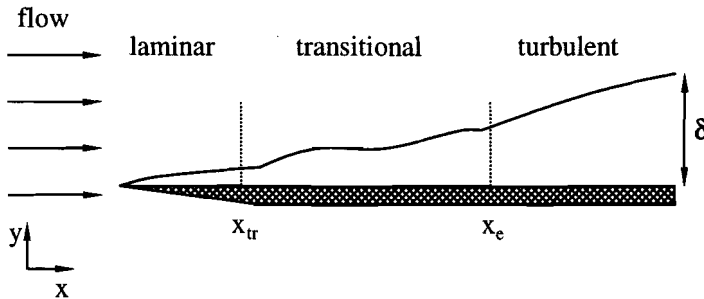


Figure 2.1: Schematic figure of a transitional boundary layer at a flat plate

transition, turbulent spots appear that give rise to an 'intermittent' boundary layer behaviour. Initially, the amount of turbulence is small but it increases until a fully turbulent boundary layer is obtained at the end of transition. The turbulent spots significantly influence parameters like shape factor, averaged velocity profile and skin friction. According to *Dhawan and Narasimha* [1958] the mean flow in the boundary layer during transition is best described through the distribution of the intermittency, $\gamma$. The intermittency is the fraction of time during which the flow over a point on the surface is turbulent. It is zero at the beginning and equal to one where a fully turbulent boundary layer is obtained. Zero percent intermittency defines the start of transition, with subscript $tr$, while an intermittency of 0.99 is defined as the end of transition, indicated with subscript $e$ (figure 2.2). As the relations for both the laminar and turbulent boundary layer properties are known, the resulting 'properties' in the transitional part can be
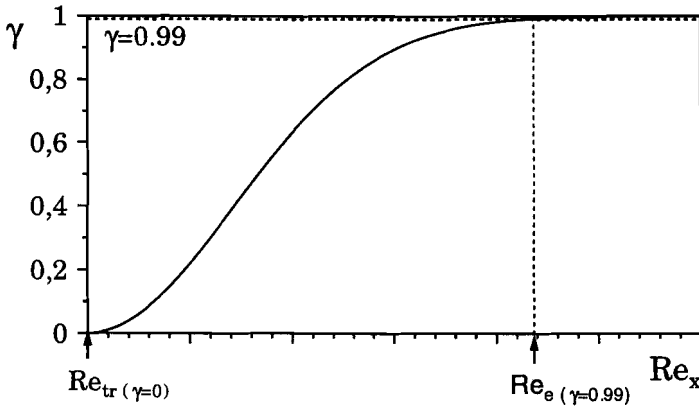
*Figure 2.2: Intermittency distribution in stream wise direction of a transitional boundary layer. Here $Re_x$ stands for the local Reynolds number.*

computed if the start and distribution of intermittency is known {*Dhawan and Narasimha*, 1958].

This chapter starts with several scenarios that can cause the onset (=start) of transition resulting in so-called turbulent spots. This spot is a turbulent structure embedded in a laminar environment, which grows in a longitudinal and span-wise direction causing an increasing turbulent part (intermittency) downstream. Finally, the different spots merge resulting in a fully turbulent boundary layer. The properties of the turbulent spot are described in the third section. Based on the integral effect of turbulent spots an intermittency model can be derived that is widely used. This model is discussed in the fourth section. In the fifth section the determinative parameters (like free stream turbulence, etc.) for boundary layer transition in turbine flows are discussed. The individual effect of each parameter on spot parameters, onset and length of transition is dealt with. This chapter ends with conclusions concerning the research that still is required to improve the present results with respect to the prediction of transition.

## 2.2    Transition scenarios

The onset of boundary layer transition can be divided into three different scenarios: secondary instability or natural transition, bypass transition, and the separated-flow transition scenario. In both the natural and bypass transition types the breakdown of the non-linear structure ends in the birth of a turbulent spot.

## Secondary Instability Scenario
In flows with free stream turbulence intensities lower than 1%, the secondary instability scenario is the normal way to come about. It characterizes a number of succeeding phenomena, observed after the critical boundary layer Reynolds number has been exceeded (figure 2.3). After the origination of two-dimensional Tollmien-Schlichting (TS) waves [Reshotko, 1984] a linear amplification of the small amplitude instability waves is the second stage [Arnal, 1994], followed by the formation of non-linear Λ-vortices [Hama et al., 1957], resulting in a non-linear vortex breakdown [Klebanoff et al., 1962]: the origination of a turbulent spot.

Two different breakdown types have been recognized [Kachanov, 1994]: the well ordered peak-valley pattern of the K-breakdown and the staggered pattern of the N-breakdown. The K-breakdown is a result of a rapid amplification of the fundamental harmonic mode, while the N-breakdown is characterized by the amplification of the three-dimensional sub-harmonics of the fundamental wave.



1 : Tollmien-Schlichting waves
2 : Λ-vortices
3 : Non-linear vortex loops
4 : Turbulent spots
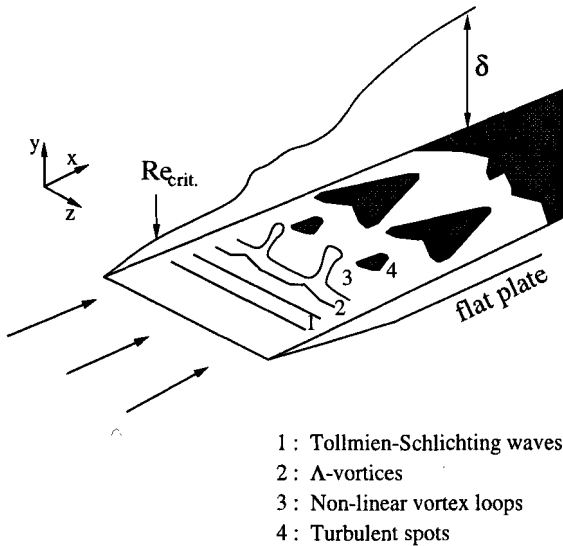
*Figure 2.3: Sketch of different phenomena occurring during natural transition.*

## Bypass Transition Scenario
Another class of transition is called *bypass* transition. The mechanism is connected to a direct non-linear laminar flow breakdown due to external disturbances [Kachanov, 1994]. This mechanism still is not fully understood and insights are mainly based on phenomenological observations.

The boundary layer is sensitive to disturbances either from the region outside the boundary layer or from the wall. Disturbances grow in those parts of the bound-

ary layer that are most sensitive to the disturbances. In the description of this process it is useful to consider the linear and weakly non-linear disturbances as being composed of a dispersive wave portion and an advective part. The dispersive wave portion grows or decays according to Tollmien-Schlichting instability theory, and the advective or transient portion travels at approximately the local mean velocity [*Breuer and Landahl*, 1990]. *Breuer and Landahl* [1990] found that for larger disturbances in the three-dimensional flow the advective portion grows much faster than the wave portion.

Stronger three-dimensional perturbations lead to the 'lift-up' effect. This process is illustrated with a numerical simulation as seen in figure 2.4. Due to an initial eddy (e.g. from free stream) low speed fluid near to the wall is pushed up and high speed fluid is pulled down. Thus a high velocity region (solid contour lines) is created in front of a low velocity region (gray contour lines). This structure is tilted over due to the mean shear in the boundary layer, and is stretched, creating an internal shear layer. The shear layer structure stretches and the dis-
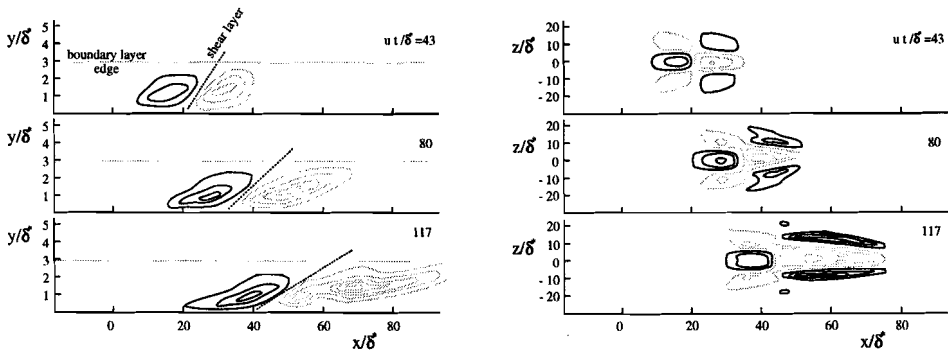


*Figure 2.4: Contours of the stream-wise perturbation velocity in x,y-plane at centreline (left-hand) and in x,z-plane at $y/\delta^*=1.05$ (right-hand). Contour spacing is 0.02 u. (solid lines: positive contours, gray lines: negative contours, with $\delta^*$ the displacement thickness) [Breuer and Landahl, 1990].*

turbance intensifies[1]. The sharp shear layer roll up gives a situation similar to the first spike stage observed in the breakdown of large-amplitude disturbances in the secondary instability scenario. After the first sign of breakdown the disturbance quickly develops into a turbulent spot. Direct numerical simulations [*Henningson et al.*, 1993, *Henningson et al.*, 1994] and experiments [*Breuer and Haritonidis*, 1990] show that the largest growth is always achieved for disturbances with very low stream wise wave number, i.e. streaky structures. The disturbance growth and breakdown in this transition scenario takes place at a much shorter time interval than that of the secondary instability scenario [*Henningson et al.*, 1993].

---

[1] For an initial situation of a low speed area in front of a high speed area, caused by a counter rotating initial eddy, no internal shear layer is generated and this thus does not result in bypass transition [*Breuer and Landahl*, 1990].

The term bypass transition emphasizes the fact that in this scenario the growth of T.S. waves and their subsequent secondary instability scenario is bypassed. The bypass route to turbulence in boundary layer flows is usually related to the transition at free stream turbulence levels above about 1%. It therefore is the common mode for transition in gas turbine engines.

**Separated Flow Transition**

A third mechanism is transition due to a laminar separated boundary layer [*Mayle*, 1991]. Separation is usually caused by a disturbance at the surface or due to a strong adverse pressure gradient. The turbulent boundary layer may reattach on the surface and a separation bubble is formed.

## 2.3   Turbulent spot

It was Emmons (1951) who discovered a turbulent spot by accident during a lecture and initiated a new view with respect to the laminar-turbulent transition zone [*Narasimha*, 1985]. Almost 70 years earlier Reynolds (1883) already observed flashes of turbulence in pipe flow. One of the first experiments that provided more clarity was performed by *Schubauer and Klebanoff* [1955].

A turbulent spot is a wedge-shaped patch of turbulence in a laminar environment (figure 2.5). In an incompressible flow without pressure gradient, the sides of the spot are straight and the spreading angle attains a constant value. The
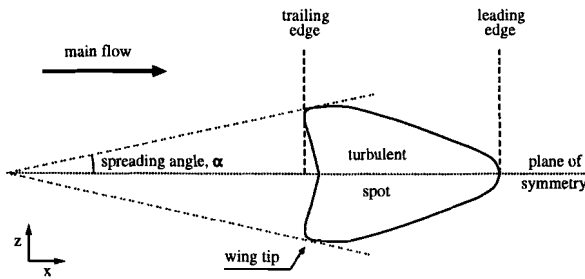


*Figure 2.5: Plane view of a turbulent spot with the definition of the leading and trailing edge, spreading angle, wing tips and plane of symmetry.*

trailing edge is slightly concave. For adversed pressure gradient flow the concavity is more expressed, whereas it is completely absent for strong favourable pressure gradients [*Katz et al.*, 1990]. Figure 2.6 shows a cross-section at the plane of symmetry. At the leading edge a characteristic overhang is present at about 1/4 of the total spot height. The total spot height corresponds with the empirical relation for a fully turbulent boundary layer on a flat plate.

An important feature is the self-similarity of the spot; from a certain size the shape of the spot is preserved. In zero pressure gradient flow, the trailing and
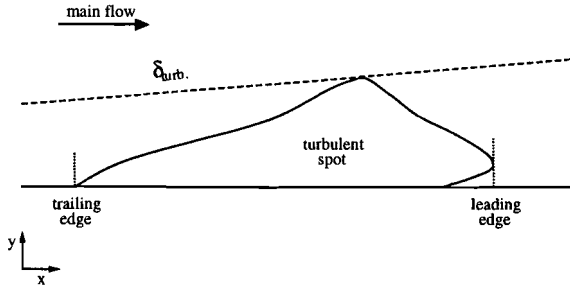
*Figure 2.6: A cross-section of a turbulent spot at the plane of symmetry.*

leading edge velocities are 0.88 and 0.5 times the free-stream velocity, respectively [*Schubauer and Klebanoff*, 1955], while the spot is bounded by an intermittent region with the outer limit given by a spreading angle of about $10°$ [*Wygnanski et al.*, 1976]. All these parameters strongly depend on different flow parameters. In particular the pressure gradient has a large impact on the expansion in all directions. This effect will be discussed later. Behind the trailing edge of the spot, a stable flow is observed (figure 2.7), called the 'calmed region' [*Gad-el Hak et al.*, 1981]. Hot wire [*Schubauer and Klebanoff*, 1955] and heat transfer measurements
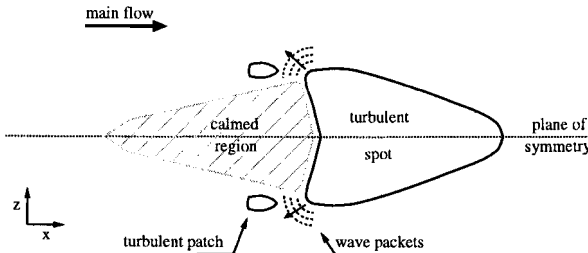


*Figure 2.7: Plan-view sketch of the calmed region behind the trailing edge of a turbulent spot.*

[*Clark et al.*, 1994] show the typical exponential-like decay for velocity and heat transfer rate. In the calmed region the velocity profile changes smoothly from a turbulent velocity profile inside the spot [*Wygnanski et al.*, 1976, *Cantwell et al.*, 1978] to a laminar profile 'after' the calmed region. During this recovery trail the profile is fuller compared to the velocity profile in the surroundings and more stable [*Gostelow*, 1995]. In the interior of the spot larger structures are present ejecting fluid entrained at the plane of symmetry in the span-wise direction outward at the wing tips [*Cantwell et al.*, 1978, *Seifert et al.*, 1994]. For the case of a zero pressure gradient, *Wygnanski et al.* [1979] observe coherent oblique wave packets behind the spot outside the calmed region. The largest amplitudes in

the wave packets mostly occur behind the tips of the spot. For flows with adversed pressure gradients wave packets propagate along with the leading edge of the spot [*van Hest*, 1996]. It is assumed that the shape of the spot, the rate of growth and its spreading angle are related to these wave packets. At Reynolds numbers that are sufficiently high to allow disturbances to grow, the wave packets can lead to new breakdowns and give rise to so-called turbulent patches [*Glezer et al.*, 1989]. These patches are new spots behind the wing tips of the 'parent' spot (figure 2.7). A turbulent patch generated by the breakdown of the waves increases in size, while it propagates downstream eventually amalgamating with the parent spot. The generation of patches at high Reynolds number (turbine-like conditions) is unknown.

## 2.4   Intermittency model

*Emmons* [1951] constructed an intermittency model for a transitional boundary layer on the basis of the increasing intermittent fraction caused by the growth of turbulent spots. A turbulent spot initiated at point $P_0$ (left-hand figure 2.8) covers the so-called propagation cone in the x,z,t-space. The intermittency at point $P$ (right-hand figure 2.8) is determined by the dependency volume (mirrored propagation cone). The cone of dependence is the collection of all points upstream of $P$ in the x,z,t-space that are sources of turbulent spots, which will pass over $P$. The overlap of spots was taken into account too.
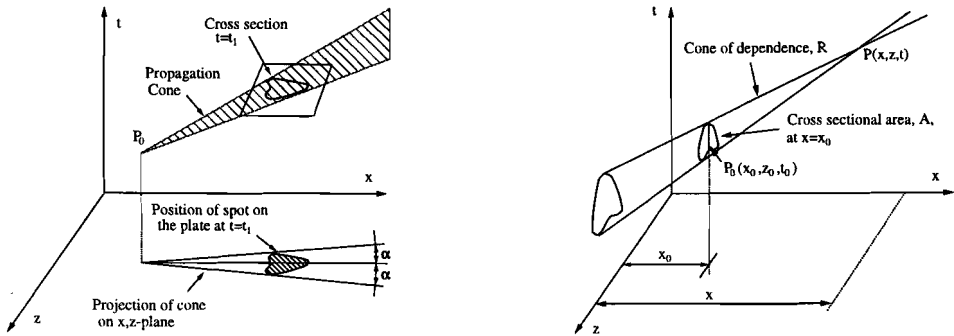


*Figure 2.8: Propagation of a turbulent spot in $x, z, t$-space (left-hand) and the dependence volume of point $P(x, z, t)$ (right-hand).*

*Steketee* [1955] found the derivation of this model 'rather complicated' and proposed a more 'straightforward' derivation to come to the same result. In the work of *Chen and Thyson* [1971] the dependence volume $R$ was written in terms of spot parameters. They used the work of *Dhawan and Narasimha* [1958] in which the spots are proposed to be generated on one line and they approximated

the projected spot shape with a triangle.

This work resulted in the useful intermittency model [*Mayle*, 1991]:

$$\gamma(Re_x) = 1 - exp\left[-\hat{n}\sigma(Re_x - Re_{tr})^2\right] \quad \text{for} \quad Re_x > Re_{tr} \qquad (2.1)$$

where $Re_{tr}$ is the Reynolds number at the start of the transition, $\hat{n}$ the dimensionless spot formation rate given by

$$\hat{n} = n\nu^2/u^3 \qquad (2.2)$$

where $n$ is the turbulent spot production rate, $u$ is the free stream velocity, $\nu$ is the kinematic viscosity and $\sigma$ is the spot propagation parameter given by

$$\sigma = tan(\alpha)\left[C_{te}^{-1} - C_{le}^{-1}\right] \qquad (2.3)$$

where $C_{te}$ and $C_{le}$ are the ratios of trailing and leading edge velocities to the free stream velocity, respectively.

## 2.5   Governing parameters for transition in turbine flow

Boundary layer transition in general can be influenced by a number of parameters [*Abu-Ghannam and Shaw*, 1980][*Reshotko*, 1984]. Factors like free stream turbulence, pressure gradient, Reynolds number, Mach number, acoustic radiation, surface roughness, surface temperature, surface curvature, film cooling and periodic unsteady wake passing, play their individual role. The latter two effects are introduced artificially and require special modelling and will not be discussed here[2]. However, *Mayle* [1991] showed that due to the high free stream turbulence level in turbo-machinery (5% to 10%), the free stream turbulence strongly dominates the effects of surface roughness, surface temperature, surface curvature[3] and acoustic radiation. The effect of the Reynolds number has not yet been investigated in any detail. According to the work of *Stetson and Kimmel* [1993] it seems that in the case of high free stream turbulence the latter is dominant. Hence, the following parameters: free stream turbulence, pressure gradient and Mach number seem to play a part in boundary layer transition in turbo-machinery

---

[2]The effect of unsteady wake passing can be viewed as a periodic flow with higher free stream turbulence level (15% to 20%). This can be described with an extended intermittency model [*Mayle and Dullenkopf*, 1990].

   Film cooling can be seen as a source of high turbulence within the downstream developing boundary layer which effects a turbulent boundary layer [*Mayle*, 1991]. Due to strong acceleration the flow can become laminar again. Usually this situation occurs for film-cooled blades in the first turbine stage.

[3]Pressure gradients induced by surface curvatures, contraction or area cross-sectional area reduction must be taken into account.

flow. The individual and combined effects will be discussed next.

In order to obtain functional relations for the intermittency model (equation 2.1) attention will be focused on empirical relations for the effect of the free stream turbulence level both on transition onset and transition length (in terms of $\hat{n}\sigma$). A useful physical parameter related to the stability of the boundary layer is the Reynolds number based on the boundary layer momentum thickness $\Theta$ at start of transition $Re_{\Theta tr}$. $Re_{tr}$ is related to $Re_{\Theta tr}$ via:

$$Re_{\Theta tr} = 0.664\sqrt{Re_{tr}} \tag{2.4}$$

### Influence of free stream turbulence

A lot of work has been performed to study the influence of free stream turbulence on incompressible boundary layer transition without pressure gradient. The work has mainly been focused on the turbulence intensity and hardly on the structure [*Mayle*, 1991]. In literature different empirical relations have been determined based on collected experimental data. The relation presented by *Abu-Ghannam and Shaw* [1980] uses the Tollmien-Schlichting limit of stability ($Re_{\Theta} = 163$) as a lower limit, resulting in

$$Re_{\Theta tr} = 163 + \exp(6.91 - Tu) \tag{2.5}$$

where $Tu$ is the free stream turbulence level in percents. According to *Mayle* [1991] this lower limit is irrelevant because bypass transition is completely independent from the Tollmien-Schlichting instability. Values of 100 for $Re_{\Theta}$ are not uncommon. He came to the relation:

$$Re_{\Theta tr} = 400 Tu^{-5/8} \tag{2.6}$$

This relation seems to correspond very well with data over a wide range of free stream turbulence levels, as can be seen in figure 2.9. Various other relations are available [*Abu-Ghannam and Shaw*, 1980, *Johnson*, 1994] with more or less comparable predictions.

Different definitions are used to characterize the length of the transition zone. A convenient parameter combination is directly obtained from the intermittency model (equation 2.1) in which the term ($\hat{n}\sigma$) determines the transition length. Some experimental fits for different free stream turbulence levels are presented in figure 2.10 (left-hand). The best fit yields the corresponding spot production rate. The relation between spot production rate and free stream turbulence level is drawn in figure 2.10 (right-hand) with the best fit given by:

$$\hat{n}\sigma = 1.5 \times 10^{-11} Tu^{7/4} \tag{2.7}$$

Another way is to use direct length scales like $\lambda$, which is the distance between the intermittencies of 0.25 and 0.75, or the transition length $L_t$, the length between intermittencies of 0 and 0.99. However, these length scales can directly be written
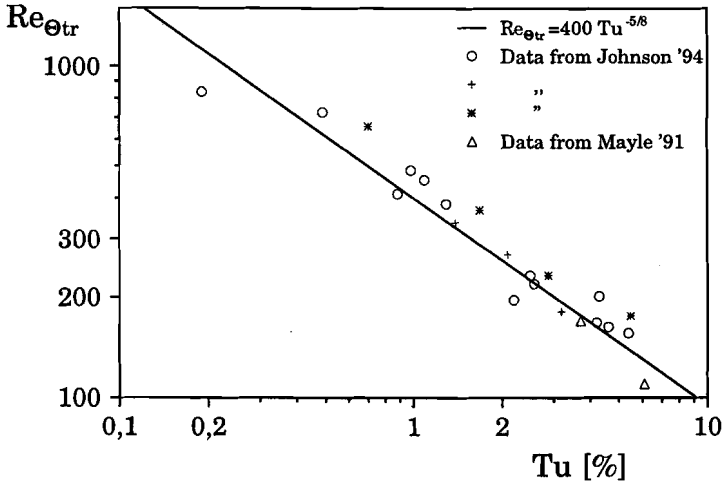
*Figure 2.9: Momentum thickness Reynolds number at the start of transition as a function of free stream turbulence level for an incompressible flow with zero pressure gradient.*

in terms of the spot production rate $\hat{n}\sigma$, using the intermittency model (equation 2.1). *Dhawan and Narasimha* [1958] found a logarithmic relation between $Re_{tr}$ and $Re_\lambda$ given by

$$Re_\lambda = 5Re_{tr}^{0.8} \tag{2.8}$$

**Turbulence scales**

In experiments the free stream turbulence level frequently is artificially created by means of a square plain grid. The grid usually consists of equidistant rods. The rod distance is referred to as the mesh size. *Hall and Gibbings* [1972] showed the importance of grid mesh size during the onset of transition (figure 2.11). *Mayle* [1991] suggested that this probably is the principal reason for the scatter in figure 2.9. He found the maximum difference in onset of transition to be $\pm$ 25% in the stream-wise location This is the difference between upper and lower line in figure 2.11 transformed to stream-wise location via relation 2.4. In spite of this significant effect, the scale of turbulence has not yet been a subject of study.

**Effect of pressure gradient**

The spot growth and thus the transition length is strongly influenced by pressure gradients. In experiments the parameter $\lambda_\Theta$ is frequently used. This is a convenient parameter to describe the pressure gradient and is defined as (at the start of transition)

$$\lambda_\Theta = \frac{\Theta^2}{\nu} \frac{du}{dx} \tag{2.9}$$
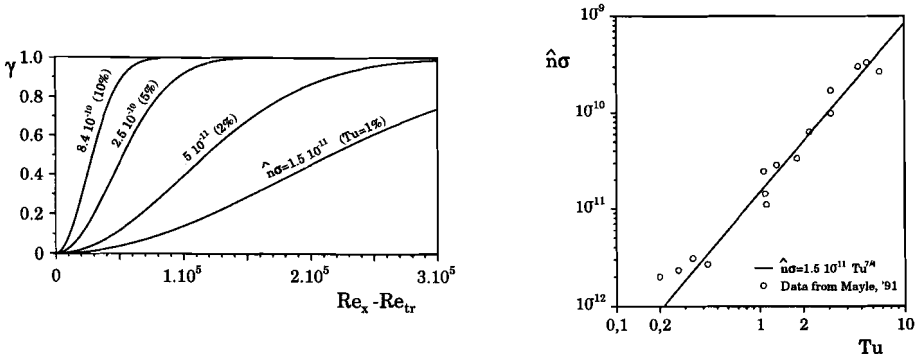
Figure 2.10: Intermittency distribution for different free stream turbulence levels or spot production rates $\hat{n}\sigma$, according to relation 2.7 (left-hand). Experimental spot production rate versus free stream turbulence levels with best fit (right-hand) [Mayle, 1991] (incompressible flow without pressure gradient).
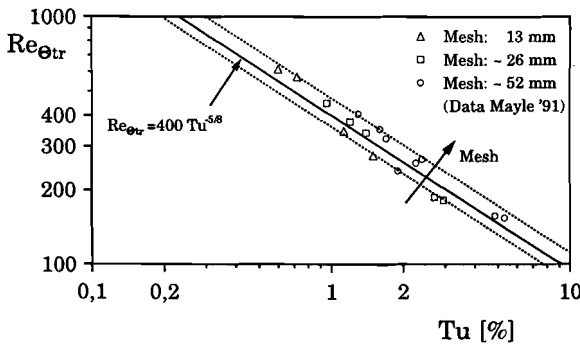


Figure 2.11: Onset of transition for different grid meshes [Hall and Gibbings, 1972, Mayle, 1991] (incompressible flow with zero pressure gradient).

The overall tendency is that an increasing pressure gradient causes an increasing trailing edge velocity, whereas the leading edge velocity remains more or less unchanged (figure 2.12). The spreading angle and growth in height decreases. Also, the relative size of the calmed region diminishes. For very strong favourable pressure gradients *Clark et al.* [1994] show that the trailing edge comes close to the leading edge velocity. Adversed pressure gradients show an opposite effect. The decreasing leading edge velocity causes an increasing velocity difference between the two edges, resulting in a stronger spot growth. The span-wise growth also increases significantly [*van Hest et al.*, 1994] (figure 2.12).

Furthermore, the transition onset is influenced. *Abu-Ghannam and Shaw* [1980] collected different experimental results and proposed a combined relation
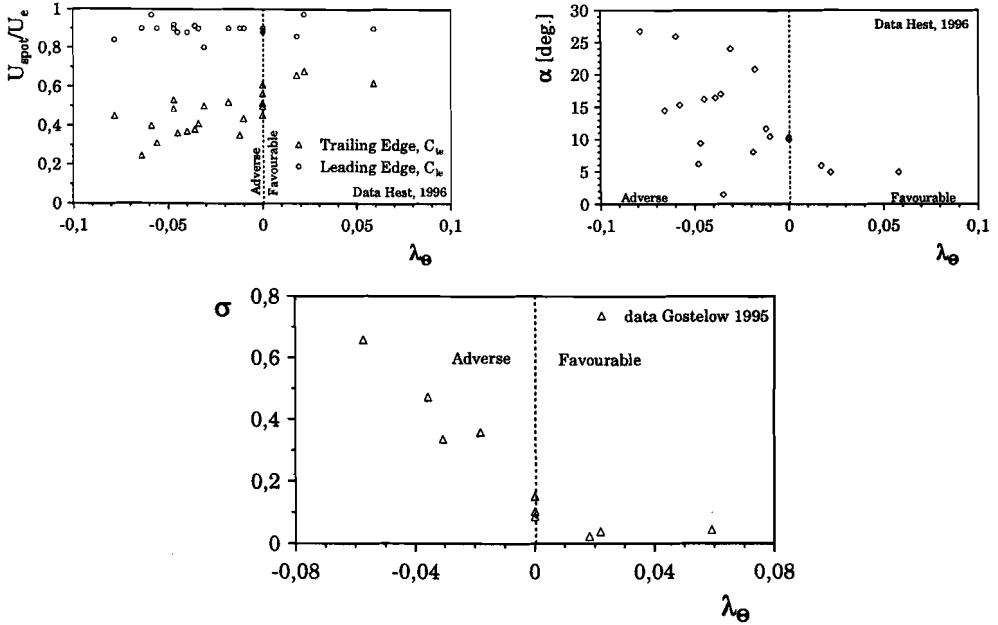
*Figure 2.12: The effect of pressure gradient on spot growth. Upper left-hand figure shows the effect on the spot propagation velocity ($U_e$ is boundary layer edge velocity). Upper right-hand figure shows the effect on the growth angle (data from van Hest [1996]). The lower figure shows the resulting spot propagation parameter $\sigma$ (according to Gostelow et al. [1994]).*

for the influence of free stream turbulence and pressure gradient:

$$Re_{\Theta tr} = 163 + \exp\left(F(\lambda_{\Theta}) - \frac{F(\lambda_{\Theta})}{6.91}Tu\right) \qquad (2.10)$$

where the function $F(\lambda_{\Theta})$ is the relation for adverse or favourable pressure gradients, respectively, given by

$$F(\lambda_{\Theta}) = 6.91 + 12.75\lambda_{\Theta} + 63.64\lambda_{\Theta}^2 \text{ for } \lambda_{\Theta} < 0 \qquad (2.11)$$

and

$$F(\lambda_{\Theta}) = 6.91 + 2.48\lambda_{\Theta} - 12.27\lambda_{\Theta}^2 \text{ for } \lambda_{\Theta} > 0 \qquad (2.12)$$

for $-0.09 < \lambda_{\Theta} < 0.058$ and free stream turbulence levels between 0.3% and 5%. The prediction of the end of transition was found to be rather difficult due to the scattering of the results. In the empirical relations presented different regions must be distinguished. *Johnson* [1994] proposed another relation for transition onset based on experimental data for the pressure gradient parameter $\lambda_{\Theta}$ between -0.1 and 0.1 and turbulence levels between 0.2% and 5%.

## Effect of compressibility

The contribution of compressibility in connection with high free stream turbulence levels on transition still is not clear. Opinions with respect to the importance are not identical [*Narasimha*, 1985, *Mayle*, 1991]. The reason for this is that all compressible flow data are obtained at low turbulence levels. *Zysina-Molozhen and Kuznetsova* [1969] found that the experimental data available suggested an increasing transition Reynolds number equal to

$$\frac{Re_M}{Re_{(M=0)}} = 1 + 0.38M^{0.6} \qquad (2.13)$$

where $M$ is the Mach number. This trend was obtained from tests with rocket noses and cones in flight and wind tunnels. In these experiments the highest free stream turbulence level was 1.3% at Mach numbers around 0.2 and 2.0. The transition has been determined either with micro tubes in the boundary layers or by interpreting interferograms and shadowgrams. According to relation 2.13 the
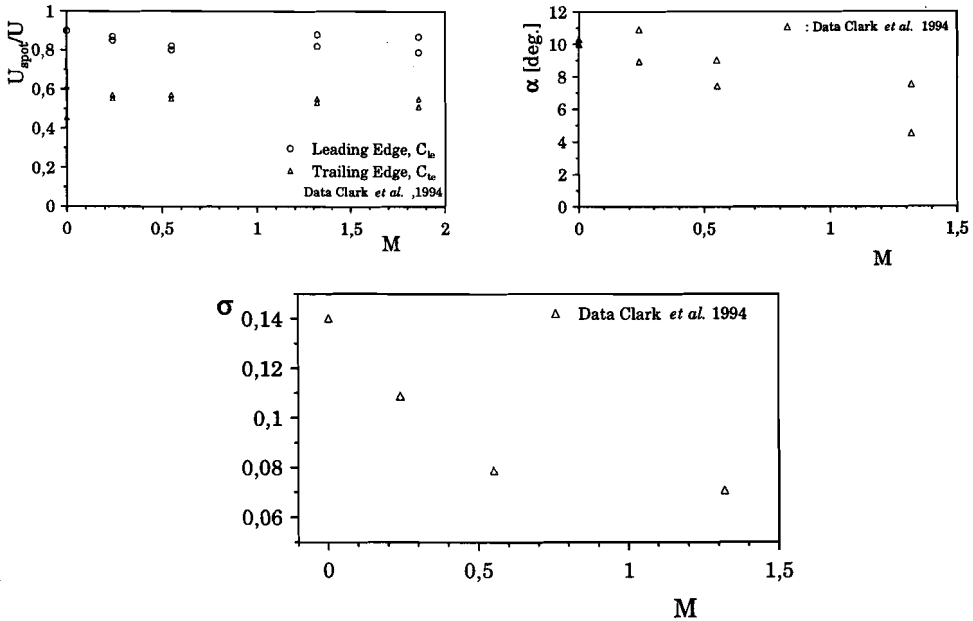


*Figure 2.13: The effect of Mach number on propagation velocity (upper left-hand figure), on growth angle (upper right-hand figure) and resulting spot propagation parameter, $\sigma$ (in lower figure), according to Clark et al. [1994].*

transition onset is delayed by 38% in Reynolds number for $M = 1$. The physical reason may be found in the fact that a compressible boundary layer is more stable due to a fuller velocity profile [*Schlichting*, 1979]. *Mayle* [1991] estimated an 8% to 30% increase in the length of transition for $M = 1$. This is supported by the experimental work of *Clark et al.* [1994] who performed heat transfer

measurements in an Isentropic Light Piston Tunnel (ILPT) for $0.24 \leq M \leq 1.86$ and $Tu = 0.1\%$. They also found a decreasing spot spreading angle $\alpha$, with increasing Mach numbers, whereas the stream-wise growth is almost unaffected. The spot propagation parameter $\sigma$, is shown in figure 2.13. However, quantitative measurements for spot production rate $\hat{n}\sigma$, are still not available for compressible flows with higher free stream turbulence levels.

## 2.6    Conclusions

Boundary layer transition in flows with high free stream turbulence levels is mainly dominated by free stream turbulence, pressure gradient and compressibility. Too few experimental data are available about the effect of turbulence structure and compressibility on boundary layer transition at higher free stream turbulence levels. The uncertainty introduced by this lack of information causes an expected inaccuracy in the onset of transition of $\pm$ 25% due to the turbulence scale effect. This is concluded from the experimental data available at present. The uncertainty may be even larger because the present data are based on three mesh dimensions only (figure 2.11). An additional uncertainty is caused by the effect of compressibility. First estimates show a delay in transition of 38% at $M = 1$, while the transition length is expected to increase by 8% to 30% at the same Mach number.

# Chapter 3

# Experimental Ludwieg tube set-up

## 3.1 Introduction

Previous chapters showed that experiments are lacking in the regime for Mach numbers between 0 and 1, and free stream turbulence levels between 1% and 10% with favourable pressure gradients. Experiments in this range have to satisfy several requirements:

- The Mach number, Reynolds number, free stream turbulence levels and pressure gradient must be independent parameters that can be adjusted in the desired range.

- The transition length of the boundary layer has to be large enough. In order to measure with sufficient spatial accuracy, the transition zone has to be 10 cm.

It will be shown that these requirements make the application of an atmospheric wind-tunnel inadequate. In the following the wind-tunnel, Isentropic Light Piston Tunnel and Ludwieg tube are compared.

**wind-tunnel**
With some effort higher subsonic Mach numbers can be created in an atmospheric wind-tunnel, just like high free stream turbulence levels and pressure gradients. But because density and temperature can not be adjusted, the unit-Reynolds number $Re_u = u/\nu \ [m^{-1}]$, is directly coupled to the Mach number. With the assumption that the kinematic viscosity $\nu$, is $1.6 \times 10^{-5} \ m^2/s$ and the velocity of sound $c$, is $340 \ m/s$, the relation for Mach number ($=u/c$) and unit-Reynolds number is given by

$$M = \frac{\nu}{c} Re_u = 4.7 \times 10^{-8} Re_u \tag{3.1}$$

This relation describes the trajectory of an atmospheric wind-tunnel and is represented in figure 3.1. Increasing the Mach number consequently implies increasing
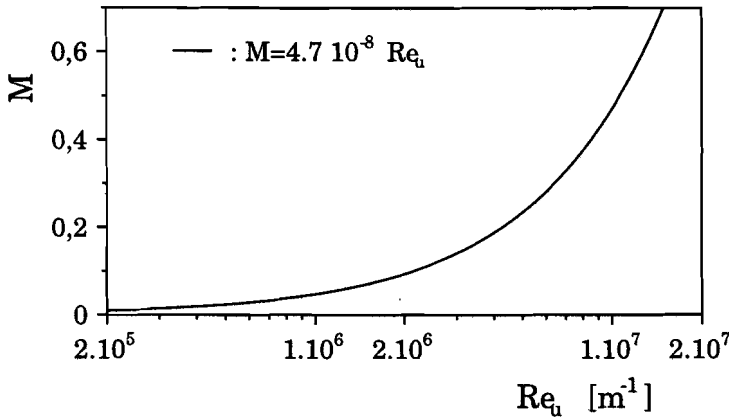


*Figure 3.1: Coupled trajectory for Mach and unit-Reynolds number for atmospheric wind-tunnel.*

the unit-Reynolds number. For a certain fixed Reynolds number $Re_{L_t}$ ($= L_t.Re_u$), based on the transition length $L_t$, the transition length linearly decreases with increasing unit-Reynolds number (and Mach number). Moreover, $Re_{L_t}$ is strongly dependent on the free stream turbulence level. According to equation 2.1 for intermittencies between 0 and 0.99, this length is given by

$$Re_{L_t} = \sqrt{\frac{\ln(0.01)}{-\hat{n}\sigma}} \qquad (3.2)$$

where $\hat{n}\sigma$ describes the empirical relation (from figure 2.10) between transition length and turbulence level of Mayle (equation 2.7). Relation 3.2 is plotted in figure 3.2 (left-hand), which shows a decreasing transition length for increasing free stream turbulence level. If the transition length $L_t$, is fixed to 0.1 $m$ the required unit-Reynolds number is plotted in the right-hand figure. The curve for $L_t$ equal to 0.1 $m$ determines the right-hand side limit for the acceptable unit-Reynolds number. Higher $Re_u$ will cause the transition length to be smaller than 0.1 $m$. This result can be combined with figure 3.1 leading to figure 3.3, where the different free stream turbulence levels (indicated with the dots in figure 3.2) are drawn as altitude levels in the $M - Re_u$ graph. Since no transition data are available at higher subsonic Mach numbers, the 'incompressible' results are applied for the Mach range. The individual turbulence intensity lines (dashed lines) correspond to a transition length $L_t$ of 0.1 $m$. To the left of each line the transition length will be longer. It can be seen that for a turbulence level of e.g. 2% the maximum unit-Reynolds number allowed is $3 \times 10^6$, which corresponds to a Mach number equal to 0.14. Thus, for higher Mach numbers the
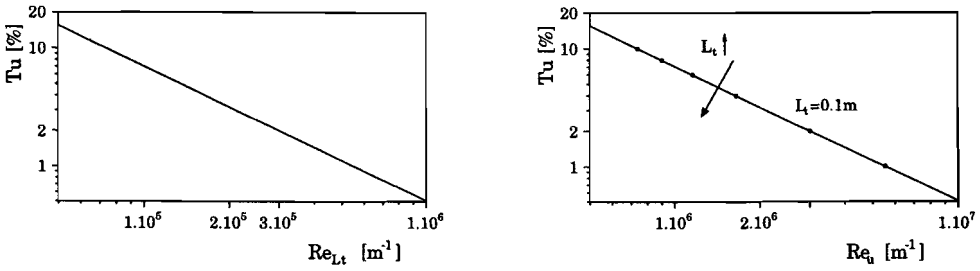
*Figure 3.2: Decreasing Reynolds transition length $Re_{L_t}$, with increasing free stream turbulence level (left-hand). The right-hand figure shows the same trend for the unit-Reynolds number required assuming a constant transition length $L_t$, equal to 0.1 m. The dots refer to the dashed lines in figure 3.3*
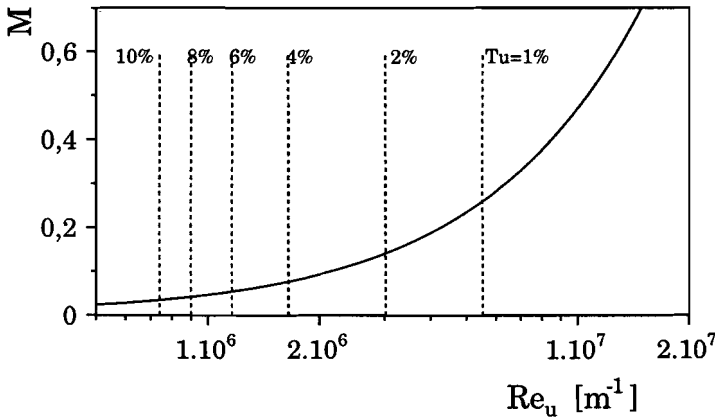


*Figure 3.3: The required unit-Reynolds number to have a transition length of 0.1 m (dashed lines). The trajectory of an atmospheric wind-tunnel is drawn with the solid line.*

transition region in an atmospheric wind-tunnel will be smaller than 0.1 $m$. For a free stream turbulence level of 1% the maximum Mach number will be equal to 0.25. For lower Mach numbers the transition length will be longer than 0.1 $m$. To investigate the influence of Mach number at turbulence levels above 1%, an experimental set-up is needed that can cover the range for the unit-Reynolds number between $5.10^5$ to $10^7$ and for the Mach number between 0 and 1.

### Isentropic Light Piston Tunnel

An experimental set-up that can vary the unit-Reynolds number, Mach number and gas-to-wall temperature ratio independently is the Isentropic Light Piston Tunnel (ILPT). The ILPT is a transient facility that pumps isentropically compressed air (compressed with piston construction) through a test section into

a dump tank. The test time depends on the set-up geometry and varies typically between 70 $ms$ [*Ching and LaGraff*, 1995] and 300 $ms$ [*Clark et al.*, 1994]. Depending on the test section configuration the flow can either be subsonic or supersonic. This facility is frequently used in boundary layer transition research, but up to now has only been applied to test sections with a number of turbine blades. A disadvantage of the performed experiments is that the pressure gradient is unknown.

Two experimental facilities have been applied to create a well defined pressure gradient, unit-Reynolds number, Mach number and free stream turbulence level. In these experiments the Mach number and unit-Reynolds number were coupled. *Clark et al.* [1994] performed experiments at a free stream turbulence level of 0.1%. They reported Mach numbers between 0.24 and 1.86 and related unit-Reynolds numbers between $7.5 \times 10^6 m^{-1}$ to $16 \times 10^6 m^{-1}$. The experiments of *Ching and LaGraff* [1995] ranged from unit-Reynolds numbers between $1.8 \times 10^6 m^{-1}$ to $4.2 \times 10^6 m^{-1}$, with Mach numbers equal to 0.05 and 0.1 with a turbulence level equal to 0.5%. No experiments have been performed at higher turbulence levels. It is not clear whether lower unit-Reynolds numbers are feasible. If the lower unit-Reynolds number is really limited by the value $1.8 \times 10^6 m^{-1}$, a free stream turbulence level of 4% will give a transition length of 0.1 $m$. Higher free stream levels lead to shorter lengths (according to equation 3.2). This experimental set-up has the advantage that gas-to-wall temperature ratio, unit-Reynolds and Mach numbers can be varied independently. It also has some disadvantages. There is a relatively large fluctuation in static pressure of $\pm$ 3.5% caused by shock and expansion waves (as shown in figure 3.21). This causes stronger variations in unit-Reynolds and Mach numbers. Furthermore, the set-up is complicated from a constructive point of view and is expensive.

**Ludwieg tube**

Another experimental facility in which Mach number and unit-Reynolds number can be varied independently over a wide range is the Ludwieg tube. This experimental set-up has often been used to generate super- and hypersonic flows [*Schneider and Haven*, 1995]. Remarkably, this set-up has not been applied yet in boundary layer transition research in the regime discussed earlier. Only one article was found in which a Ludwieg tube in subsonic configuration was used. It focuses on film cooling with fixed turbulence intensity at 0.6% and Mach number equal to 0.42 [*Zhang et al.*, 1993].

In cooperation with the Faculty of Applied Physics at Eindhoven University of Technology the applicability of the Ludwieg tube was studied. The performance analysis of the Ludwieg tube, discussed in this chapter, shows that the desired range (presented in figure 3.3) can be covered. This is shown in figure 3.4. Here, the relation 3.2 is once again used for the transition length prediction. The work presented in this thesis includes Mach numbers up to 0.62 at maximum. Moreover, higher Mach numbers are possible with some additional measures. An
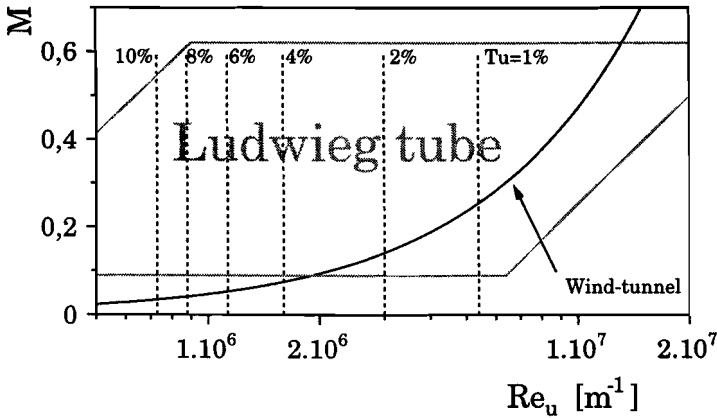
*Figure 3.4: The available range of Mach number and unit-Reynolds number for the present Ludwieg tube set-up (within gray lines) and the ranges necessary to have a sufficiently long transition length to perform accurate measurements at prescribed turbulence levels (dotted lines).*

option is discussed at the end of this chapter. In this chapter the principle of the Ludwieg tube in subsonic configuration is explained first. To study different aspects of the Ludwieg tube three design test sections were used. The construction and results of these test sections are discussed.

This knowledge is integrated in the design of a final test section. This design is discussed together with the resulting quality of the flow conditions, the available range for Mach number, unit-Reynolds number and free stream turbulence level. Furthermore, the gas dynamical relations and the way to determine the Mach and Reynolds number are described.

The chapter ends with some conclusions and an evaluation of the performance of the Ludwieg tube compared to other experimental set-ups.

## 3.2    Principle

The Ludwieg tube is a transient facility in which gas dynamical waves generate a well defined flow. The waves are introduced from an initial stepwise pressure distribution. The resulting conditions can be adapted by means of initial pressure levels and area reductions.

The Ludwieg tube as employed, consists of a 10 $m$ long tube. This tube is made of stainless steel (wall thickness 20 $mm$) and is fixed solidly at a height of 1.2 $m$. The cross-section of the tube measures $0.1 \times 0.1$ $m^2$ and is connected via the test section (TS) to the low pressure dump tank (DT) (figure 3.5). The diaphragm (D), between TS and DT, separates the low pressure DT from the higher pressure in the tube. The DT can be detached easily from the tube and is
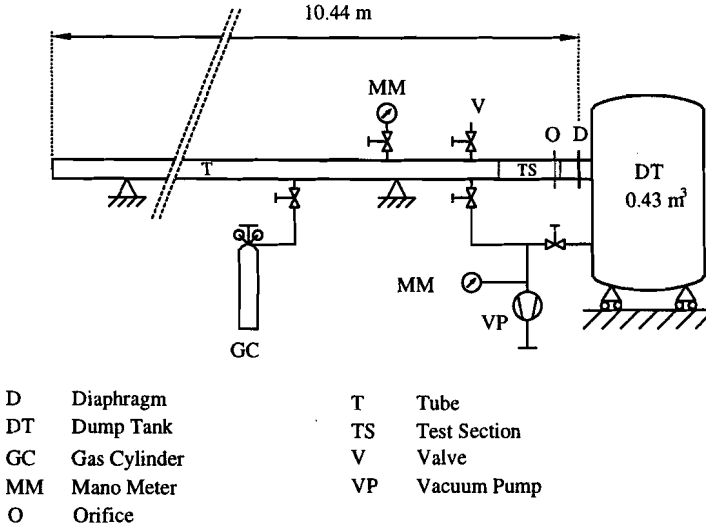
*Figure 3.5: Schematic diagram of the experimental Ludwieg tube set-up.*

movable in order to replace the diaphragm before each experiment. A diaphragm of 50 $\mu m$ thick Melinex is used, which can resist pressure differences of $2 \times 10^5$ $Pa$. Opening is obtained by means of an electrically heated cross-wire.

Before every experiment the DT is evacuated to about 500 $Pa$. The tube (T) can be filled with an arbitrary gas. To obtain a pure composition in this situation, the tube can first be evacuated to about 100 $Pa$ by means of the vacuum pump (VP). The desired pressure in the tube can be adjusted using gas cylinder (GC) (for gases different from air or pressures above ambient pressure), valve (V) and the vacuum pump.

Figure 3.6 shows the space-time representation of the wave patterns in the x,t-diagram. After the diaphragm is ruptured a shock wave and contact surface run into the DT. An expansion wave runs into the tube, which causes a supercritical pressure ratio over the smallest cross-sectional area, the orifice (O). The flow becomes choked locally. The expansion wave accelerates the fluid until the sonic velocity is reached at the orifice opening area. From the moment this sonic condition is reached the downstream information (among other things the rest of the expansion wave) can not travel upstream anymore. This part of the expansion wave is swept back in the direction of the DT causing a supersonic flow downstream of the orifice. The expansion wave runs through the test section and the Ludwieg tube T, accelerating the flow to a Mach number $M_t$. The value of this Mach number is determined by the ratio of the tube area and the area of the orifice. The expansion wave reflects at the far tube-end and returns. The time between the first and second passage of the expansion wave at the TS is the test
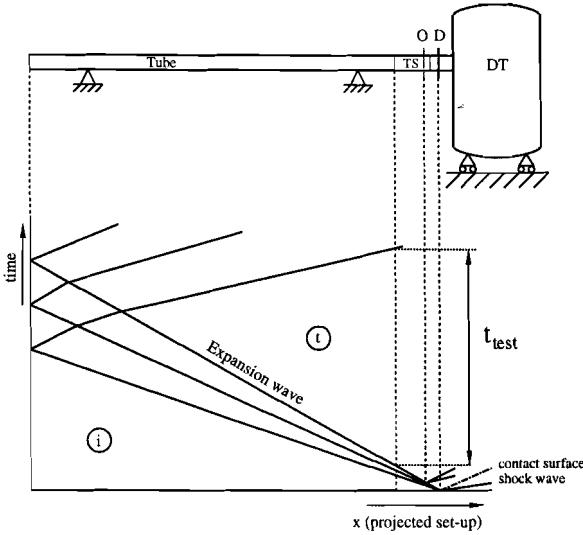
*Figure 3.6: Space-time representation of wave patterns in an x,t-diagram for a Ludwieg tube set-up. (i=initial condition region, t= test condition region)*

time $t_{test}$ ($\approx 55$ $ms$). As long as the pressure ratio over the orifice is supercritical, the flow downstream of the orifice is supersonic and no disturbances return from the DT. During the test time a steady flow of low temperature gas is present at the TS (region t in figure 3.6).

## 3.3 Development of the test section

Three different preliminary test sections have been used with different purposes. In this paragraph the aim, design and result of each test section design is discussed.

### 3.3.1 Test section 1: Flow conditions and constancy

The first type of test section simply consists of an orifice. The primary aim of this test section was to investigate the available test time, the constancy of the pressure signal, the agreement with predictions of gasdynamical relations and the reproduction accuracy.

Two orifice geometries were tested (figure 3.7): a 1 $mm$ thick aluminium plate with square aperture (TS1a) and a contraction created by two blocks with a rounded entrance (TS1b). The pressure is recorded upstream and downstream of the contraction (figure 3.8). The different orifice geometries were used to study

test section TS1a

front view

Flow

1 mm

55.5 mm

54.5
mm

test section TS1b

front view

Flow

r=39.5 mm

37.0 mm

150 mm
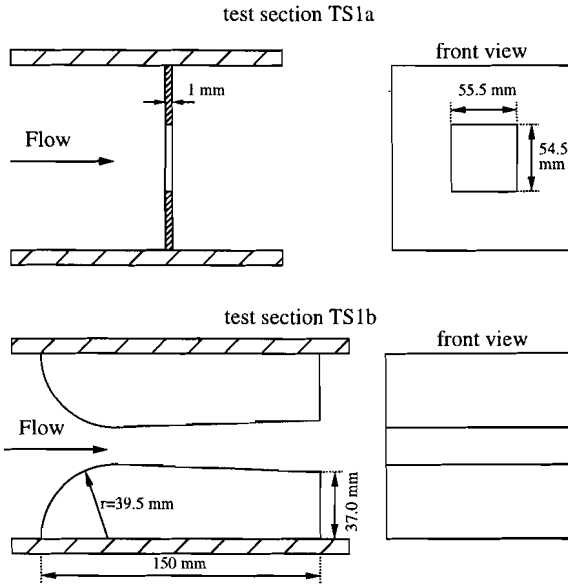
*Figure 3.7: Orifice test sections TS1a and TS1b.*

10 m

Test Section

PG₁

T

PG₂

D

DT

515
mm

540 mm

2235 mm

D    Diaphragm
DT   Dump Tank
PG   Pressure Gauge
T     Tube
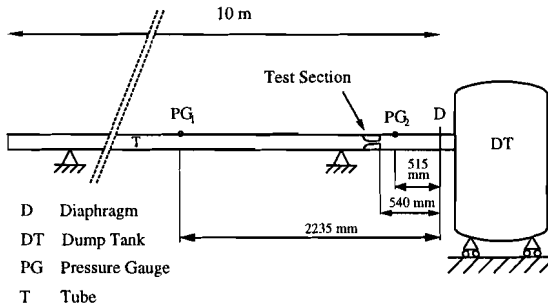
*Figure 3.8: Position of sections TS1a, TS1b and TS2 in the Ludwieg tube.*

the influence of the shape of the contraction on the resulting conditions. The sufficiently strong expansion wave causes choking at the orifice. Consequently, the area ratio $A_{tube}/A_{or}$, determines which part of the expansion wave will pass, causing an upstream Mach number that is related to this orifice area. *Owczarek* [1964] shows with conservation of mass and momentum for a 1-D inviscid homenergetic flow that the area ratio and upstream Mach number are related by

$$\frac{A_{tube}}{A_{or}} = \frac{1}{M_t} \left[ \frac{2}{\gamma + 1} \left( 1 + \frac{\gamma - 1}{2} M_t^2 \right) \right]^{\frac{\gamma+1}{2(\gamma-1)}} \tag{3.3}$$

where $\gamma$ is the ratio of the specific heats and the indices *or* and *t* refer to the orifice and test condition, respectively. It is precisely that part of the expansion wave that accelerates the upstream flow to the sonic condition in the orifice, which is transmitted. Relation 3.3 is very convenient to design orifices that lead to a prescribed Mach number flow.

A more accurate determination of the Mach number $M_t$, is obtained from the measured pressure ratio $p_t/p_i$. With the Euler equations, the definition of the velocity of sound, the assumption of an isentropic flow and the ideal gas law, it can be shown that along the so-called characteristic $C_+$-lines ($dx/dt = u \pm c$) the quantities $u \pm \frac{2c}{\gamma-1}$ are constant [*Owczarek*, 1964]. Using the relation for the $C_+$-characteristic across the expansion wave and the isentropic relation:

$$\frac{p_t}{p_i} = \left( \frac{c_t}{c_i} \right)^{\frac{2\gamma}{\gamma-1}} \tag{3.4}$$

it follows that

$$M_t = \frac{2}{\gamma - 1} \left[ \left( \frac{p_t}{p_i} \right)^{-\frac{\gamma-1}{2\gamma}} - 1 \right] \tag{3.5}$$

which gives the Mach number $M_t$, from the recorded pressure. The other flow conditions like velocity $u_t$, static gas temperature $T_t$ and density $\rho_t$ are derived using the relations for Mach number: $M = u/c$, velocity of sound: $c^2 = \gamma RT$ and ideal gas law: $p = \rho RT$ with $R$ the gas constant. Sutherland's law has been applied to compute the dynamic viscosity $\mu$

$$\mu = 1.458 \times 10^{-6} \frac{T^{1.5}}{T + 110.4} \tag{3.6}$$

With the viscosity the Reynolds number can be calculated. An experiment with TS1b to check the correspondence between the predicted and the measured pressure is shown in figure 3.9. During the test time a very constant pressure is obtained, with variations less than 0.5%. The dashed line shows the predicted pressure ratio $p_t/p_i$, using equations 3.3 (to predict the Mach number) and 3.5 (to convert the predicted Mach number to the pressure ratio). The solid line represents the measured pressure. With equation 3.3 a small underestimation is
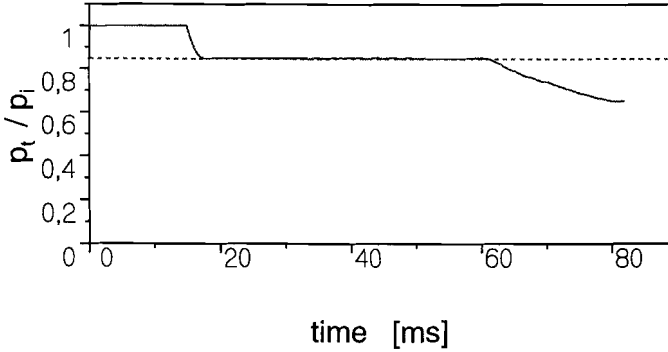
*Figure 3.9: Pressure ratio $p_t/p_i$, predicted according to equation 3.3 (dashed line) compared with a Ludwieg tube experiment (solid line). The pressure is read with pressure gauge $PG_1$, which results in a shorter test time than available at the test section. (Test section TS1b, $Re_u = 2.4 \times 10^6$ $[m^{-1}]$, $M_t$=0.12).*

found, but the difference in pressure is less than 1%. Therefore, the Mach number obtained (with equation 3.5) deviates somewhat from the predicted Mach number (see also table 3.1). This is caused by streamline curvature effects in the orifice flow, resulting in a smaller effective orifice area.

A very important feature is that the obtained Mach number is almost independent of the initial pressure. This implies that adjustment of the absolute initial pressure in the tube $p_i$, leads to a change in the unit-Reynolds number independent of the Mach number; the orifice determines the Mach number, the initial pressure in the tube the Reynolds number. This property is used in the rest of this work to realize the desired unit-Reynolds and Mach number. This quality of the Ludwieg tube makes it distinct from the atmospheric wind-tunnel experiments.

Due to the expansion wave, the gas temperature $T_t$, decreases causing a temperature difference between wall and gas flow. The size of the temperature drop is related to the Mach number (actually related to the depth of expansion) by

$$\frac{\Delta T}{T_i} = \frac{T_i - T_{t,r}}{T_i} = 1 - \frac{T_t}{T_i}\left(1 + r\frac{\gamma - 1}{2}M_t^2\right) \tag{3.7}$$

where $T_i$ is the initial gas temperature, $T_{t,r}$ is the recovery temperature in region t and $r$ is the recovery factor [*Schlichting*, 1979]. The surface temperature of an object at high speed is higher than the temperature of the undisturbed air. For an adiabatic wall condition the surface reaches a temperature $T_r$, equal to the temperature of the air adjacent to the surface, due to friction. This temperature is somewhat less than the local adiabatic stagnation temperature and is known as the recovery temperature. The recovery factor is equal to $\sqrt{Pr}$ and $\sqrt[3]{Pr}$ for a laminar and turbulent boundary layer, respectively [*Lin*, 1959], with $Pr$ the

Prandtl number.

The heat transfer rate is linearly related to this temperature difference. For an initial gas temperature $T_i$, of 300 $K$ the maximum experimental temperature difference (for $M_t = 1$) is about 50 $K$. For a Mach number of 0.18 this difference drops to the low value of about 18 $K$.

At this point it is worth noting that with the pressure all flow properties can be determined. From the experiments with the first test section it turns out that the orifice geometry has hardly any influence. The pressure ratio obtained with the 'square-hole orifice' TS1a, deviates less than 1% from the theoretically obtained value. The same holds for the pressure obtained with the rounded blocks (figure 3.9). This result is applied in the final design and construction of the test section (see section 3.4), using orifices consisting of simple plates with a number of rectangular holes. It turns out that these orifices had a somewhat higher deviation in pressure (about 1.9%) for the same area ratio as the first test section. A possible reason for this slight increase may be that the latter orifice contains three holes compared to only one in the first orifice. The effect of non-one-dimensional behaviour may be more emphatic. However, the only consequence is that the resulting Mach number according to equation 3.5 will be somewhat different (lower) from the design Mach number.

### 3.3.2 Test section 2: Flow development around a complex geometry

A second test section was designed (TS2) with the purpose to visualize the transient flow development around a 'complex' geometry. Since the Ludwieg tube is a transient flow generating set-up, the flow around the object in the test section must be fully developed within the test time. The available test time is reduced due to the time required to obtain a steady, developed flow at the body of observation (e.g. flat plate, turbine blades). To obtain an impression of the time required for instationary flow development, a flow visualization was performed with test section TS2. A 2-D cascade was constructed where the aspect of optical visibility was taken into account. The construction is composed of two blades that are kept in position by fixation bars mounted on blocks (figure 3.10). The blocks are fixed to the tube wall and have the function of guiding the up- and downstream flow. The orifice is formed by the smallest cross-section. Due to the local choking and supersonic flow downstream of the geometry, different phenomena like shock waves and slip lines are clearly visible. These phenomena are utilized to indicate the development of the flow. The test section is situated at the same position as the previous test section (figure 3.8). Figure 3.11 shows a shadowgraph visualization of the flow in test section TS2 at different stages after the expansion wave has passed. The first picture clearly shows a shear layer at the trailing edges that ends up in a vortex. Wakes, shock waves and slip lines are generated in the supersonic flow behind the blades in the milliseconds that follow.
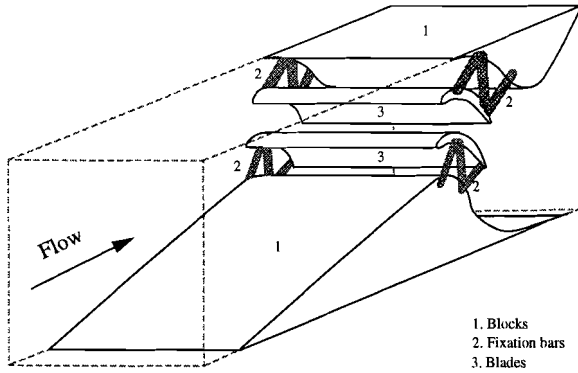
*Figure 3.10: Perspective sketch of test section TS2 designed for flow visualization. Two cascade blades are mounted on blocks. The optical accessibility is taken into account.*

The flow develops in about 10 $ms$ and is constant during the rest of the test time. This experiment shows that at one specific Reynolds value ($Re_u = 5.2 \times 10^6 \; m^{-1}$, $M$=0.3 in front of the blades) sufficient time is left (about 40 $ms$) to perform measurements in a steady, developed flow.

### 3.3.3   Test section 3: Heat flux measurements

Test section 3 was constructed to perform heat flux measurements. The aim of the experiments with this test section was to study the adequacy of the Ludwieg tube for heat transfer measurements in a transitional boundary layer. Test section TS3 (figure 3.12) consists of a 10 mm thick flat brass plate (l×w×h: 190×85×10 $mm^3$) with a sharp leading edge (20°). To introduce an angle of attack, the plate is mounted on a fixation block with a hinge point. To mount the construction and to carry away the electrical wires from the thin film gauges, two holes are available in the tube. A glass plate (l×w×h:190×85×3 $mm^3$) with the heat flux gauges (thin film gauges) at the surface is pasted on the brass plate. The glass substrate has a sharp leading edge of 30°. To connect the electrical circuit at the upper side with the lower side, plastic strips (width=7.5 $mm$) are mounted on both sides of the table with brass pins (see right-hand figure 3.12). At the top the thin film gauges are connected to these pins with a thin brass wire (d=0.15mm). Silver paint connects this wire with the thin film gauges. The electrical wires underneath of the flat plate are guided to the bottom wall of the tube by two parallel plates in the wake of the fixation block. A plastic plug carries the wires outside.

The orifice is composed of two parts. The upper orifice (figure 3.12) consists

a)                                                    b)





c)                                                    d)
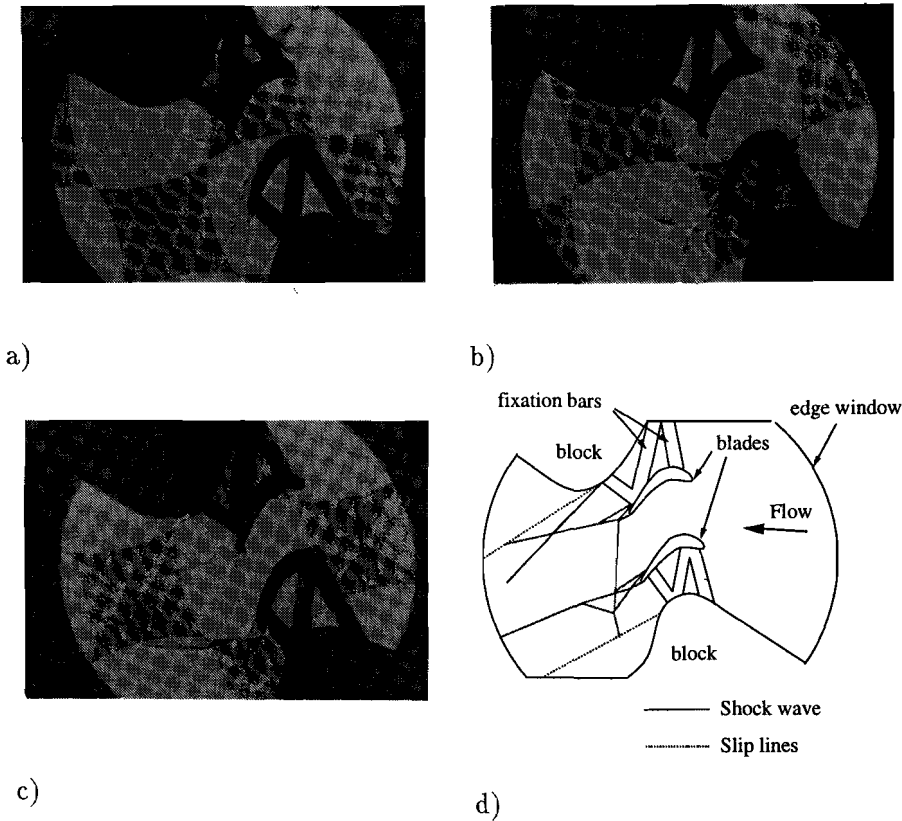
*Figure 3.11: Shadowgraph pictures showing the development of a flow around a 2-D cascade. (a: t=2.0 ms, b: t=10.0 ms, c: t=50.0 ms and d: the explanation of the different flow phenomena in steady flow situation, $Re_u = 5.2 \times 10^6\ m^{-1}$, M =0.3 in front of the blades).*

of an area reduction due to the presence of 9 parallel rods (d=9 *mm*). The contraction at the lower side is fully due to three stabilizor rods. The wake behind the fixation block also reduces the effective orifice area. The upper area reduction is chosen somewhat larger than the reduction at the lower side. In this way the streamlines are bent downwards slightly in front of the flat plate, which reduces the risk of boundary layer separation at the plate leading edge. This causes a somewhat different Mach number for upper and lower side. Because some results are obtained with this test section, for example the propagation of turbulent spots, the flow conditions have to be determined as accurately as possible. (The determination of the flow condition in this case is treated in appendix B). The Mach number that corresponds to the effective orifice area is equal to 0.33. The three lower rods have the additional function of keeping the plate at the desired

1. Glass substrate with sensors          6. Electrical wires
2. Brass 'table'                          7. Plug to carry wires outside
3. Hinge point                           8. Tube wall
4. Fixation block                         9. Lower orifice/table stabilizor
5. Protection plates for electrical wires 10. Upper orifice (9 rods)
   (in wake of fixation block)           11. Pressure gauge

1. Glass substrate    5. Electrical wires
2. Brass table        6. Lower orifice/table stabilizor (3 rods)
3. Plastic strips     7. Upper orifice (9 rods)
4. Brass pin          8. Tube wall

*Figure 3.12: Sketch of the test section TS3 which is suitable for heat flux measurements. Side view (left-hand) and front view (right-hand).*

angle during the experiment. To keep the relative area reduction on the lower side as small as possible, the position of the table is chosen to be rather high.

Figure 3.13 shows the instantaneous heat flux at three locations from the leading edge ($x = 0.013\ m$, $0.063\ m$, and $0.183\ m$, $M = 0.33$, $Re_u = 1.1 \times 10^7$ $m^{-1}$). The arrival of the incident expansion wave induces a flow. The upper graph shows that this causes a very thin boundary layer at first, resulting in a high heat flux level. Due to unsteady boundary layer growth the heat flux level decreases. After about 3 $ms$ a steady heat flux is obtained, indicating a steady boundary layer thickness. All three measurements clearly show that the flow development at a flat plate takes less time compared to a more complex geometry. This is presumably caused by the simpler geometrical configuration. In the previous test section recirculation zones had to be established that influence the observed flow pattern.

More in detail, the upper figure shows a constant heat flux level of a laminar boundary layer. What is interesting, is the sudden transition to a higher heat flux level (turbulent boundary layer) in the lower figure. A boundary layer at that position is in principle unstable for the steady flow conditions. However, the initially transient boundary layer is thinner and thus more stable. This situation changes when the critical thickness is reached. The figure in the middle shows the heat flux in the transition region of the boundary layer. The alternating low-high level clearly indicates the passing turbulent spots. Finally, it should be noted that the noise, present on the heat flux signal, is rather high. This noise level should be reduced to improve the accuracy of heat flux measurements.
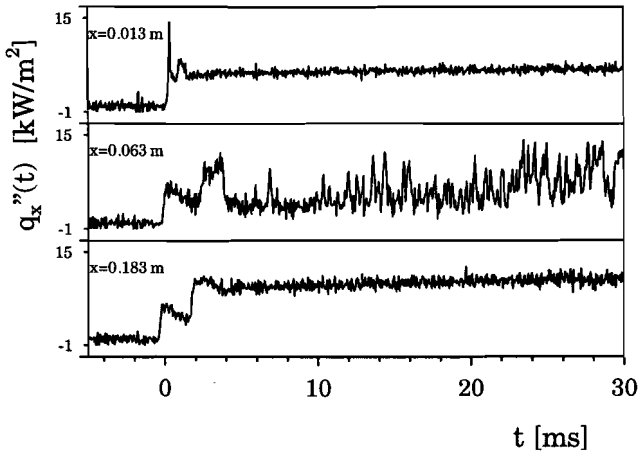
*Figure 3.13: Heat flux development at three locations at a flat plate ($x = 13$ mm, $x = 63$ mm and $x = 183$ mm) from the leading edge. (Test section TS3, $M = 0.33$, $Re_u = 1.1 \times 10^7$).*

### 3.3.4   Conclusions

The experiments with three different test sections have shown that boundary layer transition research with a Ludwieg tube is possible.

Experiments with the first test section ($M=0.12$) showed that the measured pressure differs less than 1% from the predicted pressure. The accuracy with which the conditions are determined can be improved using equation 3.5. The pressure obtained, is very constant. The variation is less than 0.5%. Besides, it was shown that the orifice shape has a negligible influence on the resulting flow conditions. The test time is found to be about 50 $ms$ for a flat plate configuration, whereas it is about 40 $ms$ for a more complex geometry (test section 2). The latter geometry requires more time to become fully developed than a flat plate (ca. 3 $ms$). Heat flux measurements on a flat plate clearly show the heat flux of a transient developing boundary layer. After the boundary layer has developed, the passing of turbulent spots in the transitional boundary layer shows up.

## 3.4   Construction of final test section

The final or fourth test section was designed using the results obtained with the first three test sections. A new tube section was integrated into the Ludwieg tube (left-hand figure 3.14). The inner cross-section is equal to the original tube area ($100 \times 100$ $mm^2$). The total length between the flanges is 500 $mm$. The position of the final test section in the Ludwieg tube is shown in figure 3.15. The whole test section construction was designed (and checked) to be airtight.

1. Stainless steel plate
2. Glass substrate
3. Plate angle adjustment
4. Connector to carry electrical wires outside
5. Pressure gauges
6. Exchangable orifice
7. Exchangable turbulence grids
8. Hotwire probe
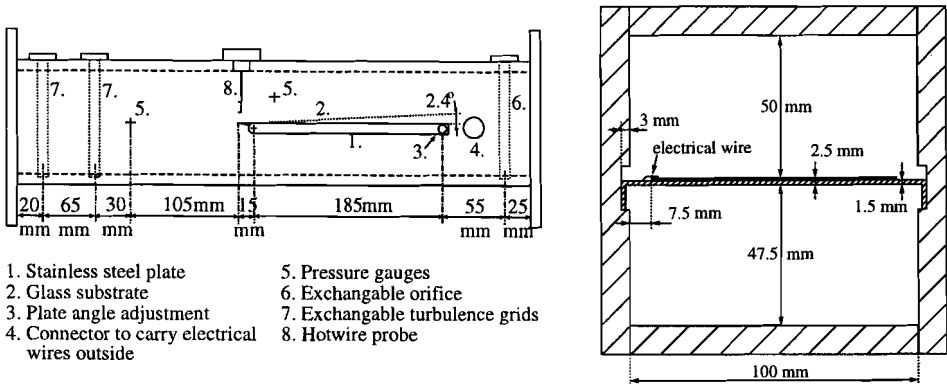
*Figure 3.14: Sketch of test section TS4 containing an adjustable flat plate with thin film heat flux gauges, exchangeable orifices, exchangeable turbulence grids and a hot-wire probe above the leading edge of plate. Side view (left-hand) and cross-section of test section at the flat plate (right-hand).*



D    Diaphragm
DT   Dump Tank
O    Orifice
T    Tube
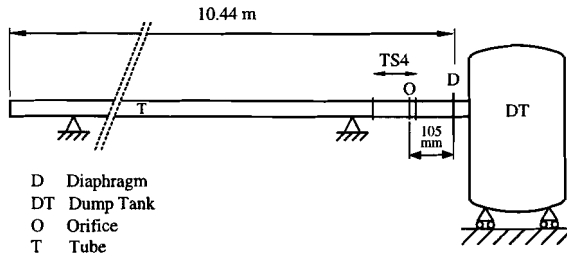
*Figure 3.15: Position of test section TS4 in the Ludwieg tube.*

A glass substrate ($l \times w \times h$:190×85×1 $mm^3$) carrying the thin film gauges, is pasted on a stainless steel plate ($l \times w \times h$:190×106×1.5 $mm^3$). Both the stainless steel plate and glass substrate are sharp at the leading edge. The lateral sides of the steel plate are folded $90^o$ to mount the plate in a 3 $mm$ deep slot milled in the tube wall (right-hand figure 3.14). The plate angle can be adjusted between $0^o$ and $2.4^o$. With this construction a minimal area reduction of 2.5% is obtained, such that the flow conditions in this section are hardly influenced by the presence of the plate. The width of the glass plate is smaller than that of the stainless steel plate. In this way some space (7.5 $mm$) is saved, to carry the electrical wires backwards from the film gauges lateral to the glass plate (right-hand figure 3.14). At the far end of the plate these wires are led outside the tube walls through a plastic connector.

Above and below the plate the top and bottom walls of the tube have been kept free of any objects. For the future this gives us the opportunity to apply profiles and select different pressure gradients and higher Mach numbers.

| | slot width $w_s$ [mm] | $A_{or}/A_{tube}$ | $M_{t,theory}$ (eq.3.3) | $M_{t,measured}$ (eq.3.5) |
|---|---|---|---|---|
| orifice 1 | 5.5 | 0.164 | 0.10 | 0.09 |
| orifice 2 | 11.3 | 0.338 | 0.20 | 0.18 |
| orifice 3 | 20.9 | 0.625 | 0.40 | 0.36 |
| orifice 4 | 27.8 | 0.832 | 0.59 | 0.5 |

*Table 3.1: Characteristic dimensions and parameters of the orifice plates used in test section TS4 ($A_{or}/A_{tube}$ is the ratio of orifice and tube area).*

## Pressure gauges

Two pressure gauges are mounted in the side tube wall, flush with the inner wall. One gauge 24 $mm$ above the glass sensor plate, 35 $mm$ from the leading edge, the other 105 $mm$ in front of the leading edge. These two positions have been chosen to determine the conditions at different stream-wise locations for the situation when local contractions are used. In the present experiments no differences were found.

## Choking orifice

The orifice is located at the far end of the test section. Four different orifices with different area ratios were used based on simple plates with slots. These plates were used because experiments with test sections TS1a and TS1b proved that the orifice shape does not play a significant role. The area ratios are chosen according to equation 3.3 to give resulting Mach numbers of 0.09, 0.18, 0.36 and 0.5. Higher subsonic Mach numbers are difficult to realize with the orifice only, because at higher subsonic Mach values, the Mach number becomes very sensitive to the area ratio $A_{tube}/A_{or}$. A method to increase the Mach number in the test section will be discussed at the end of this chapter. Each orifice has three slots with a height of 100 $mm$. The slot width $w_s$, for the different orifices are printed in table 3.1 together with the area ratios, and the theoretical and obtained Mach numbers. The slots are oriented vertically to reduce the effect of plate wake. The thickness of the brass orifice plates is 6 $mm$.

## Turbulence grids

Free stream turbulence is created artificially with a plane grid of cylindrical rods in a square mesh pattern [*Frenkiel and Ithaca*, 1948]. Turbulence intensity and its decay can be manipulated with the rod diameter $b$, and with the mesh size $m$, being defined as the centreline distance between parallel rods (figure 3.16). *Baines and Peterson* [1951] fitted the theoretical relation for the degree of turbulence, the rod size and downstream distance to the rods proposed by *Frenkiel*
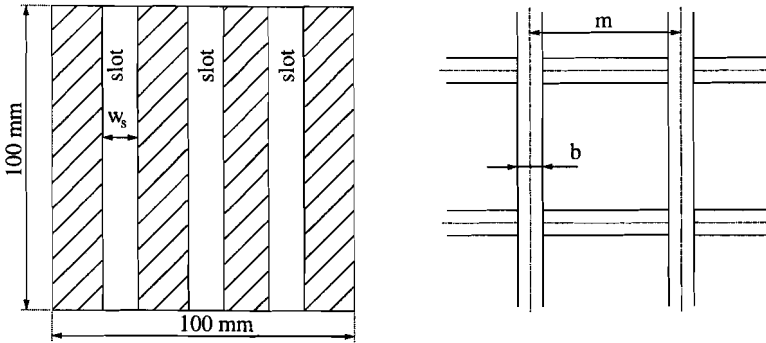
*Figure 3.16: Front view of the orifice geometry (left-hand) (the shaded area is blocked) and plane square turbulence grid with characteristic dimensions (right-hand).*

*and Ithaca* [1948] on several atmospheric wind-tunnel data sets with free stream turbulence levels ranging from 0.7% to 30%. They came to a practical relation that predicts the free stream turbulence level at distance $x$ downstream of the grid:

$$Tu(x) = 1.12 \left(\frac{x}{b}\right)^{-5/7} \qquad (3.8)$$

where $Tu$ is the free stream turbulence level in percents, $x$ is the downstream coordinate starting from the grid and $b$ is the rod diameter. In this relation no influence of the mesh size $m$, is observed. The free stream turbulence intensity at certain locations can be adjusted by means of the dimensionless parameter $x/b$.

Another important parameter for artificial turbulence generation is the grid solidity $\sigma$, which is the ratio of the grid area (blocked space) and tube area. The solidities in the experiments used to obtain equation 3.8, were varied from 0.2 to 0.9, with rod diameters between 8.5 $mm$ and 76 $mm$. The velocities ranged from 0.3 $m/s$ to 7.6 $m/s$. Due to anomalous behaviour of the flow for higher grid solidities, *Tan-Atichat et al.* [1982] advised to avoid solidities above 0.4.

For completeness it should be noted that the Reynolds number based on the rod diameter should exceed the value of 50 to get unsteady vortex shedding. In our case this value is always higher than 200.

For the Ludwieg tube an additional restriction to the turbulence grid holds, i.e. that its solidity should be smaller than the 'solidity' of the orifice. The latter should always have the smallest cross-sectional area. The solidity of orifice number 4 (Table 3.1) is equal to 0.17 ($1$-$A_{or}/A_{tube}$) which is very low for the construction of a turbulence grid. Grids that generate high turbulence intensities, which require larger rod diameters, unavoidably exceed this value. For solidities exceeding 0.37 no difficulties are found anymore in the construction of turbulence

| | rod diam. $b$ [mm] | mesh size $m$ [mm] | number of rods | solidity $\sigma$ | $M_{t,choking}$ (eq.3.3) | Tu [%] 140mm | (eq.3.8) 200mm |
|---|---|---|---|---|---|---|---|
| grid1 | 0.4 | 6.3 | 2×15 | 0.12 | 0.65 | 1.7 | 1.3 |
| grid2 | 1.0 | 12.5 | 2× 7 | 0.14 | 0.63 | 3.3 | 2.5 |
| grid3 | 2.0 | 10.0 | 2× 9 | 0.33 | 0.44 | 5.4 | 4.2 |
| grid4 | 4.0 | 21.0 | 2× 4 | 0.29 | 0.46 | 8.8 | 6.8 |
| grid5 | 6.0 | 25.5 | 2× 3 | 0.33 | 0.44 | 11.8 | 9.2 |

*Table 3.2: Dimensions and characteristic parameters of the turbulence grids applied ($M_{t,choking}$ is the upstream Mach number that leads to choking at the grid according to equation 3.3, Tu is the expected free stream turbulence level according to equation 3.8).*

grids. The test section was designed to generate turbulence levels varying from 1% to about 12%. This is done using five different grids that can be placed at two upstream positions (figure 3.14). Considering the height of the tube (100 $mm$) and solidity limit, 6 $mm$ is an optimum rod diameter. Larger rod diameters will cause too limited a number of rods in the flow, causing a non-uniform flow. According to equation 3.8 the closest upstream position for a turbulence level of 12% with 6 $mm$ rods is 140 $mm$. With the same grid at an upstream distance of 200 $mm$ the turbulence intensity is 9.2%. With grid rod diameters of 4 $mm$, 2 $mm$, 1 $mm$ and 0.4 $mm$ turbulence levels are step by step decreased to about 1%. Table 3.2 shows the different parameters for the grids applied. Grid numbers 3, 4 and 5 can not be applied for a Mach number of 0.5.

Grant and Nisbet [1957] studied the turbulence homogeneity in the lateral cross-section downstream of the turbulence grid. They showed in their experiments that the time averaged intensity varies smoothly between about 95% and 115% over space. The inhomogeneous pattern obtained did not show any correlation with grid mesh size and was shown to persist over at least 80 mesh lengths. All grid-generated turbulence showed this effect. They found that increasing the mesh size $m$, improves homogeneity.

Another important parameter is the anisotropy of the turbulence generated. In anisotropic turbulence, the intensity of the fluctuating velocity component perpendicular to the free stream flow $v'$, is different from the intensity in the stream-wise direction $u'$. Different experiments [*Comte-Bellot and Corrsin*, 1966] showed an anisotropy, $\sqrt{u'^2/v'^2}$, varying between 1.07 to 1.35, which slowly decreases with increasing downstream distance. The anisotropy of the flow in the Ludwieg tube was not measured.

**Hot-wire probe**

Above the plate tip a hot-wire probe can be mounted. A 21 $mm$ long hollow ceramic tube (d=2 $mm$) was pasted in a plastic flange and mounted in the test section wall (figure 3.17). Inside the ceramic tube two sets of prongs (d=0.3 $mm$) are mounted that are bended horizontally at distances of 30 $mm$ and 40 $mm$ below the upper wall. The prongs are sharp at the wire ends. To study
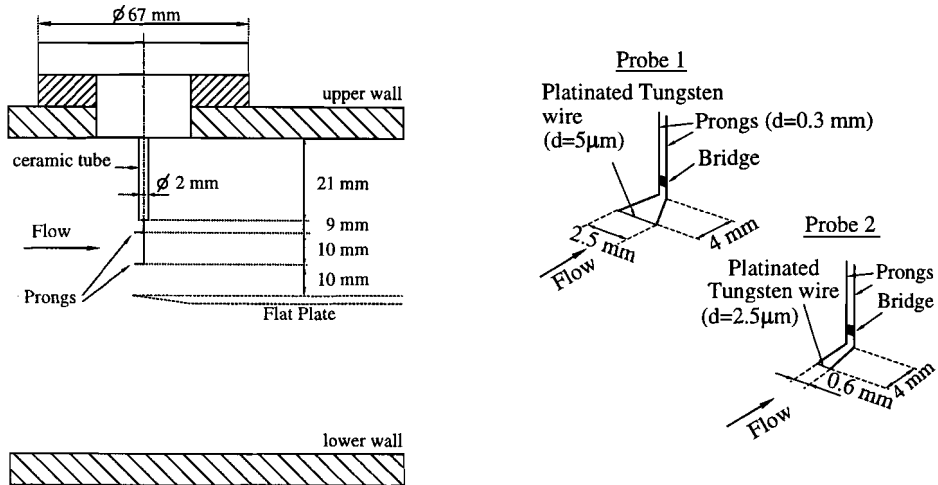


*Figure 3.17: Hot-wire probe dimensions and position in the Ludwieg tube (left-hand). Specific dimensions of probes on the spot of the hot-wire (right-hand).*

possible differences in height, two wires above each other have been used. The lower set of prongs is situated 10 $mm$ above the leading edge of the flat plate and is strengthened with a bridge that consists of a droplet of glue. Without this bridge a very severely disturbed signal is obtained. This is probably caused by the oscillation of the prongs causing dominant strain gauging. Even with this bridge a small peak in the frequency spectrum was obtained. This was reduced significantly when the wires were mounted with a little slack [Bruun, 1995]. To measure the free stream flow with fluctuations, the wires are placed horizontally and perpendicularly to the free stream flow.

# 3.5   Performance and properties of the final test facility

In this section the quality of the final test section is studied. Several aspects were investigated, like test time, variation of flow conditions, reproduction accuracy, etc.

### 3.5.1  Test time

The available test time is determined by the time between the arrival of incident and reflected expansion wave and is given by (according to *Owczarek* [1964]):

$$\frac{c_i t_{test}}{L} = \frac{2}{1 + M_t}\left[1 + \frac{\gamma - 1}{2}M_t\right]^{\frac{\gamma+1}{2(\gamma-1)}} \tag{3.9}$$

where $c_i$ is the velocity of sound at initial condition and $L$ is the length between the test section (pressure gauge) and the far tube-end. As a matter of fact, the length $L$ in equation 3.9, is the distance between the diaphragm (the start of expansion wave) and the far tube-end. Due to the small expansion wave length at the test section, the error made is small.

   Figure 3.18 shows a comparison of equation 3.9 with experiments. Very
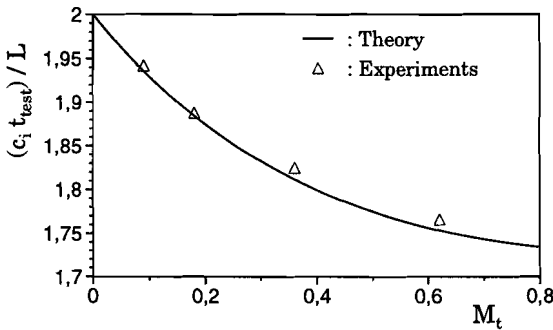


*Figure 3.18: The experimental and theoretical dimensionless test time as a function of $M_t$ (Test section TS4, $\gamma = 1.4$).*

good agreement is obtained with differences less than 0.7%. The uncertainty of the determination of the test time is about 0.4%. An increased upstream Mach number results in a slightly decreased test time from 56 $ms$ for $M_t = 0.09$ to 51 $ms$ at $M_t = 0.62$. This reduction in test time is caused by the fact that the reflected expansion wave moves faster due to a higher gas velocity. The 'effective' test time is about 3 $ms$ shorter due to flow development (which became clear from experiments with test section TS3).

### 3.5.2  Variation of flow conditions

One of the important parameters with respect to accuracy, is the variation of the flow conditions during the experiment. Two different variations of conditions can be distinguished:

- Variations at smaller time scales due to turbulent fluctuations.

- Variations at larger time scales ($> 5$ $ms$) due to e.g. wave reflections or boundary layer growth at the tube wall.

Figure 3.19 shows the relative pressure variation in the test section (TS1b) measured at the tube wall. Due to the generation of vortices in the turbulent boundary layer at the tube (commonly a turbulence level of 20%, while the maximum fluctuations are even larger), pressure fluctuations are brought about. A crude
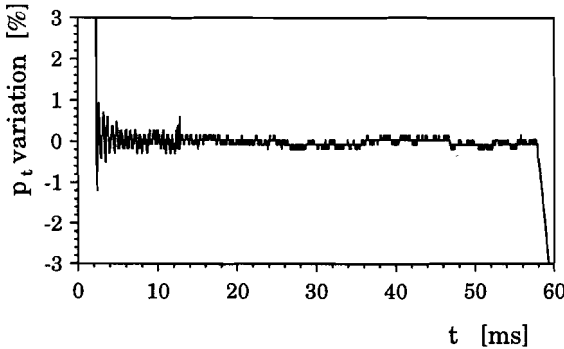


*Figure 3.19: The relative unsteady pressure fluctuation at the tube wall in the test section TS1b ($M = 0.09$ and $Re_u = 1.88 \times 10^6$ $[m^{-1}]$).*

estimate using Bernoulli's equation yields pressure fluctuations of the same order of magnitude as shown here, which is also confirmed by the experimental results of *Schneider and Haven* [1995].

At larger times scales during the test, it is found that the pressure ratio $p_t/p_i$, at the test section decreases a little. This effect may be explained by the development of thin boundary layers at the tube walls. Initially, the expansion wave creates a uniform velocity profile. However, due to viscosity unsteady developing boundary layers are initiated, which weakly influence the flow conditions in the tube.

The systematic change in pressure in the test time interval depends on the initial pressure and on the flow Mach number or instead, on the unit-Reynolds number and the Mach number. This systematic change of pressure can be expressed as a relative decrease of pressure during the test time interval. Because the Mach and unit-Reynolds numbers are related to the pressure, the former parameters are estimated from the latter using equation 3.5, etc.. Figure 3.20 shows the measured change of pressure and the corresponding calculated change in Mach and unit-Reynolds number at different unit-Reynolds numbers for a fixed average Mach number ($M = 0.33$). This figure shows a slightly larger change at a lower unit-Reynolds number, however, the dependence on the unit-Reynolds number is very weak.

The influence of the Mach number is shown in figure 3.21. It should be noted
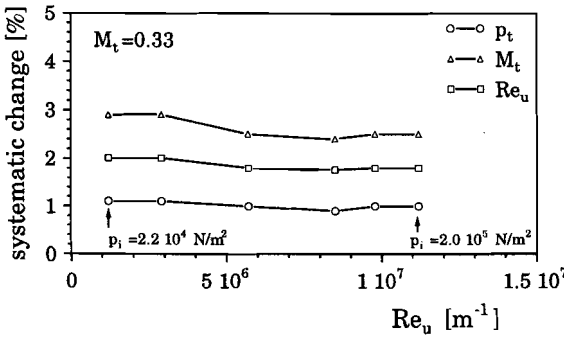
*Figure 3.20: The systematic change of the pressure, Mach and unit-Reynolds number as a function of unit-Reynolds number for equal orifice ('constant' Mach number). The Mach and Reynolds number variation is estimated from the pressure change measured.*

that no data are available for different Mach numbers with a constant unit-Reynolds number. However, the previous result shows a very weak influence of unit-Reynolds numbers so that data at different Reynolds numbers can probably be used to obtain a good impression of the influence of the Mach number. It is
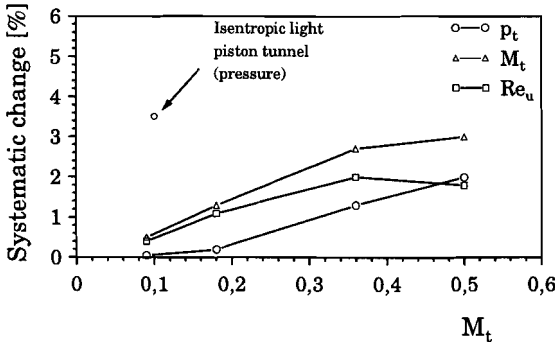


*Figure 3.21: Systematic change of the pressure (measured), Mach and unit-Reynolds number (estimated from pressure) during the test time interval as a function of the Mach number ($Re_u$ of data points from left to right: 1.8, 3.5, 6.0 and 7.5 $\times 10^6$ $[m^{-1}]$, respectively). The additional data point at $M = 0.1$ indicates a typical relative pressure variation in an isentropic light piston tunnel [Magari and LaGraff, 1991].*

observed that increasing the Mach number shows increasing variation. However, at higher Mach numbers it seems that the change in Mach and Reynolds number stabilizes at a certain value, whereas the variation of pressure still increases. According to equation 3.5 the Mach number becomes less sensitive to variations in pressure at higher Mach numbers. Hot-wire measurements show comparable percentages and trends for the smoothly changing mass flux. Since the latter measurement method combines mass flux and temperature change, the pressure

is to be preferred.

The variation in pressure of an Isentropic Light Piston Tunnel (ILPT) [*Magari and LaGraff*, 1991] has been added in figure 3.21 to indicate the accuracy of the Ludwieg tube. While the Ludwieg tube has a smooth change of 0.1% in pressure, a variation of 3.5% is found in the ILPT due to several shock and expansion wave reflections. Unfortunately, no information is found for higher Mach numbers.

Finally, it should be noted that the variation of flow conditions due to turbulent fluctuations dominates the (smooth) variation with longer time scales, particularly for higher free stream turbulence levels (e.g. figure 3.24).

### 3.5.3   Reproduction of experiment

Another important factor is the reproduction accuracy of the experiment. Theoretically, the accuracy is determined by the exactness with which the initial pressure and temperature can be imposed and recorded. The ambient temperature is read within $0.1 K$. This causes an error of $\pm$ 0.02% in the unit-Reynolds number over the whole range of unit-Reynolds number and Mach number. The ambient pressure is read from a barometer with an error of 0.1 $mmHg$, while the (calibrated) manometer can be read within 0.5 $mmHg$ causing a total inaccuracy in the initial pressure in the tube of 80 $Pa$. This maximum error is relatively larger for lower unit-Reynolds numbers at lower initial pressures. The relative error in unit-Reynolds number (due to an uncertainty of 80 $Pa$) is shown in figure 3.22 for different Mach numbers. This error is computed according to the relations for the flow conditions (equation 3.5 etc.). The accuracy was
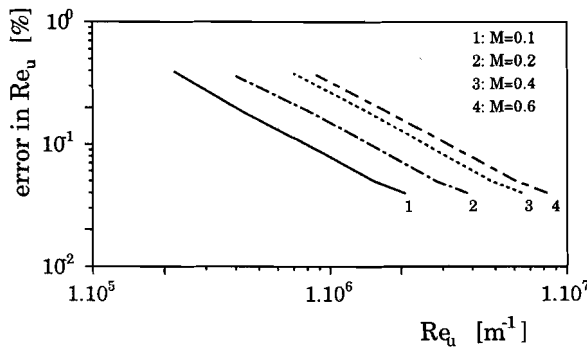


*Figure 3.22: Estimated relative error in unit-Reynolds number due to limited accuracy in pressure adjustment.*

tested by performing an experiment with test section TS1b with $M = 0.12$ and $Re_u = 2.4 \times 10^6$ $[m^{-1}]$. This experiment shows that the time averaged pressure reproduce within 0.05%. According to the relations for the flow conditions, the error in unit-Reynolds number is 0.05%. This corresponds with the predicted

accuracy in figure 3.22.

It can be concluded that the accuracy of condition reproduction is very high, in particular at high unit-Reynolds numbers and low Mach numbers. For the most inaccurate combination (low unit-Reynolds numbers and high Mach numbers, e.g. $M_t$=0.6 and $Re_u = 5 \times 10^5$ $[m^{-1}]$) the inaccuracy is still less than 0.8%.

### 3.5.4  Influence test section on flow conditions

Due to the additional objects in the test section (flat plate and turbulence grid) the flow conditions may be influenced. The investigation of the individual effects showed that neither the turbulence grids nor the flat plate in horizontal position have any influence on the averaged pressure. For the plate at maximum angle ($\approx 2.4°$) there is some influence. Figure 3.23 shows the upward shift in pressure measured and the estimated consequence for the Mach and unit-Reynolds number. An increasing influence is observed for increasing Mach number. However,
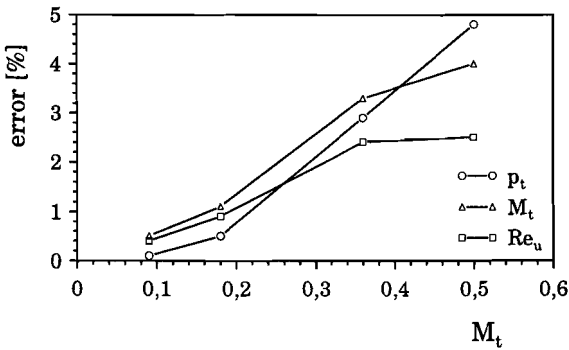


*Figure 3.23: Relative error in the pressure, Mach number and unit-Reynolds number for different Mach numbers. Test section TS4 is used with the plate at maximum angle (related to test section without plate).*

the influence becomes constant at higher Mach numbers.

### 3.5.5  Free stream turbulence level

Five different turbulence grids were applied to generate a free stream turbulence. These grids can be placed at two different upstream positions. In this section the turbulence level as a result of the different grids is studied at a fixed distance downstream of the grid. To determine the free stream turbulence level for each grid, the lower wire (right-hand figure 3.17) of probe 2 (2.5 $\mu m$ wire) has been employed at an overheat ratio of 1.7 (see appendix C).

Figure 3.24 shows an example of the mass flux fluctuation, $\rho u/\overline{(\rho u)_t}$, during test time for $M = 0.36$, $Re_u = 1.24 \times 10^6$ $[m^{-1}]$ and grid no. 3. Generally, the
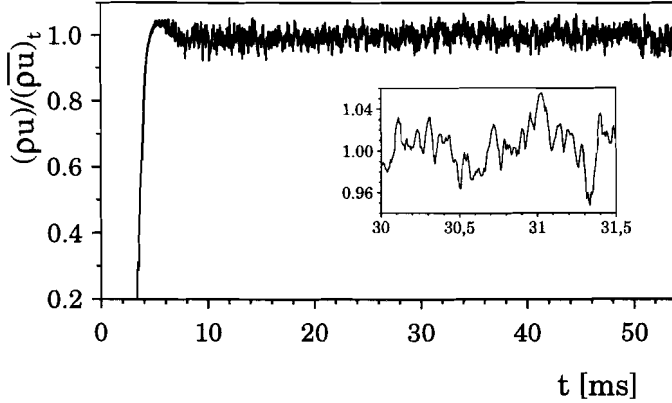
*Figure 3.24: Non-dimensionalized instantaneous mass flux measured above the leading edge of the plate for test section TS4, $M = 0.36$, $Re_u = 1.24 \times 10^6$ $[m^{-1}]$, $Tu=2.0\%$, grid no. 3, 140 mm upstream.*

turbulence level is very constant during the experiment. The relative difference between the first and second half of the test time is very small (about 1% to 2 %). For higher unit-Reynolds numbers ($\approx > 5 \times 10^6$ $[m^{-1}]$) sometimes differences up to 7% can be observed. A somewhat peculiar behaviour is obtained for the turbulence grid no. 1 at a Mach number of 0.36. For this combination the turbulence level increases with 14%. As the induced turbulence level with this grid is relatively low ($\approx 1.3\%$), the increasing natural free stream turbulence level of the Ludwieg tube may become dominant. Even if these larger variations are taken into account, the turbulence level is sufficiently constant to perform accurate measurements.

The turbulence level for the complete test time is reproduced within 4% (generally within 2%) for Mach numbers from 0.09 to 0.5 and unit-Reynolds numbers from $6.9 \times 10^5$ to $7.5 \times 10^6$ $[m^{-1}]$ (levels outside this range were not determined).

Variation of the turbulence level over the cross-section were not studied in detail. One single qualitative experiment using the upper wire was performed at $M = 0.18$ and $Re_u = 3.5 \times 10^6$ $[m^{-1}]$. This experiment demonstrated that no significant differences are present.

The effect of Mach number and unit-Reynolds number on the induced turbulence level were studied for all grids. The measurements for Mach numbers equal to 0.18 and 0.36 are represented in figure 3.25. From this figure, it can be seen that the free stream turbulence level depends on the unit-Reynolds number. Increasing viscous forces for decreasing unit-Reynolds numbers may cause extra dissipation, resulting in a lower free stream turbulence level. This is especially observed at higher turbulence levels and seems more pronounced for the higher Mach number. The fourth grid was placed further upstream, because at the
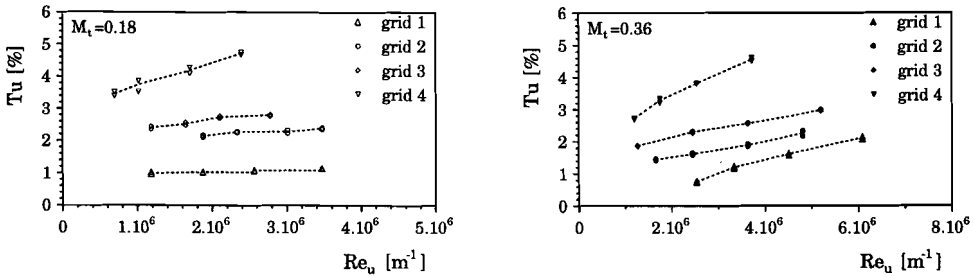
*Figure 3.25: Free stream turbulence level at leading edge of flat plate for various turbulence grids as a function of $Re_u$ and Mach number. M=0.18 (left-hand) M=0.36 (right-hand) (grid numbers 1, 2 and 3, 140 mm upstream, grid 4 at 200 mm). Each experiment was performed twice.*

closest upstream position the turbulence level was too high to obtain an initial laminar boundary layer at the flat plate with a sharp leading edge. For the same reason the turbulence level of the fifth grid was not studied in detail. As expected the lowest free stream turbulence level obtained with grid 1 is about 1%. The highest free stream turbulence level is obtained with grid number 5 at 140 *mm* upstream. Unfortunately, this turbulence level was not measured with probe 2 (2.5 $\mu m$ wire). However, a preceeding series of experiments with probe 1 (5 $\mu m$ wire, 4 times longer wire) was performed for all grid numbers. These measurements show a systematic underestimation (due to a too long wire) of about 30%. Measurements with this wire for grid number 5 showed free stream turbulence levels of 8 to 9 % for Mach numbers from 0.09 to 0.5. The 'real' free stream level is expected to be above 10%.

### 3.5.6   Range of Mach number, unit-Reynolds number and turbulence level

The upstream Mach number can be varied from 0.09 up to a value of 0.6. Independent of the Mach number, the unit-Reynolds number was varied starting from about $6 \times 10^5$ to over $1 \times 10^7$ $[m^{-1}]$ (figure 3.26). The practical upper limit for the unit-Reynolds number is determined by the maximum initial pressure allowed by the construction. The lower range is limited by too low an initial pressure difference over the diaphragm, which will cause incomplete membrane opening. Concerning boundary layers, the transition point can easily be adjusted to the plate length by adapting the unit-Reynolds number. The transition process can be realized across the whole sensor plate to obtain maximum spatial measuring accuracy.

The free stream turbulence level can be varied from 1% to 10% up to a Mach number of 0.36. Above this Mach number there are some difficulties with the coarser turbulence grids ($Tu > 2\%$) forming a critical area reduction.
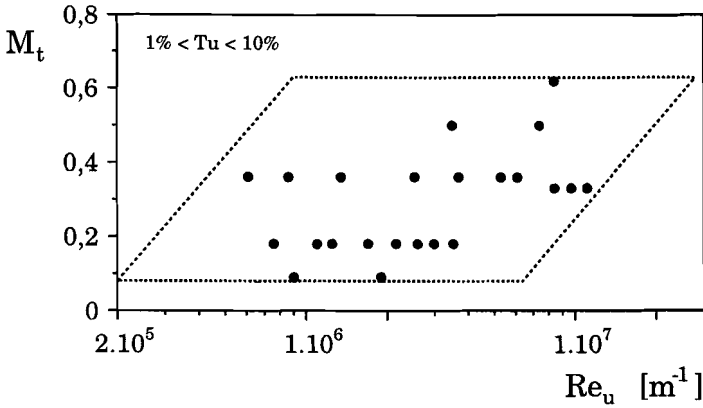
*Figure 3.26: The available two dimensional range for Mach and unit-Reynolds number represented by a quadrilateral for the Ludwieg tube as tested at this moment. The dots represent some experiments that have been performed.*

A method to increase the local Mach number is to mount an area reduction at the location of the flat plate. In this way a turbulence grid can still be applied with a subcritical opening area.

## 3.6    Comparison of experimental set-ups

In this last section a short evaluation is carried out. The Ludwieg tube is compared with two experimental facilities discussed earlier. At the end a different facility will be considered as an alternative: a combination of a *shock tube* and a Ludwieg tube.

### 3.6.1    Ludwieg tube versus atmospheric wind-tunnel

It is shown in the introduction that the atmospheric wind-tunnel is inadequate for boundary layer transition research at higher free stream turbulence levels and higher subsonic Mach numbers.

However, for free stream turbulence levels below about 1%, this set-up can be applied, just like the Ludwieg tube set-up. In both experimental facilities special measures must be taken (like screens and contractions) to reduce the natural turbulence level of the set-up (about 1% for the Ludwieg tube). Both facilities cope with comparable problems. The atmospheric wind-tunnel has the specific advantage that the test time is actually unlimited. Also, the conditions might be more constant. The Ludwieg tube has the particular advantage that the unit-Reynolds number can be varied for a constant Mach number.

### 3.6.2   Ludwieg tube versus ILPT

Both the Ludwieg tube and Isentropic Light Piston Tunnel have the advantage that the Mach and unit-Reynolds number can be independently varied across a wide range. The Isentropic Light Piston Tunnel has the additional benefit that the gas-to-wall temperature ratio is an extra independent parameter, with which high gas temperatures can be created. Moreover, the test time is several times larger. It is not clear whether sufficiently low unit-Reynolds numbers can be created.

The Ludwieg tube has the specific advantage that the flow conditions are very constant. In addition the accuracy of reproduction is very high. The relatively low experimental costs are an added bonus. Due to the simple construction without moving parts, the set-up is reliable and relatively cheap.

Concerning the realization of free stream turbulence and higher subsonic Mach numbers, both set-ups behave comparably.

### 3.6.3   Ludwieg tube versus a shock tube driven Ludwieg tube

Parallel to the performance study of the Ludwieg tube (as discussed in this chapter) the performance of a shock tube as a driver for the Ludwieg tube was investigated. The principle and results of this tube set-up are presented in appendix A. Both the Ludwieg tube and shock tube set-ups were employed parallel until the final test section. For the comparison in this section the first major results of the shock tube driven Ludwieg tube will be given.

Concerning the range of unit-Reynolds number and Mach number, both the Ludwieg tube and shock tube perform comparably. In both set-ups these two flow parameters can be varied independently. Just like the Isentropic Light Piston Tunnel, the shock tube has the extra advantage that the gas-to-wall temperature ratio is an extra independent parameter. This gives the opportunity to generate high gas temperatures. With respect to condition reproduction, both set-ups perform very well.

A difference in performance concerns the constancy of flow conditions. With a slowly increasing pressure (10 %), the conditions in the shock tube are clearly less constant than the conditions in the Ludwieg tube (1% during 55 $ms$ for $M_t$=0.33). Another disadvantage of the shock tube is the short test run time of about 11 $ms$. A third problem typical for the shock tube, is the natural turbulence level, which is between 2% and 6% [*Trolier and Duffy*, 1985]. This limits the range of turbulence level significantly at the lower side. A minus of the original Ludwieg tube is the significantly lower heat flux level.

# 3.7  Conclusion and discussion

This chapter dealt with the performance of the Ludwieg tube with respect to boundary layer transition research at subsonic Mach numbers at higher free stream turbulence levels. It has been shown that this experimental facility combines constant and reproducible flow conditions with a wide independent range of Mach numbers, unit-Reynolds numbers and free stream turbulence levels. In a parameter range where an atmospheric wind-tunnel has essential shortcomings, the Isentropic Light Piston Tunnel is not that flexible and accurate, and the shock tube yields too short test time, the Ludwieg tube performs very well.

A disadvantage of the Ludwieg tube is the relatively low heat flux level compared to the piston tunnel (about five times less). The conventional heat flux measurement technique with cold thin film gauges is less adequate for performing accurate heat transfer measurements. For this reason the measuring technique needs to be improved (this will be discussed in the next chapter). With the optimized measuring technique applied, the Ludwieg tube is a successful experimental facility for the range under consideration.

# Chapter 4

# Heat transfer measurements

For this work several different measuring techniques are employed to determine different quantities. Heat flux gauges at a flat plate are used to measure the heat transfer in transitional boundary layers. From these measurements information can be obtained with respect to transition parameters.

The measuring technique employed (cold thin film gauges) is convenient for transient experimental facilities like the Ludwieg tube. This technique is not standard however. In this chapter the development of a well defined and optimized sensor design is discussed.

## 4.1  Cold thin film gauges

To obtain information from a transitional boundary layer, hot wire anemometry is often applied. However, in this work metal thin film gauges have been employed for several reasons. Firstly, we are interested in the heat transfer rate to the wall. Contrary to hot wire anemometry where the heat transfer rate is determined indirectly, thin films provide the primary parameter of interest. Secondly, in natural transition it is difficult to determine spot parameters without using more probes simultaneously. Upstream probes may not affect the downstream flow. Thirdly, the boundary layers in high-speed flow are thin ($\delta_l < 10^{-3}\ m$), which do not make the application of hot wires straightforward.

Many techniques are available for heat flux measurement [*Abtahi and Dean,* 1990]. However, due to the several requirements that must be satisfied, the application of most techniques fail. To measure the heat transfer rate in a subsonic transitional boundary layer, the measuring technique must be fast. A response frequency band ranging from 20 $Hz$ to at least 30 $kHz$ is required to determine the velocity of the passing turbulent spots with sufficient accuracy. The second requirement concerns the geometrical dimension. To prevent flow disturbance, the technique may not be too intrusive. A third aspect concerns the manufacturing of the sensor. A complicated sensor lay-out is necessary to measure different

transition phenomena, therefore the fabrication must be relatively simple.

Only thin film gauges satisfy these requirements without concessions. This technique is fast, does not disturb the flow and allows damping, sputtering or painting on an electrically insulated substrate such that complex lay-outs can be obtained.

The principle of thin film gauges is based on the fact that the metal film resistance depends on its temperature. Thin film gauges are usually applied in one of two different modes: as a hot film (analogous to hot wire anemometry) or as a cold film (operated as a resistance temperature device (RTD)). The hot film is usually operated in a constant temperature (CT) mode and applied in a steady-state flow [*Bruun*, 1995]. In the steady flow situation the substrate surface temperature equals the gas temperature, except at and in the vicinity of the thin film where the sensor is kept at a higher temperature (e.g. $180^{\circ}C$) causing a steady flux into the substrate. The varying part of the flux supplied, is a result of the flow and a calibration in steady flow makes this method useful. In a transient flow (e.g. Ludwieg tube) the flux of the sensor into the substrate is not constant since the whole surface is cooled down (or heated for a shock tube or ILPT) and consequently the same holds for the vicinity of the sensor. The CT film supplies extra power to the substrate to eliminate the temperature decrease of the substrate [*O'Brien*, 1990]. Additionally, power is supplied to the cooling gas flow. An additional effect of hot film gauges in general is the thermal interference of the gauges due to heated wakes. Cold thin film gauges avoid these difficulties and are often applied in transient facilities [*Schultz et al.*, 1980]. Because in this technique the film does not play an active role, it does not influence the process. The cold thin film technique is applied in this work.

## 4.1.1   Cold thin film gauge principle

Thin film sensors make use of the effect that the electrical resistance of a metal film is temperature dependent. For sufficiently thin layers the thermal mass can be neglected. This implies that thin film gauges can serve as a temperature sensor, measuring the unsteady surface temperature. The substrate layer has to be sufficiently thick to stop the thermal boundary layer from reaching the bottom within the test time. In this case a semi-infinite assumption is valid. The time required for a step-wise change in temperature to reach the back substrate surface is given by *Diller* [1993]

$$t = \frac{\rho c H^2}{16k} \tag{4.1}$$

where $H$ is the substrate thickness, $k$ the thermal conductivity, $\rho$ the density and $c$ the heat capacity of the substrate material. This relation is used to estimate the thermal penetration depth in the substrate for the experiments performed ($t \approx 50\ ms$) being $\delta \approx 0.6\ mm$.

With known thermal substrate properties the flux can be reconstructed from

the surface temperature history, by solving the unsteady heat conduction equation for the substrate layer. Due to a low measuring current the internal dissipation has to be sufficiently low to prevent the influence of heating. A disadvantage of this method is that knowledge on substrate properties and the resistance temperature coefficient of the sensor is necessary.

The electrical resistance of a thin film gauge with length $l$, is given by [*Bruun*, 1995]

$$R_g = \int_0^l \frac{\chi_g}{h.w} dz \tag{4.2}$$

where $h$ is the gauge height, $w$ is the gauge width, $l$ is the gauge length (figure 4.1) and $\chi_g$ is the gauge resistivity. The latter is in linear approximation (for a small temperature interval):

$$\chi_g = \chi_0[1 + \alpha_0(T_g - T_0)] \tag{4.3}$$

where $T$ is the temperature, $\alpha$ is the temperature coefficient of resistivity and the indices $g$ and $0$ refer to the present and reference situation of the gauge. These relations even hold very well for very small, thin layers. For constant $l$, $h$, $w$ and
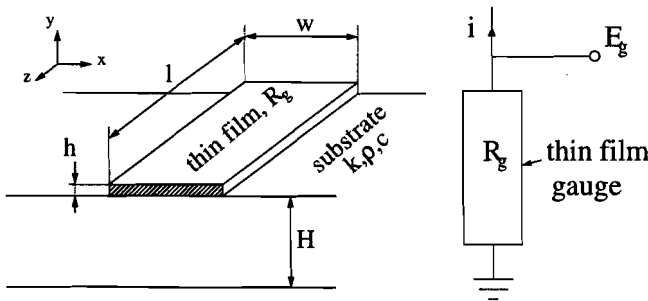


Figure 4.1: Sketch of a thin film gauge (left-hand) on a substrate with descriptive dimensions (not in scale). The right-hand figure shows the sensor in the electrical circuit with a constant current.

$\chi_g(z)$ the gauge resistance can be written as

$$R_g = \frac{\chi_g l}{hw} = R_0[1 + \alpha_0(T_g - T_0)] \tag{4.4}$$

A constant current source can be used to measure the electrical resistance variation. This method is more accurate than the Wheatstone bridge (which was used in test section TS3), because in the Wheatstone bridge-circuit the effect of resistance variation on voltage change is partially annuled by a decreasing current (because the bridge voltage must be constant). For a constant current source the voltage variation $\Delta E$ (right-hand figure 4.1) is related to the temperature as:

$$\Delta E = E_g - E_0 = i(R_g - R_0) = E_0 \alpha_0(T_g - T_0) \tag{4.5}$$
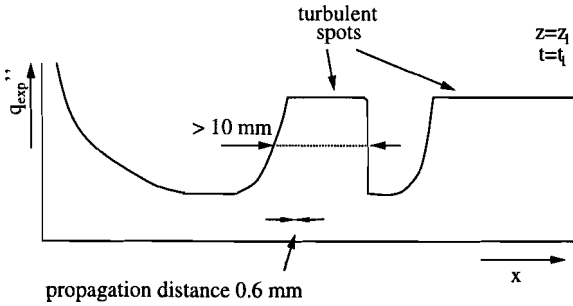
*Figure 4.2: Sketch of experimental heat flux at a flat plate at a certain time and certain cross-section. A laminar heat flux with turbulent spots imposed causes a one-dimensional heat flux for the thin film gauges.*

with $i$ the constant current through the sensor, and $E_0$ the initial voltage across the sensor. This equation shows that in order to maximize the sensor output $E_0$, $\alpha_0$ and $T_g - T_0$ should be as high as possible.

## 4.1.2  One-dimensional assumption and superposition principle

Due to the temperature difference between the expanded gas and flat plate heat transfer occurs. For the reconstruction of the experimental heat flux, a one-dimensional heat conduction is assumed [*Schultz et al.*, 1980]. In this section we show that this assumption is justified.

The heat flux signal can be considered to be composed of a laminar basis flux (which is uniform for the domain of influence) with turbulent spots superposed (figure 4.2). The spots, having a characteristic size of 1 $cm$ to 10 $cm$, are much larger than the zone of influence ($\delta \approx 0.6$ $mm$).

Furthermore, the convective spot velocity over the surface is 20 $m/s$ to 100 $m/s$, which is much faster than the thermal diffusion velocity in the substrate. This implies that the thin film senses the turbulent spot as an abruptly rising flux level, which is much wider than the influencing zone.

Another assumption that has been made is the superposition principle. Due to the electrical current through the sensor, ohmic dissipation occurs. The dissipated power divided over the gauge surface results in a steady dissipation flux $q''_{diss}$. This dissipation flux can be larger than the experimental heat flux that has to be measured. Although this flux may be quite high, the temperature rise is not large, as will be seen later on. Since the heat conduction equation is linear, the superposition principle holds, which means that the steady dissipation flux can be considered absent, provided that the steady situation is taken as reference situation. A possibly superfluous two-dimensional numerical simulation that was carried out, showed that this assumption is justified. This principle has been
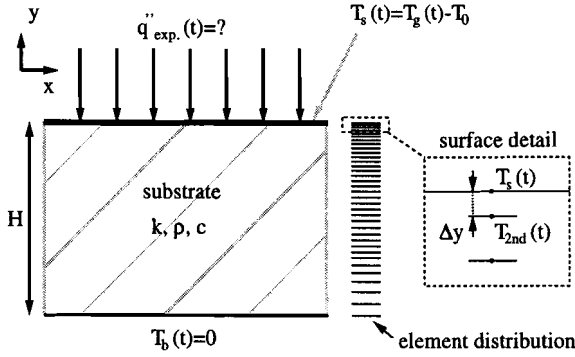
*Figure 4.3: Numerical domain for the reconstruction of the unsteady heat flux at the top. The boundary conditions are prescribed for the surface and bottom. The element distribution is shown on the right-hand side.*

checked experimentally by *O'Brien* [1990]. He varied the ohmic flux up to the measured heat flux and found a negligible effect.

## 4.1.3 Flux reconstruction

According to *Diller* [1993], the presence of the film in the heat conduction process can be neglected while the film is negligibly thin (70 *nm* in the present study). This has been verified with a numerical simulation which justified this assumption.

The heat conduction for the substrate is given by the one-dimensional heat conduction equation

$$\rho c \frac{\partial T}{\partial t} = \frac{\partial}{\partial y}\left(k\frac{\partial T}{\partial y}\right) \tag{4.6}$$

where $\rho$, $c$ and $k$ are the substrate density, heat capacity and conductivity, respectively. The boundary conditions are given by

$$T_s(t) = T_g(t) - T_0 \tag{4.7}$$

$$T_b(t) = 0 \tag{4.8}$$

where the indices $s$ and $b$ refer to surface and bottom quantity, and $T_g(t) - T_0$ is the measured temperature according to equation 4.5 (figure 4.3). A second order accurate finite volume method with a first order accurate fully implicit time integration was applied to numerically solve the unsteady heat conduction problem. 30 elements were used over the substrate domain with grid refinement at the surface. The experimental sample time was used equal to the numerical time-step, which was found to be sufficiently small. The flux at the top is reconstructed

by the computation of the heat flux over the first element

$$q''_{exp}(t) = k_{sub} \frac{T_s(t) - T_{2nd}(t)}{\Delta y} \tag{4.9}$$

where $T_{2nd}(t)$ is the solved temperature in the second nodal point and $\Delta y$ the size
of the first element (see figure 4.3). It should be noted that this reconstruction is
first order accurate and that the heat storage in the first element is neglected. The
effect of that was verified with a flux step function as test case. The analytical so-
lution of this test case is known. It turns out that the error in flux reconstruction
after the first time step, with correction for heat storage, decreases from 0.5% to
0.07%. This shows that even ignoring the heat storage in the first element the
reconstruction is sufficiently accurate. A typical example of this reconstruction
is presented in figure 4.4. The left-hand figure shows the measured temperature
$T_g(t) - T_0$. The reconstructed heat flux from this temperature is displayed in the
right-hand figure. This example shows that the weak noise level present in the
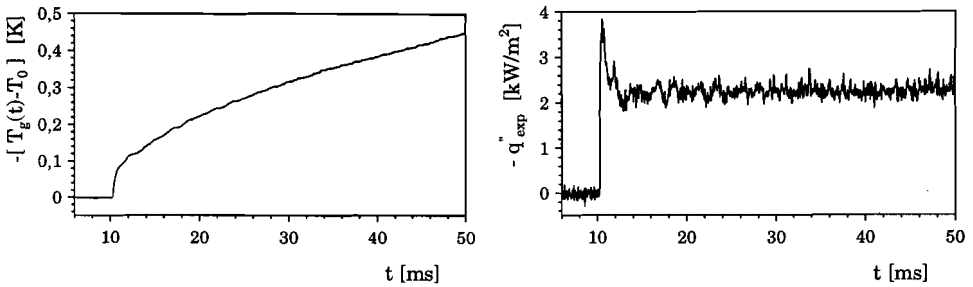


*Figure 4.4: Left-hand figure shows the thin film temperature measured during an
experiment in the Ludwieg tube ($Re_u = 4.9 \times 10^6$ [$m^{-1}$], $M$=0.36, $x_{gauge}$=53
mm). In the right-hand figure the reconstructed heat flux is plotted. A detail of
the noise level is shown in figure 4.15.*

temperature measured is strongly present in the reconstructed heat flux. The
origin of this noise will be discussed in section 4.4.

Sometimes an electrical analogue is applied to obtain the flux on-line [*Doorly
and Oldfield*, 1986]. This technique proved to work quite well. Since a complete
electrical circuit is required for each sensor, this technique was not applied.

## 4.2    Design guidelines for cold thin film gauges

As concluded from figure 4.4, the sensor accuracy is strongly determined by the
signal-to-noise ratio. To obtain a maximum signal-to-noise ratio the sensor output
must be maximized with respect to the noise level. Equation 4.5 shows that in
order to obtain a maximum output, the voltage across the film gauge must be
as high as possible provided that the noise level is constant. On the other hand

the acceptable sensor voltage is limited. Too high a voltage causes too much dissipation, resulting in high sensor temperatures.

For an optimized cold thin film gauge, a balance must be obtained between the increasing accuracy as a result of higher voltage and decreasing accuracy due to thermal effects as a result of increasing dissipation. With design rules that account for these effects, the design can be tuned leading to an optimized accuracy.

Unfortunately, nothing more than a few rules of thumb have been found in literature for the design of cold thin film gauges. According to *Diller* [1993] the sensor resistance should be at least 100 $\Omega$. For these gauges a current of 1 to 2 $mA$ provides a good result. *O'Brien* [1990] presents a relation to keep the surface heating (due to convective flux) under control to prevent too large a drop in the heat flux. *Epstein and Guenette* [1986] report that the supply voltage is constrained by the dissipation in the film sensor given by

$$q''_{diss} = \frac{P_{diss}}{A_{sensor}} = \frac{i^2 R_g}{lw} = \frac{E_g^2 h}{l^2 \chi_g} \tag{4.10}$$

which should be kept small (in contradiction with *O'Brien* [1990]) compared to the heat flux being measured. This equation combined with equation 4.5 leads to the conclusion that long thin films with a high sensitivity $(= \alpha \sqrt{\chi})$ give the optimum design.

The lack of design rules can be partially attributed to the conditions in the experimental facilities in which this principle is applied. In these facilities the temperature between highly convective flow and object usually is 150 $K$ or more. First, this implies that the heat flux is large (strong signal) and second, the relative effect of, for example, sensor heating due to electrical current is relatively small. With temperature differences of 20 to 30 $K$ the Ludwieg tube has considerably lower values. Therefore, a more sophisticated way to design a cold thin film sensor is required as stated in the previous chapter. However, an improved thin film will also improve the results in the former set-ups, where larger temperatures are available.

In this chapter some quantitative estimates of the accuracy of cold thin film gauges are specified.

The first effect that has to be taken into account is the unsteady surface heating during an experiment. Due to the heat flux the surface will be cooled (or heated). Depending on the substrate properties, the unsteady temperature decrease may cause a decreasing temperature difference between gas and plate, which causes a decreasing experimental heat flux.

As a result of the electrical current there will be a heat flux due to dissipation, as discussed by *Epstein and Guenette* [1986]. As shown by *O'Brien* [1990] this flux may be comparable with the experimental heat flux. Because the superposition principle may be applied this effect does not play any role. However,

changing the surface temperature during the experiment will cause a changing sensor resistance and thus a changing flux due to dissipation. Since this change is induced by the time scale of the experiment it should be much smaller than the flux to be measured.

A third effect that must be taken into account is the sensor heating due to dissipation. The increase of sensor temperature must be small enough to avoid this to be an essential contribution in the transfer process during the experiment. It will be shown that it is quite possible to predict the thin film surface temperature as a result of steady dissipation. Quantification of these effects leads to a design guideline. It will be shown that the accuracy of cold thin film gauges can be improved significantly using these design guidelines. The optimization is achieved by tuning the supply voltage, the value of electrical resistance, and the geometrical configuration of gauge and substrate.

Before these design guidelines are discussed it is important to note that the noise level is hardly affected by the voltage across the sensor and by the value of electrical resistance. This was verified experimentally for voltage levels between $1\ V$ and $50V$ and resistances between $100\ \Omega$ and $2.10^4\ \Omega$. This means that both the voltage level and sensor resistance can be chosen freely over a wide range.

### 4.2.1 Unsteady surface heating

The first restriction is formed by the requirement that the unsteady surface cooling due to convective heat transfer must be smaller than $\Delta T_{exp}$, the temperature difference between gauge and gas (as was shown by *O'Brien* [1990]). This yields:

$$\frac{T_g(t) - T_0}{\Delta T_{exp}} < \xi_1 \tag{4.11}$$

where $T_g(t)$ is the unsteady gauge temperature, $T_0$ the initial gauge temperature, $\Delta T_{exp}$ the temperature difference between gas and sensor (which is assumed to be known), and $\xi_1$ the acceptable ratio of surface heating and experimental temperature difference.

The surface cooling $T_g(t) - T_0$, is a result of the convective heat flux called the experimental flux $q_{exp}^"$, of which the value is also assumed to be known. When this experimental flux is approximated as a step function in time (which is a quite good approximation according to figure 4.4, all the more because this especially concerns the smooth temperature drop) starting at $t = 0$, the time-dependent temperature is given by [*Incropera and De Witt*, 1990]:

$$T_g(t) - T_0 = \frac{2q_{exp}^"}{\sqrt{(\rho ck)_{sub}}}\sqrt{\frac{t}{\pi}} \tag{4.12}$$

where $t$ is the time in seconds and $(\rho ck)_{sub}$ is the product of the substrate parameters involved. To maximize the sensor output (according to equation 4.5),

the instationary temperature change $T_g(t) - T_0$ should be as large as possible. On the other hand it is limited according to equation 4.11. For a given tolerance $\xi_1$, the combination of equations 4.11 and 4.12 leads to

$$\frac{2q_{exp}^{''}}{\Delta T_{exp}} \frac{\sqrt{\frac{t}{\pi}}}{\sqrt{(\rho ck)_{sub}}} < \xi_1 \tag{4.13}$$

In most cases the experimental heat flux and temperature difference can not be chosen freely. The experimental heat flux is a function of $x$, and thus the maximum averaged experimental heat flux should be taken (this flux is most critical). Moreover, for transient experimental facilities the test time is also more or less imposed. This implies that the single group of parameters that can be varied is given by $(\rho ck)_{sub}$, which determines the choice of substrate material.

While making a choice other aspects also must be taken into account. The substrate must be an electrical insulator. Also, the fabrication process of a thin film must be kept in mind. The substrate temperature can rise up to $300^oC$ depending on whether sputtering or damping is applied. Each sensor material (e.g. Ti, Ni or Pt) requires a different temperature during the manufacturing process.

Glass was used as a substrate material (B270-glass), with substrate properties specified by the manufacturers within $\pm$ 1% ($k$=0.92 $W/mK$, $\rho$=2550 $kg/m^3$ and $c$= 860 $J/kgK$). However, these values hold for the bulk material. At the surface the properties may deviate. A calibration to eliminate this uncertainty is discussed further on.

## 4.2.2   Ohmic heat flux change

Another requirement concerns the change of dissipation flux $\Delta q_{diss}^{''}$, during the experiment. This must be smaller than the convective heat flux that has to be measured. Due to small sensor dimensions, together with high voltage and the change of resistance during the experiment, the dissipation flux change can be significant. This effect is important because it is coupled to the test run time scale. This means that

$$\frac{\Delta q_{diss}^{''}}{q_{exp}^{''}} < \xi_2 \tag{4.14}$$

where $\Delta q_{diss}^{''}$ is the change in dissipative heat flux during the experiment due to changing sensor resistance, $q_{exp}^{''}$ is the experimental heat flux, and $\xi_2$ the acceptable ratio. $\Delta q_{diss}^{''}$ is related to the change in resistance during experiment $(R_g(t) - R_0)$ according to equation 4.4 and 4.10 and is given by

$$\Delta q_{diss}^{''} = q_{g,diss}^{''} - q_{0,diss}^{''} = \frac{E_0^2 h}{l^2 \chi_0} \alpha_0 (T_g(t) - T_0) \tag{4.15}$$

This relation together with the expression for unsteady surface heating (equation 4.12 and 4.14) lead to the important expression:

$$\frac{\Delta q''_{diss}}{q''_{exp}} = \frac{E_0^2 h}{l^2} \frac{\alpha_0}{\chi_0} \frac{2\sqrt{\frac{t_{test}}{\pi}}}{\sqrt{(\rho c k)_{sub}}} < \xi_2 \qquad (4.16)$$

The group of parameters $(E_0^2 h)/(l^2 \chi_0)$ is the steady ohmic heat flux $q''_{diss}$.
With this relation many decisions can be made with respect to the choice of sensor material and the raising of the sensor output for example. As regards the sensor material choice, the relation for sensor output, equation 4.5, should be kept in mind.

In relation 4.16 several groups of parameters can be distinguished: a group determined by sensor geometry and sensor voltage ($E_0, h, l$), a part with sensor properties ($\alpha_0, \chi_0$), a substrate contribution ($\rho c k)_{sub}$, and an experimental influence ($\sqrt{t_{test}}$). In the previous section the substrate properties were determined by the choice of substrate material. Also, the test time of the experiment is known. The choice of sensor material is based on the separate effects of $\alpha_0$ and $\chi_0$. Relation 4.16 written explicitly for $E_0$ with keeping all parameters constant, except $\alpha_0$ and $\chi_0$, can be substituted into equation 4.5 to show that the sensor output is proportional to $\sqrt{\chi_0 \alpha_0}$. Therefore, the sensor with the maximum value of the quantity $\chi_0.\alpha_0$ should be taken. It is important to remark that this conclusion is different from the conclusion of *Epstein and Guenette* [1986] who stated that $\sqrt{\chi_0}.\alpha_0$ should be maximized. The difference between these two conclusions can be explained by the following. In the present work the limit is not imposed by the ohmic heat flux (as is the case with Epstein). It is determined by the change of ohmic heat flux, which is additionally influenced by $\alpha_0$ (see equation 4.16).

In practice, the number of gauge materials is very limited because many aspects must be taken into account like the fabrication process (damping, sputtering, painting), sensitivity to corrosion, etc. According to the first right-hand term the sensor output is proportional to the inversed square root of film height $h$, which should therefore be as small as possible (high electrical resistance, less dissipation). It should be remarked that sensor properties like $\alpha_0$ and $\chi_0$ more strongly depend on the film thickness $h$ for $h$-values smaller than about 0.1 $\mu m$. This thickness is taken as the lower limit in this work. For thin layers $\alpha$ will generally decrease while the resistivity $\chi$, increases (the dependency is not specified). In order to make a choice out of different sensor materials, the dependency can be approximated to be equal for all materials. In the measurements performed in the scope of this work, the film properties for titanium are found to be: $\chi_{ti,bulk} = 4.2 \times 10^{-7} \ \Omega m$, $\chi_{ti,film} = 7.8 \times 10^{-7} \ \Omega m$, $\alpha_{ti,bulk} = 3.5 \times 10^{-3} \ K^{-1}$, $\alpha_{ti,film} = 1.8 \times 10^{-3} \ K^{-1}$. These values also depend on the process used to create the film. Hence, a small test object is made to obtain reliable values before making the final design.

The first factor in the right-hand term in equation 4.16 also shows that the

sensor length has a strong influence on the sensor voltage allowed. The dependency is linear (which was also found by *Epstein and Guenette* [1986]). This is explained by the fact that increasing the length at a constant $E_0$ increases both the sensor resistance (causing less dissipation at constant voltage) and the projected area (less dissipation per unit area). The length should be as long as possible. However, it is limited by the phenomena or quantity that must be measured (or effects that must not be measured). The sensor width $w$, does not play a part in this process because decreasing width causes linearly increasing film resistance and linearly decreasing projected area ($q_{diss}^{"}$ is constant). On the basis of these considerations the maximum sensor voltage allowed can be computed.

### 4.2.3   Heating due to ohmic heat flux

An aspect that has not been taken into account yet is the temperature increase of the sensor as a result of the dissipation flux. The resulting temperature increase is strongly influenced by the sensor width, as will be shown in this section. If this sensor width is not taken into account, the sensor voltage $E_0$, obtained from the previous section can not be realized because the sensor temperature is too high. For the sensor temperature increase $\Delta T_{diss}$, it is assumed that the ratio with the experimental temperature difference must be smaller than $\xi_3$:

$$\frac{\Delta T_{diss}}{\Delta T_{exp}} < \xi_3 \tag{4.17}$$

where the experimental temperature difference $\Delta T_{exp}$, is known and $\Delta T_{diss}$ must be specified. It would be useful to have a relation between the latter parameter and $q_{diss}^{"}$.

The sensor temperature increase is determined by a heat conduction problem governed by the heat input via the sensor, the dimensions of the sensor and the properties and dimensions of the substrate (figure 4.5). Since the sensor length in the present work is 10 to 40 times larger than the substrate thickness, the heat conduction problem can be reduced to a 2-D problem in $(x, y)$-plane (for lower $l/H$-ratios the situation is more 3-D. The following derivation will overestimate the temperature rise in this case, and will therefore be on the 'safe' side).

The 2-D heat conduction problem can be simplified to the domain with the boundary conditions as shown in figure 4.6. Here, a cross-section of the sensor with sensor width $w$, on a piece of substrate of width $W$ and height $H$ in $(x, y)$-plane is chosen. Variation of domain geometry shows that the side walls play a negligible role in the conduction process if $W/H > 4$ and $W/w > 4$. In this case the side wall boundary conditions may be taken to be $\partial T/\partial n = 0$ or $T = 0$[1]. The boundary condition at the bottom for this problem is taken equal to the

---

[1]This implies that the distance between two succeeding sensors should have at least the distance $W > 4w$ and $W > 4H$. In practice this will not be a restriction. In the present work the distance between the succeeding sensors is more than two times this 'critical distance'.
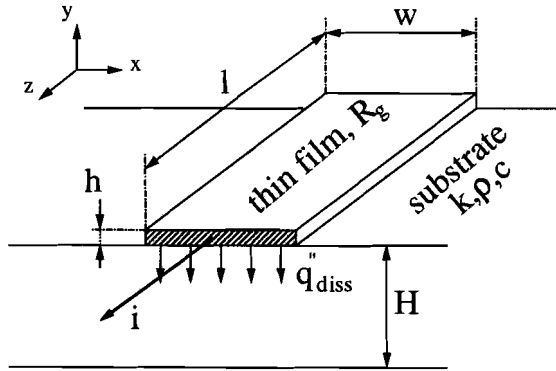
*Figure 4.5: Schematic drawing of a thin film gauge deposited on a substrate plate, with the descriptive length scales (not in scale). Due to the electrical current through the sensor, internal dissipation will generate a heat flux into the substrate layer, causing sensor heating.*

homogeneous Dirichlet condition (i.e. $T = 0$), because this side is mounted on a metal construction, which can be seen as a heat sink.

The thin film provides the heat flux equal to $q_{diss}^{''}$ over width $w$, while the rest of the surface is taken to be adiabatic ($\partial T/\partial n = 0$). For this configuration the relation between the specific dissipation flux $q_{diss}^{''}$, and resulting temperature rise $\Delta T_{diss}$, in the middle of the sensor will have the form:

$$q_{diss}^{''} = k_{sub}\frac{\Delta T_{diss}}{H}g(H/w) \tag{4.18}$$

where $k_{sub}$ is the thermal conductivity of the substrate, and $g(H/w)$ a function that accounts for the two-dimensionality of the heat conduction problem (a kind of Nusselt number). The function $g(H/w)$ is determined by means of numerical simulations for several $H/w$ ratios using a finite element package (Sepran). The result is shown in figure 4.7 by means of the triangles. The solid line represents a least-squares fit of a second degree polynomial through the computed points, which leads to

$$g(H/w) = 1.0 + 0.65(H/w) - 1.3 \times 10^{-3}(H/w)^2 \tag{4.19}$$

The numerical simulation was verified with experiments, using two different $H/w$ ratios ($H/w = 20$ and $100$). In these experiments the substrate thickness is 1 $mm$ and sensor width $\times$ length is $10\mu m \times 9\ mm$ and $50\mu m \times 40\ mm$. The sensor temperature was measured using relation 4.4, the $\alpha_0$-value was determined within 5% by means of a calibration in an oven. By prescribing $q_{diss}^{''}$ and using equation 4.18 the data points in figure 4.7 (filled triangles) can be found. The boundary condition $T = 0$ was imposed by pasting the substrate with conductive
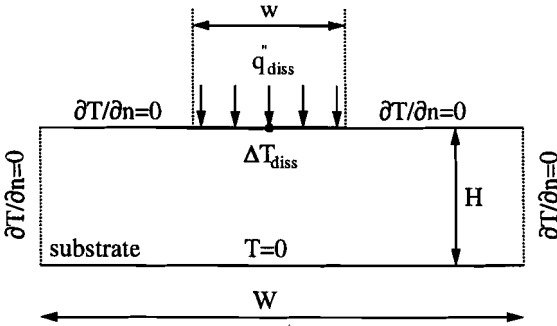
*Figure 4.6: Two-dimensional domain for the heat conduction problem together with the featuring dimensions and boundary conditions.*
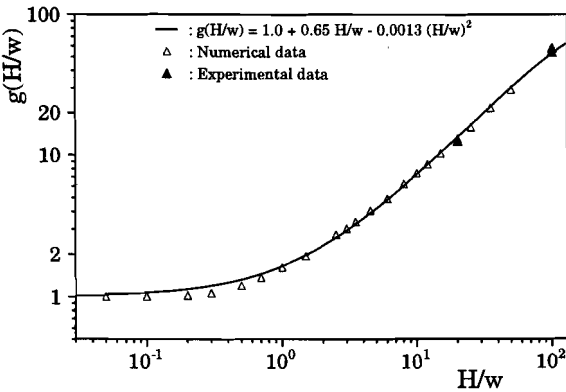


*Figure 4.7: The function $g(H/w)$ that relates temperature rise at the sensor (as a result of internal heat generation in the sensor) to the $H/w$ ratio.*

paste on a block of brass. It can be seen that the experiment corresponds well with the numerical predictions.

Several conclusions can be drawn from this. It can be seen that for sensors with a large width compared to substrate thickness (low $H/w$ ratio) the function $g(H/w)$ becomes equal to one, which implies a nearly one-dimensional situation. For decreasing sensor width (larger $H/w$ ratio) the resulting temperature decreases proportionally to $1/g(h/w)$ for equal dissipative heat flux $q''_{diss}$. In other words, a higher dissipation heat flux (higher voltage and thus higher accuracy) is allowed for larger $H/w$ ratios resulting in an equal temperature rise. This is explained by the fact that the heat can easily flow sideways. This result shows that the $H/w$ ratio should be as large as possible at a fixed substrate thickness $H$. Another result from the numerical simulations is that the time needed to obtain a steady conduction situation is less than 100 $ms$. This means that after switching on the equipment, one has to wait about one second before the experiment can start.

With the solution for $g(H/w)$ a relation is obtained between $\Delta T_{diss}$ and $q''_{diss}$. Together with equations 4.17 and 4.18 this leads to:

$$\frac{\Delta T_{diss}}{\Delta T_{exp}} = \frac{H}{g(H/w)} \left(\frac{E_0}{l}\right)^2 \frac{h}{\chi_0 k_{sub} \Delta T_{exp}} < \xi_3 \qquad (4.20)$$

From this result it can be concluded that:

- The substrate height $H$, should be as small as possible because the effect of $H$ on $\Delta T_{diss}$ is stronger than $g(H/w)$. The minimum size is determined by the displacement of the thermal boundary layer during the test time and can be derived with equation 4.1.

- $g(H/w)$ should be as large as possible, giving a maximum ratio for $H/w$. An important improvement can be obtained with this ratio.

The sensor output is (for a given heat flux) proportional to $E_0/\sqrt{k}$ (see equations 4.5 and 4.12). The restriction of equation 4.20 requires that $E_0$ is proportional to $\sqrt{k}$. Consequently the heat conductivity does not affect the sensor output. This implies that the thermal conductivity is not important in the choice of the substrate material.

In accordance with section 4.2.2 where $q''_{diss}$ was calculated, the required film width can be computed from equation 4.20. If too small a sensor width is calculated, leading to manufacturing problems, the voltage across the sensor should be reduced.

For a constant value of the parameters $H, l, h, \chi_0, k_{sub}, \Delta T_{exp}$ and $\xi_3$ (which normally is the case) relation 4.20 can be written in an explicit form for the voltage allowed across the sensor as a function of $H/w$:

$$E_0 = C.\sqrt{g(H/w)} \qquad (4.21)$$
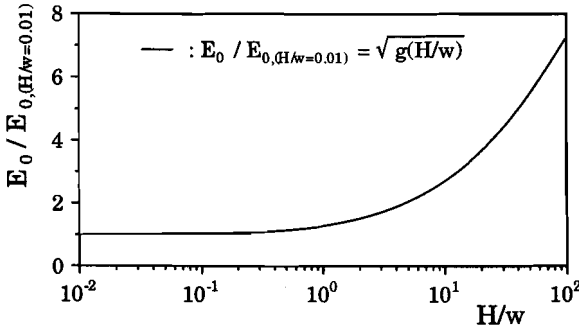
*Figure 4.8: Improvement of the voltage allowed across the sensor due to a decreasing sensor width w (larger H/w ratio). The improvement is related to a sensor with a large sensor width (H/w=0.01).*

where $C = \sqrt{(\xi_3 \chi_0 l^2 k_{sub} \Delta T_{diss})/hH}$. This relation is represented in figure 4.8 which shows the improvement related to the situation for a very wide thin film ($H/w=0.01$). The increase of sensor output is linearly dependent on $\sqrt{g(H/w)}$. Without the width adjustment of the sensor the specific heat flux due to dissipation would be too high. According to figure 4.8 it can be seen that for a $H/w$ ratio equal to 100 the voltage allowed is more than 4 times as high as that of a sensor with half the width of substrate (which is frequently used).

### 4.2.4 Design strategy

The design strategy can be summarized in the following steps (see also table 4.1):

1. Compute the thermal mass of the substrate required to prevent an unsuitably unsteady surface temperature change due to convective heat transfer.

2. Calculate the maximum voltage allowed across the sensor, such that the change in dissipation flux is kept within tolerable limits.

3. Compute the required sensor width so that the large dissipation flux obtained from the previous point does not cause too much sensor heating.

Figure 4.9 shows the heat flux level for two experiments with comparable flow conditions. The left-hand figure represents the measurement with thin film gauges used in test section TS3 designed according to the conventional guidelines. The right-hand figure displays the heat flux measured with an improved technique (less noise) in test section TS4, as will be elucidated in the next section. The final increase in the accuracy by the signal-to-noise ratio is about a factor of 5.

| | phenomenon | describing equation | comments |
|---|---|---|---|
| step 1. | unsteady surface heating | eq.4.13 | minimize: $\sqrt{(\rho c k)_{sub}}$ |
| step 2. | ohmic heat flux change | eq.4.16 | maximize: $E_0, l, \sqrt{\alpha_0 \chi_0}$ minimize: $h$ |
| step 3. | heating due to ohmic heat flux | eq.4.20 | maximize: $H/w$ minimize: $H$ |

*Table 4.1: Table of guidelines to design cold thin film gauges.*
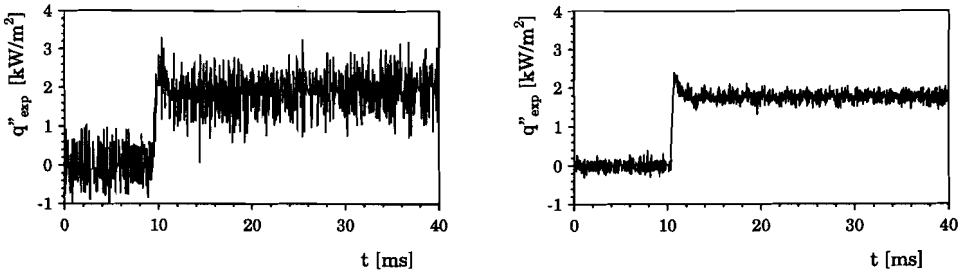


*Figure 4.9: The left-hand figure shows the laminar heat flux level for a conventional thin film gauge ($Re_u = 2.9 \times 10^6$ $[m^{-1}]$, $M=0.33$, $x=3.1\times10^{-2}$ $[m]$, $E_{bridge}=3.0$ $[V]$). In the right-hand figure the result with improved technique is shown for approximately equal flow conditions ($Re_u = 2.4 \times 10^6$ $[m^{-1}]$, $M=0.36$, $x=2.7\times10^{-2}$ $[m]$, $E_g=30.00$ $[V]$).*

## 4.3 Design of thin film sensors

The thin film sensor is produced in different steps. First, a homogeneous metal film with desired thickness is evaporated onto the whole substrate surface. Next a photoresist layer is sprayed onto the surface. The part of the metal film that must be removed is exposed to UV-light (the sensor lay-out is covered by a mask). Due to the light the cross-links in the photoresist are broken down and the solubility of the positive photoresist improves by a factor of 100. This part can easily be removed by means of etching. Finally, the protecting photoresist on the sensor lay-out is removed with ethanol.

In this work several metals (Ti, Ni and Pt) were examined. It was found that Titanium performs the best because this metal is very suitable for etching. Due to its insensitivity to etching underneath (i.e. etching below the film surface causing brittle mushroom-like structures), thin film sensors to a width of 10 $\mu m$ can be produced without problems. Very sharp edges are obtained. An additional advantage is the relatively high value for the product $\alpha.\chi$, which is advantageous
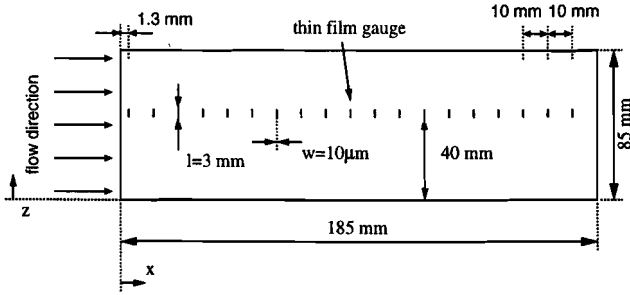
*Figure 4.10: Top view of the glass substrate with the positions of the thin film gauges (applied in test section TS3).*

in the optimization (paragraph 4.2.2).

As discussed earlier, two test sections (TS3 and TS4) were used to measure heat flux with different objectives. Beside the aim to study the adequacy of the Ludwieg tube in boundary layer transition research, the experiments with the third test section were performed to gain experience with heat transfer measurements.

**First sensor plate (TS3)**

For this experiment 19 gauges were used aligned along one line in the flow direction (figure 4.10) and equidistantly spaced on a flat glass plate. A plate length of 185 $mm$ was chosen to meet the requirement that sufficient spatial accuracy is obtained in the transitional part. This is linked to the number of gauges. The number was 19, which is a compromise between the presence of sufficient gauges in the transition region and the required space to have a track resistance much smaller than the sensor resistance. Tracks connect the sensor to the wire at the tube wall, which have the same layer thickness as the sensor. The track resistance must be negligible so that variations of the sensor are dominant.

To have sensors smaller than the occurring spots ($> 5$ $mm$) the sensor length was chosen to be 3 $mm$. In this way spot passages are clearly visible. Computations (using equation 4.2) show that in order to have a ratio $R_{track}/R_{sensor}$ smaller than 2%, the gauges should have a width of 10 $\mu m$. The electrical gauge resistances are a few kilo ohms (with sensor thickness $h$, of 70 $nm$).

Silver paint was used to connect electrical wires and tracks (figure 4.11). Due to their roughness these contacts influence the flow by generating turbulence. To avoid this effect from being measured by the last sensor, the first tracks are led under an angle in the downstream direction. The geometry was chosen such that turbulent spots generated at the contacts remain outside the sensor region along the whole plate (see figure 4.11). Each sensor was connected to a Wheatstone
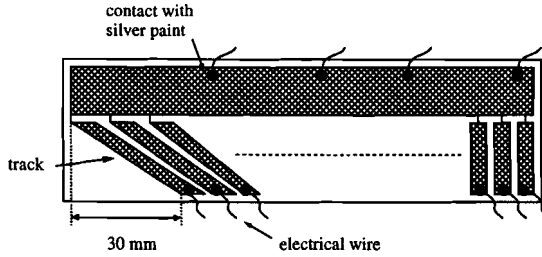
*Figure 4.11: Top view of the sensor shown in the previous figure now with tracks, electrical wires and silver paint contacts.*

bridge with the maximum voltage across the gauge of 3.0 $V$ (according to *Diller* [1993]). The bridge output was amplified 500.0 times by means of a self-made two-step operational LF356 amplifier (cut-off frequency of about 80 kHz [*Oever*, 1995]). A high and low pass filter removed frequencies below 1 $Hz$ and above 30 $kHz$.

**Second sensor plate (TS4)**

For test section TS4 a new sensor configuration was designed. Two requirements played a part in the determination of the configuration for this sensor plate.

First, the intermittency (see chapter 2) must be measured equidistantly over the whole plate. This implies that the sensors either must be much smaller than the turbulent spots (in order to measure or a fully turbulent level or completely laminar, and not a mixture) or the intermittency must be determined from the integral heat flux according to *Dhawan and Narasimha* [1958], with the Stanton number instead of shear friction coefficient. Since the number of passing spots is finite, the latter method is more accurate when the sensor is longer. In this case the flow is checked over a larger width, and more spots are taken into account, which provides a better representation of the average situation.

Second, individual spot parameters, like leading and trailing edge velocities, and lateral growth must be determined. In order to determine these parameters the spot position must be known. Therefore, detector gauges are used (figure 4.12) as well as gauges that measure the spot features.

Suppose that the outputs of gauges 5a,b,c,d, 6, 7, 8a,b,c,d, 9 and 10 are measured. If the turbulent spot density is not too large, the spots are clearly spatially separated. Sensors 5b and 5c indicate a spot while 5a and 5d do not. In this case the position of this particular spot is known. Sensors 6 and 7 will cover the whole spot (just like sensors 9 and 10) [2]. Spot arrival and departure can

---

[2]Lateral spot growth (about 11°) is less than 10 $mm$ after 5 sensors (50 $mm$), which means that sensor 10 still covers the whole spot width.
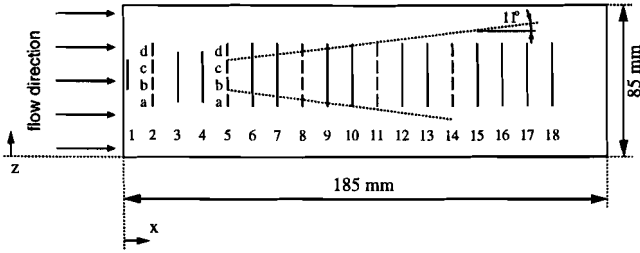
*Figure 4.12: Top view of the thin film lay-out applied in test section TS4. The short sensors can additionally be used as detector gauges.*

be detected with the knowledge that the whole spot is measured, which leads to the determination of stream-wise spot growth rates ($C_{le}$, $C_{te}$). The lateral spot growth can be derived from the value of the measured heat flux signal (in this case some assumptions are required). It should be noted that in this study the individual spot parameters were not studied with this sensor plate. In the near future this option will be employed.

Since turbulent spots are not that large at the very beginning, the sensors are chosen somewhat shorter near the leading edge of the plate to prevent unnecessarily vulnerable sensors (due to their length). The sensor length is restricted to a maximum of 40 $mm$ because of the conceivable influence of turbulent boundary layers at the tube wall and disturbances generated at contact points with silver paint as discussed before. To have a more accurate determination of intermittency (as discussed earlier) and to obtain a higher sensor output, the length of detector gauges was equal to the maximum value of 9.5 $mm$. According to the design method, the width of the 9.5 $mm$ gauges was computed to be 10 $\mu m$. The maximum voltage across the gauge was 16.00 $V$, whereas the gauge resistance was about 10 $k\Omega$. The width of the 40 $mm$ long sensors was designed to be 50 $\mu m$. The voltage across these gauges was 30.00 $V$. In order to 'impose' the homogeneous Dirichlet boundary condition at the bottom, thermally conductive paste was used which transports the heat produced by the gauge to the steel plate (figure 4.13). The final sensor configuration including the connecting tracks is given in figure 4.14. Several clusters of gauges can be recognized connected on one side to a collective electrical ground (e.g. sensors 3,4,5a,5b,5c and 5d have one common ground). This was done to reduce the number of tracks required. The other sensor side is the 'signal' side. For this sensor a constant current circuit was built consisting of 33 separate constant current sources using BF256C N-channel silicon field-effect transistors (cut-off frequency is $1GHz$). The sensor output was amplified 100.0 times with an operational LF356 amplifier.
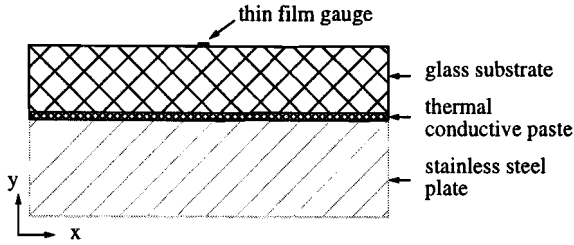
Figure 4.13: Cross-section in the x,y-plane of the thin film substrate steel plate construction. Thermally conductive paste takes care of the transport of heat (due to dissipation) to the steel plate.
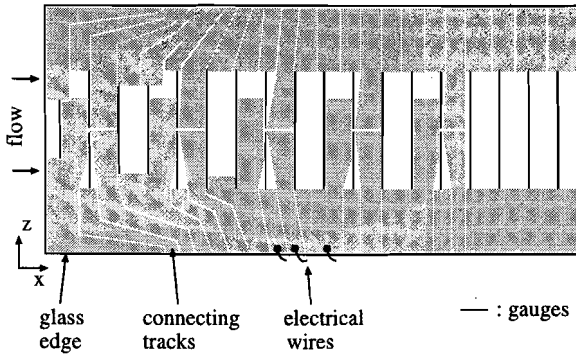


Figure 4.14: Top view of sensor lay-out including the connecting tracks. The electrical wires are connected with silver paint as explained before (sensor width w, is not drawn to scale).

## 4.4    Influence of noise and noise reduction

Many different sources determine the interference of the final noise level with the desired signal. Three main categories can be distinguished: erratic, man-made and circuit noise [*Vergers*, 1987]. Erratic disturbances contain natural electrical disturbances (like lightning discharges) and astronomic effects. Man-made noise is generated by ignition mechanisms and machines. While circuit noise is created by resistors and transistors for example.

In particular the 50 $Hz$ frequency of the electricity grid shows up very often. To reduce the effect on the resulting noise level, different measures must be taken. All signals must be shielded to protect the sensor signal from noise from the surroundings. Possible noise sources from the surroundings are checked individually regarding their effect. The Ludwieg tube is grounded. Ground loops must be avoided. The influence of the connections between wires and thin film is checked (No differences were noticed between silver paint contacts and soldered contacts).

A significant improvement is obtained by the application of a differential amplifier. The signal is amplified normally while the noise level on the original signal is not boosted proportionally. *Vergers* [1987] suggests that noise from the same noise source is eliminated because the noise on the two input branches is equal and therefore not noticed after amplification. The advice for future work is to incorporate this positive aspect in the design of a sensor.

Figure 4.15 shows the final noise level, expressed in a temperature equivalence, having a rms-value of about $4.1 \times 10^{-4}$ $[K]$. This results in a noise rms
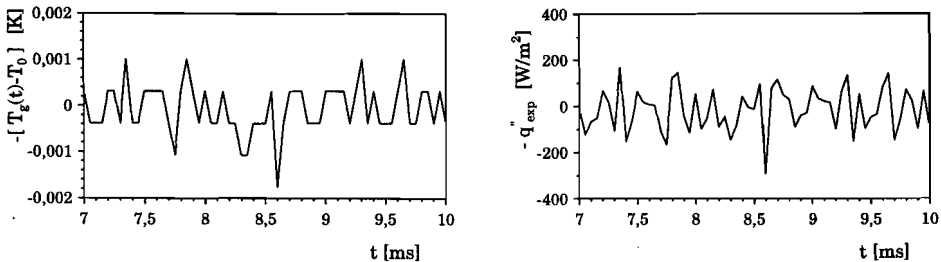


*Figure 4.15: Left-hand figure shows the noise level on the measured thin film temperature just before the incident expansion wave arrives (detail of figure 4.4). In the right-hand figure the noise on the reconstructed heat flux is plotted. ($Re_u = 4.9 \times 10^6$ $[m^{-1}]$, $M = 0.36$, $x_{gauge} = 53$ mm, $E_g = 40.0$ $[V]$ over a 40 mm long gauge).*

level of 73 $[W/m^2]$ on the flux. Changes above the noise level can be recognized. The effect of noise (according to equation 4.23) on the averaged heat flux leads to a final inaccuracy of 0.2% to 1.8% for the whole range of conditions.
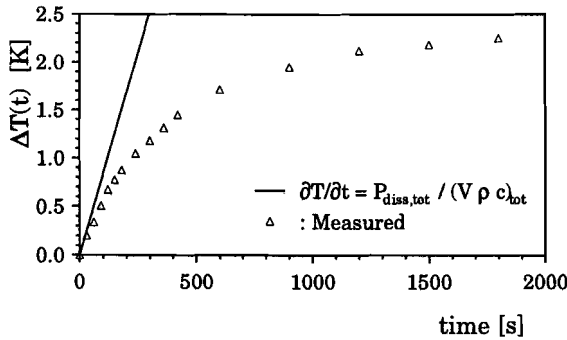
*Figure 4.16: Temperature drift of the flat plate as a result of the unsteady heat storage due to the power supplied by thin film gauges (sensor plate 2, short gauges 16.00 V, long gauges 30.00 V).*

## 4.5   Accuracy of heat flux measurements

The accuracy of the cold thin film gauge is determined by several effects. It will be shown that the quality can be improved using an in-situ calibration.

As a result of the present flat plate configuration a typical additional effect shows up. Because a thin plate construction is used (1 *mm* glass with 1.5 *mm* steel), the plate is a little heated due to steady internal dissipation in the gauges. This heat must be transported to the side walls (with a poorer thermal contact) or must be released to the surrounding air, which makes a thermal potential necessary too. Figure 4.16 shows the measured temperature increase in time. Initially, the heat losses are negligible and the temperature rise is balanced by the total power supplied by thin film gauges $P_{diss,tot}$, and thermal mass of the flat plate, given by

$$P_{diss,tot} = [(V\rho c)_{glass} + (V\rho c)_{steel}] \frac{\partial T}{\partial t} \tag{4.22}$$

Here, $V$ is the volume of glass and steel plate and $\partial T/\partial t$ is the initial instationary heating. Estimations according to equation 4.22 confirm the initial temperature rise measured, which is about $8 \times 10^{-3}$ $K/s$ (for voltages given in caption of figure 4.16). Finally, the temperature increase stabilizes at 2.3 $K$. This implies that the heat transfer rate during experiment is somewhat larger due to this effect. To improve the final accuracy this effect must be taken into account.

From figure 4.22 it can be concluded that (if the measured experimental heat flux is corrected for this effect) at least 15 minutes are required between succeeding experiments to have a sufficiently stabilized plate temperature. Fortunately, this corresponds to the time required to perform a new experiment in the Ludwieg tube. It is remarked that the unsteady heating of the whole plate was not discussed in the design rules. There, the plate temperature was considered to be

constant and the relevant time constant was related to the time for the sensor to attain its final equilibrium temperature ($\approx 100$ $ms$). However, it turns out that the whole plate is heated with a time constant of about 15 minutes.

Beside the effect of plate heating there are other effects that limit accuracy. The error in voltage adjustment across the sensor is less than 0.1%. The amplification factor is also regulated within 0.1%. The temperature coefficient of resistivity $\alpha$, is quite inaccurately known with a variation between the different gauges of $\pm5\%$. According to the manufacturer, the glass substrate properties are specified within $\pm1\%$ for bulk material. However, the properties at the surface may deviate. The connecting strips of the glass substrate have a relative resistance (related to sensor resistance) of less than 1.7%. The error in numerical reconstruction is less than 0.5%. Some inaccuracy has to be permitted in the design of the gauges according to the parameters $\xi_i$. For the first two design considerations (unsteady surface heating due to experimental heat flux and variation of dissipation flux in sensor), this effect depends on the experimental flux rate $q_{exp}^{"}$. This flux in its turn depends on the experimental conditions, location and dimension of gauges. The parameter $\xi_1$ is designed to vary between 0.5% and 1.1%, while $\xi_2$ varies between 0.4% and 3.2% for experiments over the whole range of conditions. The ohmic sensor heating has been set to 3.6 $K$ ($E_g$=16.0 $V$) for the short sensor, and 1.9 $K$ ($E_g$=30.0 $V$) for the long sensor. This is rather high, but because this effect is constant in contrast to the former ones, the effect is eliminated in the calibration which is discussed below.

The correspondence between measured heat flux and theoretically expected heat flux has been tested and is shown in figure 4.17. By generating a low unit-Reynolds number at a low free stream turbulence level, a completely laminar boundary layer is obtained on the flat plate with thin film gauges in the Ludwieg tube (no turbulent spots are observed in the heat flux).

The averaged measured heat flux in terms of the Stanton number is given by

$$\overline{St_{exp}(x)} = \frac{1}{t_2 - t_1} \int_{t_1}^{t_2} \frac{q^{"}(x,t)}{(T_w - T_r)kRe_uPr} dt \qquad (4.23)$$

where $t_1$ and $t_2$ are the beginning and end of the test period respectively, $q^{"}(x,t)$ is the measured heat flux, and $k$ is the thermal conductivity of the gas. All properties are evaluated at static gas temperature in the tube $T_t$. For a constant free stream velocity flow along a semi-infinite plate with constant surface temperature, the heat transfer rate in terms of the Stanton number for a laminar boundary layer is given by [Kays and Crawford, 1980]

$$St_l(x) = 0.332Pr^{-2/3}Re_x^{-1/2} \qquad (4.24)$$

The heat flux according this relation is given by the solid line. The measured heat flux (averaged according to equation 4.23) are indicated with the symbols. The temperature difference has been corrected for plate heating with the extra
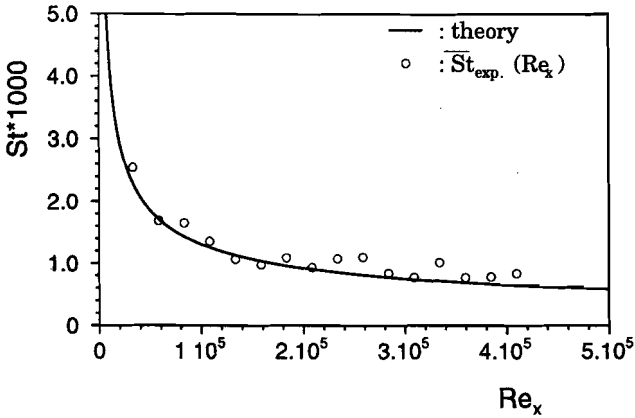
*Figure 4.17: Uncorrected data compared with the theoretical heat transfer rate.*
$Re_u = 2.51.10^6 \ m^{-1}$, $M = 0.36$, $T_{gas} - T_{recovery} = 32.5K$, $Tu = 1.5\%$ *in air.*

temperature difference shown in figure 4.16. This result indicates that the heat
flux values measured are distributed around the theoretically expected heat flux.
Generally, the measured fluxes are higher. The scatter can be explained by the
sources of inaccuracy as discussed before. Sources of uncertainty are found in the
temperature coefficient of resistivity $\alpha$, (equation 4.5), substrate material (equa-
tion 4.12), temperature drift of the plate (figure 4.16), voltage across the sensor
(equation 4.5), and amplification factor (included in equation 4.5). Since many
sources of uncertainties are linearly related to the heat flux, the output of each
heat flux signal on position $x$ can be improved by eliminating these uncertainties
with an individual multiplicative calibration factor by comparison of the experi-
mental and theoretical (relation 4.24) heat flux. The individual calibration factor
obtained with this in-situ calibration is only valid to the Mach number (see also
appendix C) and sensor voltage at which the calibration is performed.

Figure 4.18 shows the averaged heat flux levels (dimensional to distinct the
several levels) for different unit-Reynolds numbers in comparison to the theo-
retically expected flux. A maximum deviation of 3.9% at $x=0.067 \ m$ is found
for the experiment with unit-Reynolds number equal to $3.6 \times 10^6 \ [m^{-1}]$, which
is supposedly due to the start of transition. This indicates that the calibration
performed provides the theoretical heat flux levels for all unit-Reynolds numbers.

The reproduction accuracy for equal flow conditions were tested for two suc-
ceeding experiments. Figure 4.19 shows two experiments for $M=0.18$, $Re_u=1.60\times$
$10^6 \ [m^{-1}]$. In this experiment the reproduction accuracy ranged from 0.06% at
the leading edge to 1.5% at the end. The reproduction also was tested for an
intermediate period of 8 weeks. This verification proved that the maximum de-
viation is 0.9%, and that 50 percent of the gauges is still within the range of
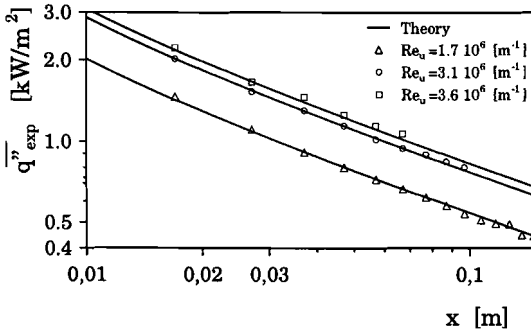
*Figure 4.18: Averaged heat flux level over the flat plate for different unit-Reynolds numbers with equal calibration factor. (Test section TS4, M=0.18). The solid lines represent the theoretical heat flux.*
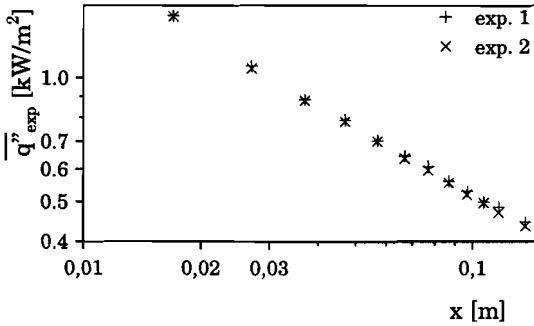


*Figure 4.19: Average heat flux level for two succeeding experiments.*

accuracy obtained between two succeeding experiments in one day (presented in figure 4.19). This indicates that the effect of film aging is negligible on this time interval. *Epstein and Guenette* [1986] found the calibration uncertainties in their experiments to be less than 1% over several months of use.

# Chapter 5

# Boundary layer transition results

## 5.1 Introduction

In this chapter results on heat transfer measurements in transitional boundary layers are presented. First, the individual spot properties were studied like self-similarity of the heat flux, propagation velocities, and spot growth. The overall behaviour in the transitional boundary layer was studied using the time-averaged intermittency. The method to compute the intermittency is discussed, just like the determination of the transition onset and spot formation rate. Using this method, the influences of the Mach number and free stream turbulence on the onset of transition, the individual spot behaviour and spot formation rate were studied.

In the processing of the experimental data several relations as found in the literature are used. Therefore, these relations will be described here briefly. For a constant free stream velocity flow along a semi-infinite plate with constant surface temperature, the heat transfer rate in terms of the Stanton number for a laminar boundary layer is given by equation 4.24. The heat transfer level of a turbulent boundary layer is influenced by several parameters. For a turbulent boundary layer with a constant surface temperature, the heat transfer is given by [*Kays and Crawford*, 1980]:

$$St_{turb,x-x_0} = 0.0287 Pr_{turb}^{-0.4} Re_{x-x_0}^{-0.2} \tag{5.1}$$

This relation holds for $0.5 < Pr < 1.0$ and $5 \times 10^5 < Re_x < 5 \times 10^6$. There is some uncertainty about the choice of the initial value of $x=0$. Here we will take $x=0$ as the position where transition starts. In practice it hardly affects the final results whether we choose $x=0$ as the plate leading edge or as the transition onset of the flow. *Davies and Bernstein* [1969] found the turbulent Prandtl number for air to be equal to unity 'which has been argued as a reasonable value on the

grounds that energy and momentum transfer both take place largely as a result
of turbulent mixing'. This was confirmed by measurements of *Rohsenow and Choi*
[1961] and *Volino and Simon* [1991]. However, in the literature differences up to
20% in the turbulent heat transfer levels can be found. Relation 5.1 was probably
found from wind tunnel experiments at room temperature and low turbulence
values. With regard to equation 5.1, the influences of wall-temperature effects
and compressibility on fluid properties in the boundary layer can be taken into
account for a correction. For a heated turbulent boundary layer flow both effects
are incorporated in the following relation:

$$\left(\frac{St}{St_{CP}}\right)_{turb} = \left(\frac{T_w}{T_r}\right)^{-0.4} \left(\frac{T_r}{T_t}\right)^{-0.6} \tag{5.2}$$

where the index $CP$ refers to constant property situation, $T_w$ is the wall tem-
perature, $T_r$ is the recovery temperature ($T_r = T_t(1 + \sqrt{Pr}\frac{\gamma-1}{2}M_t^2)$), and $T_t$ is
the static temperature of the gas flow in the tube (see section 3.3.1). Equation
5.2 yields a correction of $St/St_{CP} = 0.95$ for $M_t$=0.36. Finally, the turbulent
heat transfer rate is affected by the free stream turbulence level [*Simonich and
Bradshaw*, 1978] according to

$$\frac{St}{St_{Tu=0}} = 1.0 + 0.05Tu \tag{5.3}$$

where $Tu$ is the free stream turbulence level in per cents. According to *Simonich
and Bradshaw* [1978] the coefficient 0.05 has an uncertainty of ±20% due to a
wide scatter in the experimental data.

## 5.2   Individual turbulent spot properties

In chapter 2 the self-similar shape of an individual turbulent spot was discussed.
In this section it will be shown that the self-similarity holds for the internal heat
transfer too. To measure the internal heat transfer, the sensors must be smaller
than the spot size. For this reason, the results of test section TS3 are used,
having sensors of 3 *mm* length. The characteristic spot size is over 10 *mm*. The
spot formation rate is low in this experiment due to a low free stream turbulence
level. This gives us the opportunity to study the properties of individual turbulent
spots.

The heat transfer during a passing turbulent spot is shown in figure 5.1.
Several stages can be recognized during a spot passage [*Hogendoorn et al.*, 1996].
Upon the arrival of the spots leading edge, the heat transfer increases strongly
from the laminar level to the level of a fully turbulent boundary layer. The high
flux level is maintained up to the end of the spot (the arrival of the trailing edge).
The region behind the turbulent spot, in which the heat flux level returns to the
laminar rate, is called the calmed region (see section 2.3). When the spot has
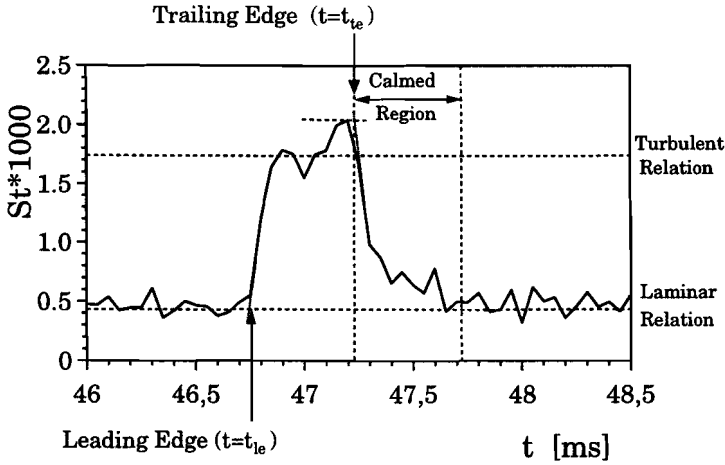
*Figure 5.1: Surface heat flux in terms of the Stanton number, during the pass-ing of a turbulent spot. The leading edge, trailing edge and calmed region are indicated. (M=0.33, $Re_u = 1.1 \times 10^7$ $m^{-1}$, x=81 mm, test section TS3).*

passed, the boundary layer is laminar again.

To investigate the self-similarity, the turbulent spot must be scaled. The heat flux $St(x,t)$, has been scaled with the laminar and turbulent heat flux levels (see equations 4.24, 5.1, 5.2, and 5.3) to an instantaneous intermittency $\gamma^*(x,t)$:

$$\gamma^*(x,t) = \frac{St(x,t) - St_l(x)}{St_{turb}(x) - St_l(x)} \tag{5.4}$$

Several different scaling techniques are available for time scaling [*van Hest,* 1996]. In this work the scaling with respect to the times of the arrival of the leading edge $(t = t_{le})$ and the departure of the trailing edge $(t = t_{te})$ has been used, which leads to:

$$\tau = \frac{t - t_{le}}{t_{te} - t_{le}} \tag{5.5}$$

Since the sample frequency was limited to 20 $kHz$, the time between two samples is 0.05 $ms$. This sample time is as large as 10% of the spots' passing time (about 0.5 $ms$). In order to increase the accuracy to determine the time of spot arrival and departure, the following procedure was used. To determine $t_{le}$, the intersection was taken of the level predicted by the extrapolated rising slope and the theoretical laminar relation (see figure 5.1). An equivalent method was used for the trailing edge. Here, the intersection of the horizontal line at the maximum level with the extrapolated falling slope was taken. Figure 5.2 shows the same spot at different locations along the flat plate, scaled according to equations 5.4 and
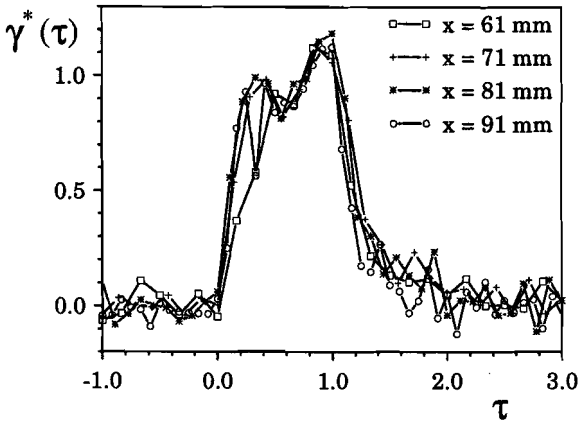
Figure 5.2: Self-similarity of the spot's heat flux during propagation at several stream-wise locations ($x_{start}$ is 11 mm from leading edge, $Re_u = 1.1 \times 10^7 \ m^{-1}$, $M = 0.33$.
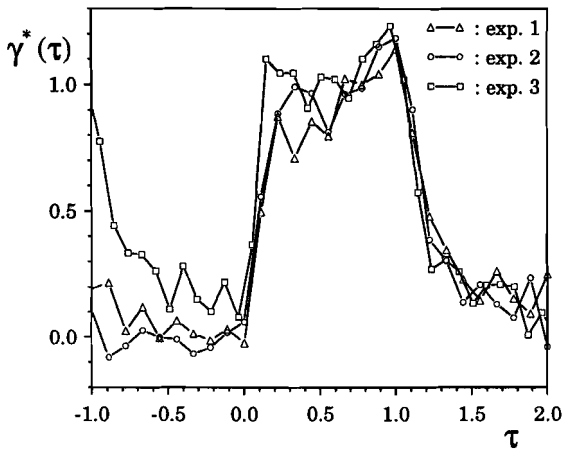


Figure 5.3: self-similarity for different experiments, $M = 0.33$.

5.5. Several conclusions can be drawn from this figure. The turbulent spot shows a surprisingly good self-similarity. This holds for the rising flank, immediately after the leading edge, as well as in the calmed region. Inside the spot, a general trend can be observed that exceeds the random behaviour of the noise level. Directly behind the leading edge, the heat transfer weakly decreases, whereas it increases to a maximum value at the trailing edge. The level inside the spot corresponds very well with the empirical relation for a fully turbulent boundary layer (starting at the leading edge of the plate). This trend is recognized for all stream-wise locations. The shape resembles very well the velocity increase inside the turbulent spot close to the wall measured by *Cantwell et al.* [1978]. The form of the spot at the first location ($x$=61 $mm$, indicated with the squares), directly after $\tau = 0$, deviates somewhat from the shape at the locations that follow. This may be attributed to the initial development of the spot. Another explanation is that for small spots the measurements are influenced by the position of the sensor in relation to the spot. In figure 5.3 three spots from different experiments are plotted. This figure shows that the characteristics described before hold for different spots as well, even for a spot travelling directly behind another spot (experiment 3). The latter experiment shows a non-zero intermittency in front of the spot, indicating the calmed region of a previous spot.

An important aspect that can be observed from figures 5.2 and 5.3 is that the heat transfer rate in the calmed region ($1.0 < \tau < 2.4$) significantly contributes to the total heat transfer due to a turbulent spot. The area of the calmed region compared to the area of the spot ($0.0 < \tau < 1.0$) is about 35%. This implies that 26% of the total flux, due to the passage of a turbulent spot, is caused by the calmed region.

The spot growth in the stream-wise direction is constant. A typical example is presented in figure 5.4. On the horizontal axis the modified stream-wise distance is given, which is equal to the actual distance minus the position of the virtual spot origin. This location is determined by the intersection of the fit through the leading edge and trailing edge data points. The vertical axis represents the time starting from the virtual spot's birth. A constant propagation velocity is recorded for the leading edge as well as for the trailing edge. It is worthwhile noting that the leading edge velocity is constant shortly after its birth. Already within 0.2 $ms$ (and probably earlier) a constant leading edge velocity is attained. Another aspect that can be observed from figure 5.4 is the rapid spot growth. After about 1 $ms$ the spot already has a length of more than 40 $mm$.

From the propagation velocity of both the leading and trailing edges, the averaged fractions with free stream velocity $u_t$ can be determined. For the leading edge this yields $C_{le} = u_{le}/u_t = 0.98 \pm 0.10$. For the trailing edge this fraction is $C_{te} = u_{te}/u_t = 0.54 \pm 0.04$. The uncertainties of $\pm 0.10$ and $\pm 0.04$ are due to the uncertainty in determination of propagation velocities, and uncertainty in flow conditions. In comparison to other experimental data the trailing edge propagation parameter is within the same range (see figure 5.5). The leading edge
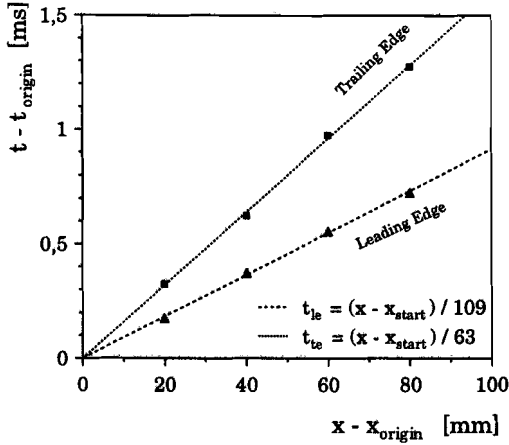
*Figure 5.4: Propagation of an individual turbulent spot over flat plate (test section TS3). $t_{origin}$ and $x_{origin}$ are the virtual start time and location, respectively ($x_{origin}$ is 11 mm from leading edge, $Re_u = 8.4 \times 10^6$ $m^{-1}$, M=0.33).*

propagation is somewhat higher than that found by *Clark et al.* [1994]. However, if the experimental data presented in figure 2.12 are studied, the present value falls within the scatter of experimental data. Finally, it seems that the propagation velocities are not influenced by mutual spot interaction.

## 5.3    Determination of time-averaged intermittency

For the analysis of experimental data in the transitional region, the time-averaged intermittency is very useful. In literature several techniques are employed to determine the intermittency as well as possible, each with their own specific problems. The determination of the intermittency in this work is affected by the choice of relatively long sensors. A typical example of the heat flux at several locations in a transitional boundary layer is shown in figure 5.6. These signals are obtained with the 9.5 *mm*-long sensors. It can clearly be observed that the time occupied by turbulent spots increases the more downstream they are. Since the turbulent spots do not all cover the complete sensor, the maximum values are very different. This can be seen in the top part of the figure. Moreover, it is hardly possible to recognize individual spots (i.e. middle part of the figure). When this effect is already found with 9.5 *mm* gauges, the effect on the 40 *mm* gauges is much stronger. For this reason it is difficult to apply detection functions to determine the averaged intermittency. The averaged heat flux was applied in accordance with *Dhawan and Narasimha* [1958]. Here, the Stanton number was used instead of the shear friction coefficient. The time-averaged intermittency
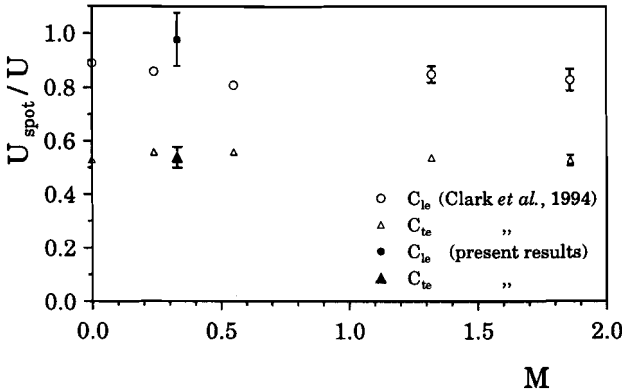
*Figure 5.5: The measured propagation velocities in comparison to the data of Clark et al. [1994].*

then is calculated with:

$$\gamma(x) = \frac{\overline{St_{exp}}(x) - St_l(x)}{St_{turb}(x) - St_l(x)} \tag{5.6}$$

which is equal to the time-averaged form of equation 5.4, where $\overline{St_{exp}}(x)$ is the averaged Stanton number measured (given by equation 4.23). The intermittency is calculated at each gauge location. An example is shown in figure 5.7. In this figure the measured time-averaged values of heat flux along the plate are presented as a function of Reynolds number. The inverse square root dependence of the Stanton number at the very beginning clearly indicates the laminar start. The heat fluxes recorded by the first gauges correspond to the theoretical laminar level. In the end, the boundary layer is fully turbulent.

The accuracy of intermittency reproduction was verified with two experiments under the same conditions (figure 5.8). Despite the limited number of turbulent spots during one experiment, the intermittency could easily be reproduced. The transition onset as well as the transition length are very similar. The maximum deviation is ± 2%. This experiment clearly confirms that the test time (about 50 $ms$) is sufficiently long to perform reliable experiments on transitional boundary layers.

**Influence of plate angle**

We investigated whether the transition process depends on the angle of the plate. While the flow conditions are kept equal, the plate angle is varied. This was done for a flow with a free stream turbulence intensity of 2.2 %. Figure 5.9 shows the intermittency for angles between $0.9^o$ and $2.3^o$. No significant differences are observed in the angle-range from $1.1^o$ to $2.3^o$. Since the boundary layer transition process is strongly dependent on pressure gradients, it may be
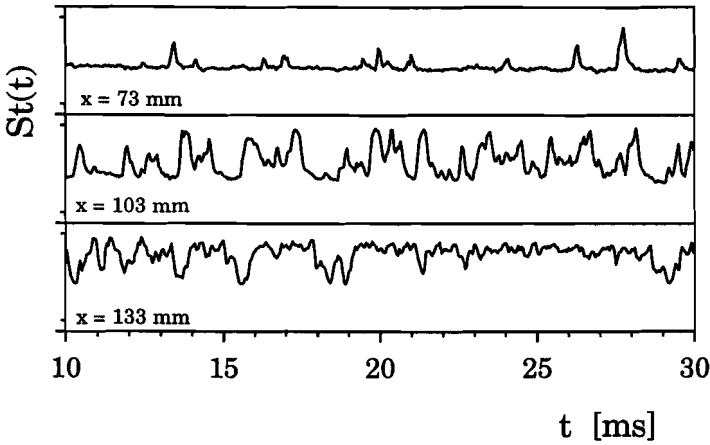
*Figure 5.6: Heat transfer at several locations in the transitional boundary layer ($M=0.36$, $Re_u = 4.9 \times 10^6$ $m^{-1}$, $Tu=1.7\%$, test section TS4, 9.5 mm-gauges).*
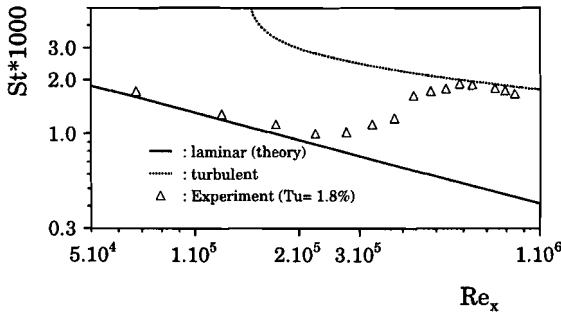


*Figure 5.7: Determination of the intermittency distribution in a transitional boundary layer. This figure shows the time-averaged experimental heat transfer together with the laminar and turbulent heat transfer relations from the literature ($M=0.36$, $Re_u = 5.25 \times 10^6$ $[m^{-1}]$, $Tu=1.8\%$).*
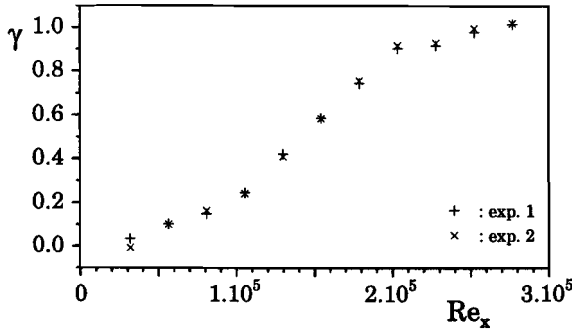
Figure 5.8: Reproduction of the intermittency distribution (M=0.36, $Re_u$ = 2.45 × 10⁶ m⁻¹, Tu=2.2%, grid no. 3).

*Figure 5.8: Reproduction of the intermittency distribution (M=0.36, $Re_u$ = $2.45 \times 10^6$ $m^{-1}$, Tu=2.2%, grid no. 3).*
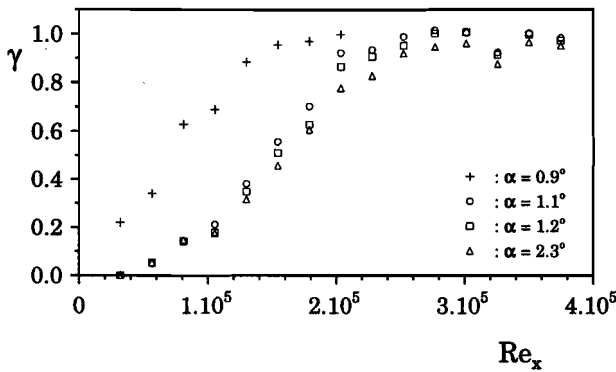
*Figure 5.9: Effect of plate angle α on intermittency (M=0.36, $Re_u$ = 2.45 × 10⁶ [$m^{-1}$], Tu=2.2%).*

concluded that there is no pressure gradient induced in the experiments within this range of angles. It is striking to see that the intermittency is essentially different for the angle of 0.9°. For this 'critical' angle a faster transition is observed. The extrapolated intermittency is larger than zero even at the leading edge of the plate. An experiment with test section TS3 shows in more detail that the turbulent spots seem to be periodically generated in front of the leading edge of the plate (see figure 5.10) in situations with the plate at a critical angle. In this case a spot with a considerable size is generated with a virtual origin in front of the plate. This poorly documented effect can be explained physically as follows. Due to the turbulent fluctuations the free stream 'velocity vector' will vary. The angle of this fluctuation is approximately equal to the arctangent of the free stream turbulence level (arctan 0.022 ≈ 1.3°). Turbulent fluctuations producing an angle of incidence larger than the plate angle are liable to cause boundary layer separation at the *sharp* leading edge of the plate (see figure 5.11). This leads to a fast break-down resulting in a turbulent spot. After its origina-
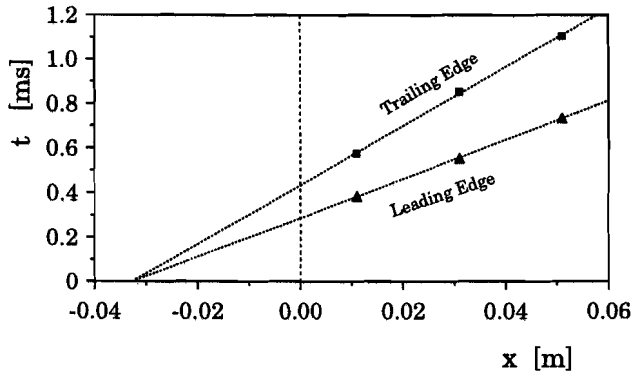
*Figure 5.10: Turbulent spot with virtual origin in front of the flat plate (M=0.33, $Re_u = 2.6 \times 10^6 \ [m^{-1}]$, test section TS3).*
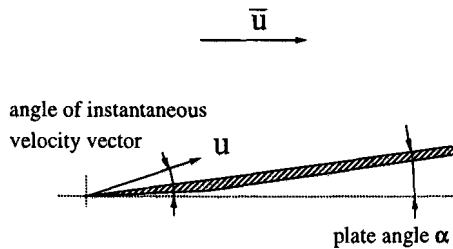


*Figure 5.11: A sketch of a plate angle which is smaller than the angle of an instantaneous velocity vector due to a turbulent fluctuation.*

tion, this spot is found to behave like a normal spot. For future experiments at higher free stream turbulence levels, the sharp leading edge should be replaced by an elliptically-shaped plate nose. With the latter geometry a proper boundary layer initiation at higher free stream turbulence levels may be possible. For a sharp leading edge, the tangent of the plate angle must be of the order of the turbulence intensity to have a proper laminar boundary layer downstream of the leading edge. The current construction allows a maximum angle of about $2.4^o$, which corresponds to a maximum free stream turbulence of about 4%.

In the present work the experiments were performed for plate inclinations above the critical angles. The free stream turbulence intensity was varied in the range of 1.2% to 4.0% (see sections 3.4 and 3.5).

## 5.4 Effect of free stream turbulence and Mach number on boundary layer transition onset

In chapter 2 a convenient intermittency model was discussed. This model was
given by equation 2.1:

$$\gamma = 1 - \exp[-\hat{n}\sigma(Re_x - Re_{tr})^2] \text{ for } Re_x > Re_{tr}$$

An important parameter in this model is the transition Reynolds number $Re_{tr}$.
This number was determined from the experimental data by a least-squares fit
through the intermittency distribution. Therefore, the experimental data were
transformed with the function [*Gostelow and Blunden*, 1989]

$$F(\gamma) = \sqrt{-\ln(1 - \gamma)} \tag{5.7}$$

The fit of the function $F(\gamma) = A + BRe_x$ through the transformed data for $F(\gamma)$
between 0.1 and 2.15 ($0.01 < \gamma < 0.99$) yields both the transition Reynolds num-
ber ($Re_{tr} = -A/B$) and the spot production rate ($\hat{n}\sigma = B^2$). A typical example
of a least-squares fit is shown in figure 5.12. The distribution of the transformed
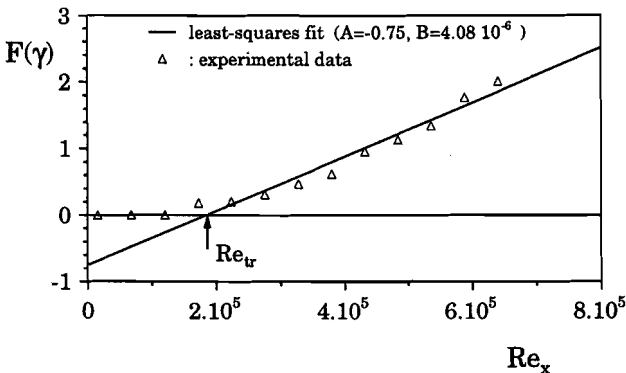


Figure 5.12: Least-squares fit through the transformed experimental intermittency
(M=0.36, $Re_u = 5.25 \times 10^6$ [$m^{-1}$], Tu=1.8%).

experimental data is somewhat concave, indicating that the intermittency model
is not fully matched. This was also observed in other experimental data, obtained
with hotwire measurements [*van Hest*, 1996].

The transition Reynolds number can be used to compute the Reynolds number
based on the boundary layer momentum thickness at the start of transition $Re_{\theta,tr}$.
According to the Blasius solution this number is given by $Re_{\theta,tr} = 0.664\sqrt{Re_{tr}}$
[*Schlichting*, 1979]. Figure 5.13 shows this Reynolds number versus the free
stream turbulence intensity for experiments with M=0.18 and 0.36. These data
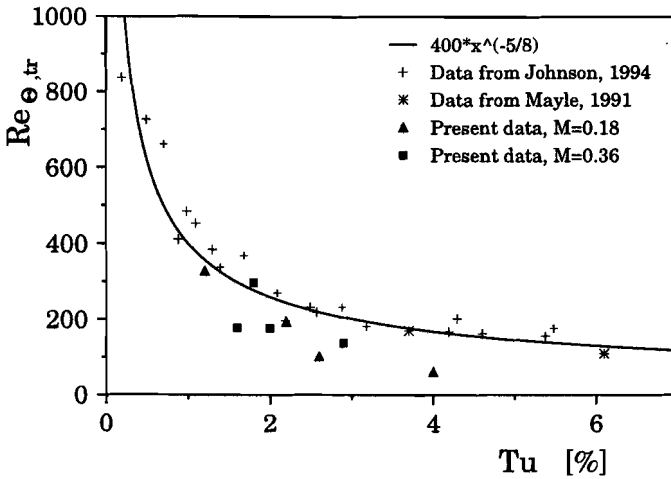
*Figure 5.13: Momentum thickness Reynolds number at the transition. Experimental results in comparison with existing data sets (incompressible flow with zero pressure gradient).*

are compared with experimental results obtained from the literature. A reasonably good agreement with other (incompressible) data is obtained for free stream turbulent levels between 1 and 2%, whereas transition is obtained too early at higher free stream levels. The difference increases with increasing free stream turbulence intensity. Especially the experiment with a turbulence level equal to 4.0% shows a very fast transition. It is not unlikely that this experiment was performed at the critical angle as described before. No essential differences are found between the data at Mach number 0.18 and 0.36, which means that in this low Mach number range, compressibility has a negligible influence on the transition onset. It is interesting to see from figure 5.13 that the present results contain experiments with almost equal turbulence levels but with significant differences in transition onset. These results are systematic as the experiment can easily be reproduced. Some more details about this contradictory behaviour are shown in figure 5.14. This figure presents the intermittency against the Reynolds number for the experiments shown in figure 5.13. The corresponding Mach numbers, unit-Reynolds numbers, turbulence levels and grid numbers are printed below the figure. Obviously the transition results depend on the type of grid used. Not only the grid type is important but also the free stream turbulence level has some influence. A clear example is found in the experiments at $M=0.36$ with grid numbers 1 and 2. The experiment with the second grid has a lower turbulence level, but shows an earlier transition. This may be explained by the influence of the mesh size of the turbulence grid as reported in section 2.5. However, the transition data of experiments with grid 2 and 3 show that the mesh size is not
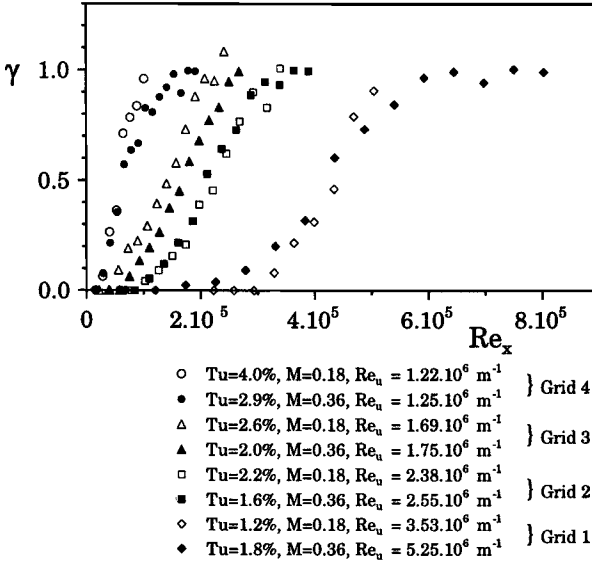
*Figure 5.14: Intermittency of transitional boundary layers for different combinations of Mach numbers, free stream turbulence levels, and mesh sizes.*

dominant. Whereas the mesh size of grid 3 is smaller than that of grid 2, the transition is earlier.

The effect of the free stream turbulence level is eliminated in the experiment shown in figure 5.15. In this experiment grid 2 and grid 3 were used, while equal free stream turbulence levels were generated at equal Mach number. Although the unit-Reynolds value is also different, it is expected that due to the scaling of the horizontal axis its influence is negligible and that the differences can mainly be attributed to the turbulence. The start of the transition as well as the length are different again. The largest geometrical difference between grids 2 and 3 is the blocked space: the solidity ($\sigma_2$=0.14, $\sigma_3$=0.33). Grid 3 has a larger rod diameter.

*Hall and Gibbings* [1972] showed the importance of the mesh size. They found that turbulence generated with a smaller mesh size leads to earlier transition than turbulence produced with coarser meshes with equal turbulence levels. In the present experiments the mesh sizes applied are smaller than the mesh sizes applied in the experiments of *Hall and Gibbings* [1972]. This should lead to earlier transition. However, the trend that a smaller mesh size gives earlier transition is not consistently observed in the present experiments. *Hall and Gibbings* [1972] found some scatter in their experiments also. This shows that more work is needed to make stronger conclusions possible.

Another aspect that attracts attention in the experiments with grid 1 con-
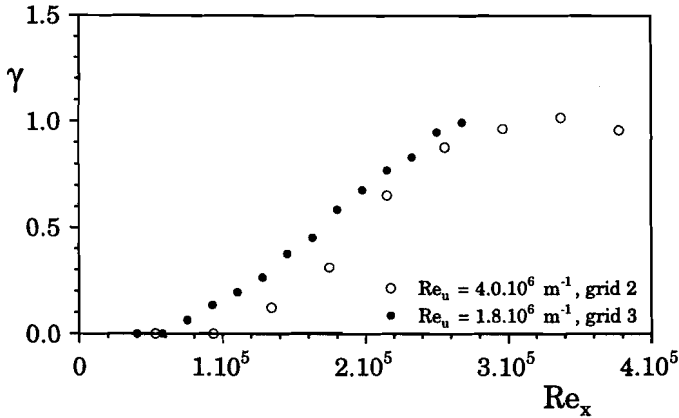
*Figure 5.15: Intermittency versus Reynolds number for equal free stream turbulence level and equal Mach number but with different grids (M=0.36, Tu=2.0%).*

cerns the difference in transition lengths. While the experiment with the lower free stream turbulence level shows a later start, the transition length is shorter and the curve of the data points intersect that of the experiment with the higher free stream turbulence level. This may lead to the conclusion that the transition length depends on either the unit-Reynolds number or the Mach number.

## 5.5    Universal intermittency distribution

In the literature the intermittency distribution in the transition region is frequently compared with Narasimha's universal intermittency distribution given by [*Dhawan and Narasimha, 1958*]:

$$\gamma(\xi) = 1 - \exp(-0.411\xi^2) \qquad (5.8)$$

where $\xi$ is the non-dimensional stream-wise coordinate defined as[1]:

$$\xi = \frac{Re_x - Re_{tr}}{Re_\lambda} \qquad (5.9)$$

where $Re_\lambda$ is the Reynolds number based on the stream-wise distance between the location where the intermittency is equal to 0.25 and 0.75. The value 0.411 in equation 5.8 follows from the introduction of the parameter $\xi$ into equation 2.1. The universal intermittency distribution according to equation 5.8 is drawn in figure 5.16 (solid line). The experimental data have been transformed to the parameter $\xi$ using the least-squares fit discussed in section 5.4. From the

---

[1] Here $\xi$ is written in terms of Reynolds numbers to have a consistent notation
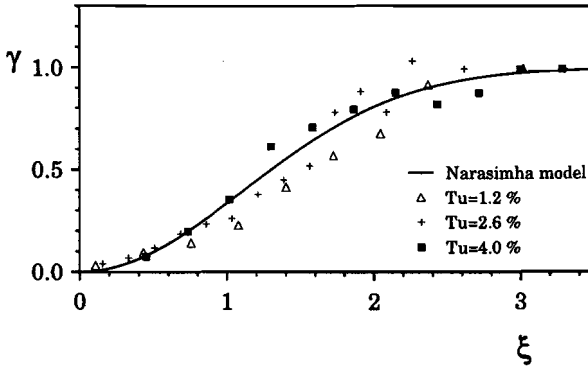
*Figure 5.16: Intermittency comparison with the Narasimha model for experiments with free stream turbulence levels of 1.2, 2.6 and 4.0 % (M=0.18).*

individual fit $Re_\lambda$ $(= 0.641/B)$ and $Re_{tr}$ $(=-A/B)$ are determined, leading to the following for the scaling of experimental data:

$$\xi = \frac{A + BRe_x}{0.641} \tag{5.10}$$

It should be noted that the scaling of $\xi$ depends on the fit with the data. Some experimental data are shown in figure 5.16 for an experiment with a Mach number equal to 0.18 at free stream turbulence levels varying from 1.2% to 4.0%. It can be seen that the free stream turbulence level has a weak influence on the intermittency distribution. The intermittency for the turbulence level of 1.2% has a distribution below the Narasimha model, whereas the intermittency for the experiment with $Tu$=4.0% matches very well. The experiment with 2.6% is located in between. The same trend holds for experiments with Mach numbers equal to 0.36 [*Hogendoorn et al.*, 1997].

Johnson and Fashifar [1994] proposed a variation of the Narasimha distribution. They assumed that the spots are not generated on one line, but that spots can start from $Re_{tr}$ on with linearly increasing probability. Using the same parameter $\xi$, the intermittency distribution reads

$$\gamma = 1 - \exp(-0.0941\xi^3) \tag{5.11}$$

The procedure to fit this model with the experimental data is similar to that of the Narasimha model ($Re_{tr} = -A/B$, $Re_\lambda = 0.455/B$). A comparison of this model to the experimental results is given in figure 5.17 for a Mach number equal to 0.18. It is observed that the intermittency distribution according to the Johnson model is a bit closer to the model prediction than that of the Narasimha model. However, the differences are small.
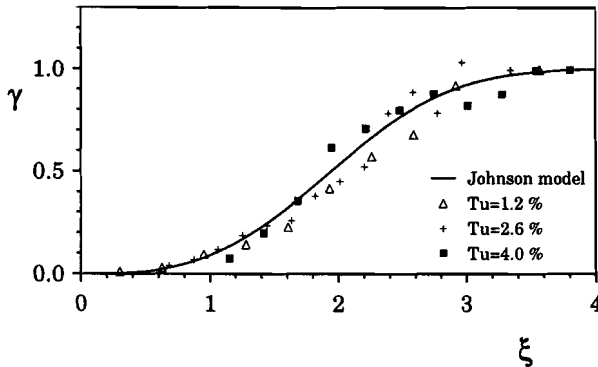
*Figure 5.17: Intermittency comparison with the Johnson model for experiments with free stream turbulence levels of 1.2, 2.6 and 4.0 % (M=0.18).*

## 5.6    Effect of free stream turbulence and Mach number on the transition length

From figure 5.14 it can be observed that a considerable part of the object under consideration can be covered by the transition region. Hence, it is valuable to study the effect of free stream turbulence and Mach number on the length of boundary layer transition. The transition length for the different experiments is determined in terms of the dimensionless spot production rate $\hat{n}\sigma$. This production rate includes both the number of generated spots (equation 2.2) and the spot growth (equation 2.3). In section 5.4 it was shown that the spot production rate results from a least-squares fit ($\hat{n}\sigma = B^2$). The higher the production rate, the shorter the transition region. In chapter two it was shown that this parameter strongly depends on the free stream turbulence level. A higher degree of perturbation leads to more turbulent spot initiations. The fits for different experiments are shown in figure 5.18 given by the solid lines. The dashed lines are two experimental curves from *Mayle* [1991] for free stream turbulence intensities of 1 % and 10 %. The present experimental curves are clearly within this range. From these fits the dimensionless spot production rates versus the free stream turbulence intensities can be obtained. These are compared with experimental data given by *Mayle* [1991] in figure 5.19. Mayle proposed the experimental fit given by

$$\hat{n}\sigma = 1.5 \times 10^{-11} T u^{7/4} \tag{5.12}$$

The present results correspond very well with this fit. For a Mach number equal to 0.36 the spot production rate seems to be slightly higher than that of the lower Mach number and the incompressible data of Mayle. However, the differences are not significant.
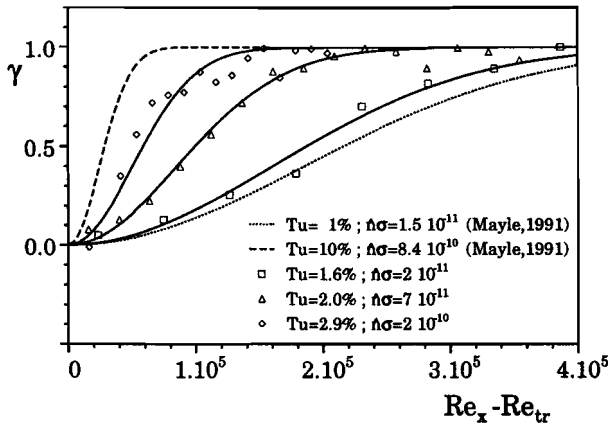
*Figure 5.18: Intermittency for different turbulence intensities in comparison with the dimensionless spot formation rate $\hat{n}\sigma$. The solid lines are the best fit functions through the data (M =0.36).*

## 5.7    Conclusions

In this chapter it has been shown that besides the geometrical self-similarity of the turbulent spot, the heat transfer rate due to a turbulent spot is self-similar too. This property also holds for a spot travelling in the calmed region of a previous spot.

After the origination of a spot, the propagation velocity of the leading edge as well as the trailing edge are constant. The measured propagation velocities correspond with 'incompressible' data sets. Compressibility effects seem to have a negligible influence on the propagation and spot growth up to a Mach number of at least 0.33. It is shown that the heat transfer level inside the spot corresponds to the empirical relation for fully turbulent heat transfer. Near the trailing edge the heat transfer is somewhat higher. The calmed region plays an essential role in the total heat transfer rate due to a single spot. Its relative portion includes about 26% of the total heat transfer due to a spot.

The intermittency distribution is obtained on the basis of the time-averaged heat flux. The intermittency in the transition region can be reproduced within $\pm$ 2%, which shows that the test time of the Ludwieg tube is sufficiently long to perform accurate measurements.

It is found that transition experiments with a flat plate and a sharp leading edge are sensitive for angles of attack that are too small. In this case turbulent spots are generated with a considerable size at the leading edge.

For Mach numbers up to 0.36 at least, the onset of transition seems to have a negligible dependency. On the other hand the onset is shown to be strongly
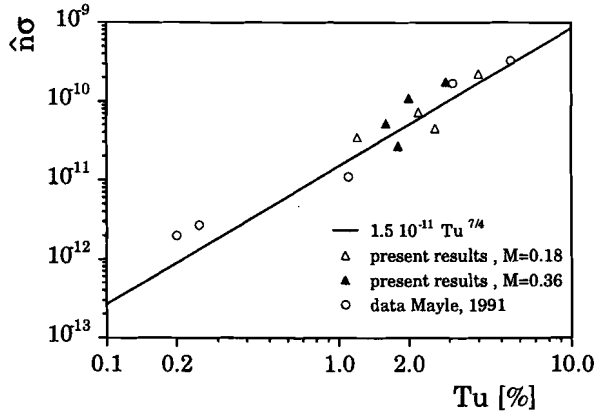
*Figure 5.19: Spot production rate as a function of free stream turbulence level in comparison to other data.*

dependent on the free stream turbulence level as well as on the mesh size of the turbulence generating grid. Probably, the grid solidity has some influence too. In this field much experimental work is still needed. Up to now the scatter in experimental data is large, based on the free stream turbulence level as a single input parameter. It is necessary to reduce this scatter. Little research has been done on the influence of the turbulence structure on the transition onset. Probably, it would be useful to take the power spectrum of the generated free stream turbulence into account. The boundary layer has different kinds of sensitivities to the scales present in the turbulence offered. In this way a formulation in terms of mesh size (which is less relevant in turbine flow conditions) can be avoided.

The spot production rates obtained in the present study correspond well with the existing data sets. For Mach numbers up to 0.36, the influence of compressibility is small. The transition length is found to be that long that it must be taken into account.

# Chapter 6

# Concluding discussion

In this thesis we have shown that the Ludwieg tube is suitable for accurate bound-
ary layer transition experiments in subsonic flow at higher free stream turbulence
levels. The accuracy of reproduction is high and the flow conditions are constant.
Furthermore, the unit-Reynolds number, Mach number, and free stream turbu-
lence level can be varied freely over a wide range.

The accuracy of cold thin film gauges is improved considerably. The opti-
mization of the sensor was obtained with a design strategy based on the balance
between increasing accuracy as a result of higher voltage and decreasing accuracy
due to thermal effects as a result of increasing dissipation.

Heat transfer measurements show that the heat transfer of a turbulent spot
is self-similar. The calmed region appears to play an important role in the heat
transfer process. A more extensive investigation of the heat transfer structure in
the lateral direction of a turbulent spot should lead to a better understanding of
the internal structure and to better modeling. The data set for subsonic Mach
numbers and higher free stream turbulence levels for transition measurements on
a flat plate is extended. Measurements show that the effect of compressibility
on transition is negligible up to the Mach number of 0.36. Regarding transition
onset, both the effect of the turbulence structure and of the turbulence level are
found to be very important.

In comparison to other work, the conditions in the Ludwieg tube are more con-
stant than those of the Isentropic Light Piston Tunnel. Moreover, the Ludwieg
tube facility is several times cheaper. A disadvantage of the latter set-up is the
lower heat flux, resulting in less accurate heat transfer measurements. This effect
is eliminated partially by the improved measuring technique. While improving
the sensor accuracy the relative noise level reduction by differential amplification
is not taken into account. If this positive result is utilized the accuracy of heat
flux measurements can probably be further improved. This effect should there-
fore be studied in more detail. Due to the complexity of the experiments, it is
recommended that the sensor lay-out be designed such that it is suitable for the

measurement of only one specific feature (e.g. intermittency or spot propagation).

The results for boundary layer transition onset agree with results from literature for free stream turbulence levels lower than 2%. At higher levels an earlier transition is obtained. It seems that the turbulence structure plays an important role. Little experimental data are available in this field, and much work is still required. The Ludwieg tube is a suitable set-up to study this. A fundamental approach is necessary here. Although it is very difficult, attempts must be made to separate turbulence structure from the intensity. This could be realized by using single upstream cylinders, generating specific frequencies. Also the three-dimensionality of the turbulence (non-isotropy) may play an important role in transition. The spot formation rate and transition length correspond well to results presented in literature. It seems that the Mach number up to the current value does not affect the transition length. It is expected that compressibility starts to play a part in boundary layer transition for Mach numbers above the value of about 0.4. With the present Ludwieg tube the Mach number can be raised to transonic values by means of a contraction at the location of the flat plate. Moreover, the turbulence level can be elevated to about 10%. In this way the Ludwieg tube can be used to extend the present data set of transition experiments at high free stream turbulence levels from low Mach numbers up to transonic flows. These values are representative for turbine flow conditions.

# References

A. Abtahi and P. Dean. Heat flux sensor research and development: the cool film calorimeter. *NASA CR 189789*, 1990.

B.J. Abu-Ghannam and R. Shaw. Natural transition of boundary layers - the effects of turbulence, pressure gradient, and flow history. *J.Mech.Eng.Sci.*, 22:213–228, 1980.

D. Arnal. Boundary layer transition: predictions based on linear theory. *AGARD Report R-793*, 1994.

W.D. Baines and E.G. Peterson. An investigation of flow through screens. *Trans. ASME.*, 73:467–480, 1951.

J.N. Bradley. *Shock Waves in Chemistry and Physics*. Methuen and Co Ltd, London, 1962.

K.S. Breuer and J.H. Haritonidis. The evolution of a localized disturbance in a laminar boundary layer. part 1: Weak disturbances. *J. Fluid Mech.*, 220:569–594, 1990.

K.S. Breuer and M.T. Landahl. The evolution of a localized disturbance in a laminar boundary layer. part 2. strong disturbances. *J. Fluid Mech.*, 220:595–621, 1990.

H.H. Bruun. *Hot-wire anemometry*. Oxford University Press, 1995.

B. Cantwell, D. Coles, and P. Dimotakis. Structure and entrainment in the plane of symmetry of a turbulent spot. *J. Fluid Mech.*, 87:641–672, 1978.

K.K. Chen and N.A. Thyson. Extension of emmons' spot theory to flows on blunt bodies. *AIAA J.*, 9:821–825, 1971.

C.Y. Ching and J.E. LaGraff. Measurements of turbulent spot convection rates in a transitional boundary layer. *Exp. Therm. Fluid Sci.*, 11:52–60, 1995.

J.P. Clark, T.V. Jones, and J.E. LaGraff. On the propagation of naturally-occurring turbulent spots. *J. Engng. Maths.*, 28:1–19, 1994.

G. Comte-Bellot and S. Corrsin. The use of a contraction to improve the isotropy of grid-generated turbulence. *J. Fluid Mech.*, 25:657–682, 1966.

H. Consigny and B.E. Richards. Short duration measurements of heat transfer rate to a gas turbine rotor blade. *J.Eng.Power*, 104:542–551, 1982.

W.R. Davies and L. Bernstein. Heat transfer and transition to turbulence in the shock-induced boundary layer on a semi-infinite flat plate. *J. Fluid Mech.*, 36:87–112, 1969.

S. Dhawan and R. Narasimha. Some properties of boundary layer flow during the transition from laminar to turbulent motion. *J. Fluid Mech.*, 3:418–436, 1958.

T.E. Diller. *Advances in heat flux measurements (in: Advances in heat transfer)*, volume 23. Academic Press Inc., 1993.

J.E. Doorly and M.L.G. Oldfield. New heat transfer gages for use on multilayered substrates. *J. Turbomach.*, 108:153–160, 1986.

H.W. Emmons. The laminar-turbulent transition in a boundary layer- part 1. *J. Aero. Sci.*, 18:490–498, 1951.

A.H. Epstein and G.R. Guenette. High-frequency response heat-flux gauge. *Rev. Sci. Instrum.*, 57:639–649, 1986.

L.M. Fingerson and P. Freymuth. *Fluid mechanics measurements.* Taylor and Francis, 1996.

F.N. Frenkiel and N.Y. Ithaca. The decay of isotropic turbulence. *Trans. ASME.*, 70:311–321, 1948.

M. Gad-el Hak, R.F. Blackwelder, and J.J. Riley. On the growth of turbulent regions in laminar boundary layers. *J. Fluid Mech.*, 110:73–95, 1981.

A. Glezer, Y. Katz, and I. Wygnanski. On the breakdown of the wave packet trailing a turbulent spot in a laminar boundary layer. *J. Fluid Mech.*, 198:1–26, 1989.

J.P. Gostelow. Modelling the transition region. In *European Research Community On Flow Turbulence And Combustion Bulletin*, volume 25, pages 9–12, 1995.

J.P. Gostelow and A.R. Blunden. Investigations of boundary layer transition in adverse pressure gradient,. *J. Turbomach.*, 111:366–375, 1989.

J.P. Gostelow, A.R. Blunden, and G.J. Walker. Effects of free-stream turbulence and adverse pressure gradients on boundary layer transition. *J. Turbomach.*, 116:392–404, 1994.

H.L. Grant and I.C.T. Nisbet. The inhomogeneity of grid turbulence. *J. Fluid Mech.*, 2:263, 1957.

D.J. Hall and J.C. Gibbings. Influence of stream turbulence and pressure gradient upon boundary layer transition. *J.Mech.Eng.Sci.*, 14:134–146, 1972.

F.R. Hama, J.D. Long, and J.C. Hegarty. On transition from laminar to turbulent flow. *J.Appl.Phys.*, 28:388–394, 1957.

D.S. Henningson, A. Lundbladh, and A.V. Johansson. A mechanism for bypass transition from localized disturbances in wall-bounded shear flows. *J. Fluid Mech.*, 250:169–207, 1993.

D.S. Henningson, A.V. Johansson, and P.H. Alfredsson. Turbulent spots in channel flows. *J. Eng. Math.*, 28:21–42, 1994.

Ch. Hirsch. Cfd methodology and validation for turbomachinery flows. In *Turbomachinery Design Using CFD - AGARD-LS-195*, 1994.

C.J. Hogendoorn, H.C. de Lange, and A.A. van Steenhoven. Heat transfer measurements in transitional boundary layers. *Proceedings of 2nd European Thermal Sciences and 14th UIT National Heat Transfer Conference, Rome,* G.P. Celata, P. Di Marco and A. Mariani (Editors), Edizioni ETS, pages 593–600, 1996.

C.J. Hogendoorn, H.C. de Lange, A.A. van Steenhoven, and M.E.H. van Dongen. Influence of turbulence intensity on intermittency model in by-pass transition. *Accepted for presentation at the ASME Turbo Expo '97*, 1997.

F.P. Incropera and D.P. De Witt. *Fundamentals of heat and mass transfer.* John Wiley and Sons, 1990.

M.W. Johnson. A bypass transition model for boundary layers. *J. Turbomach.*, 116:759–764, 1994.

M.W. Johnson and A. Fashifar. Statistical properties of turbulent bursts in transitional boundary layers. *Int. J. Heat Fluid Flow*, 15:283–290, 1994.

Y.S. Kachanov. Physical mechanisms of laminar-boundary-layer transition. *Annu. Rev. Fluid Mech.*, 26:411–482, 1994.

Y. Katz, A. Seifert, and I. Wygnanski. On the evolution of the turbulent spot in a laminar boundary layer with a favourable pressure gradient. *J. Fluid Mech.*, 221:1–22, 1990.

W.M. Kays and M.E. Crawford. *Convective heat and mass transfer.* McGraw-Hill, 1980.

P.S. Klebanoff, K.D. Tidstrom, and L.M. Sargent. The three-dimensional nature of boundary-layer instability. *J. Fluid Mech.*, 12:1–34, 1962.

C.C. Lin. *Turbulent flows and heat transfer.* Princeton University Press, 1959.

C.G. Lomas. *Fundamentals of hotwire anemometry.* Cambridge university press, 1986.

P.J. Magari and J.E. LaGraff. An isentropic compression-heated ludweig tube transient wind tunnel. *Exp. Therm. Fluid Sci.*, 4:317–332, 1991.

R.E. Mayle. The role of laminar-turbulent transition in gas turbine engines. *J. Turbomach.*, 113:509–537, 1991.

R.E. Mayle and K. Dullenkopf. A theory for wake-induced transition. *J. Turbomach.*, 112:188–195, 1990.

H. Mirels. Test time in low-pressure shock tubes. *Phys. Fluids*, 6:1201–1214, 1963.

H. Mirels. Shock tube test time limitation due to turbulent-wall boundary layer. *AIAA J.*, 2:84–92, 1964.

H. Mirels and W.H. Braun. Nonuniformities in shock-tube flow due to unsteady-boundary-layer action. *NACA TN 4021*, 1957.

R. Narasimha. The laminar-turbulent transition zone in the boundary layer. *Prog. Aerospace. Sci.*, 22:29–80, 1985.

J.E. O'Brien. A technique for measurement of instantaneous heat transfer in steady-flow ambient-temperature facilities. *Exp. Therm. Fluid Sci.*, 3:416–430, 1990.

J.P.J. van den Oever. Development of a heat flux sensor. Master's thesis, Eindhoven University of Technology, the Netherlands, 1995. WOC-WET 95.027.

J.A. Owczarek. *Gas dynamics.* International Textbook Company, 1964.

E. Reshotko. Laminar flow control - viscous simulation. *AGARD Report R-709*, 1984.

W.M. Rohsenow and H. Choi. *Heat, mass, and momentum transfer.* Prentice-Hall, 1961.

G. Rudinger. Effect of boundary-layer growth in a shock tube on shock reflection from a closed end. *Phys. of Fluids*, 4:1463–1473, 1961.

H. Schlichting. *Boundary-Layer Theory*. McGraw-Hill Book Company, seventh edition, 1979.

S.P. Schneider and C.E. Haven. Quiet-flow ludwieg tube for high-speed transition research. *AIAA J.*, 33:688–693, 1995.

G.B. Schubauer and P.S. Klebanoff. Contributions on the mechanics of boundary-layer transition. *NACA Tech. Note TN 3489*, 1955.

D.L. Schultz, M.L.G. Oldfield, and T.V. Jones. Heat transfer rate and film cooling effectiveness measurements in a transient cascade. *AGARD-CP 281*, 1980.

A. Seifert, M. Zilberman, and I. Wygnanski. On the simultaneous measurement of two velocity components in the turbulent spot. *J.Eng.Math.*, 28:43–54, 1994.

R.J. Simoneau and F.F. Simon. Progress towards understanding and predicting heat transfer in the turbine gas path. *Int.J.Heat Fluid Flow*, 14:106–127, 1993.

J.C. Simonich and P. Bradshaw. Effect of free-stream turbulence on heat transfer through a turbulent boundary layer. *ASME J. Heat Transfer*, 100:672–677, 1978.

P.C. Stainback and K.A. Nagabushana. *Review of hot-wire anemometry technique and the range of their applicability*. FED-Vol. 167 Thermal Anemometry 1993, ASME, 1993.

J.A. Steketee. Note on a formula of h.w. emmons. *J.Aero.Sci.*, 22:578–579, 1955.

K.F. Stetson and R.L. Kimmel. Unit-reynolds-number effects on boundary layer transition. *AIAA J.*, 31:195–196, 1993.

J. Tan-Atichat, H.M. Nagib, and R.I. Loehrke. Interaction of free-stream turbulence with screens and grids: a balance between turbulence scales. *J.Fluid Mech.*, 114:501–528, 1982.

J.W. Trolier and R.E. Duffy. Turbulence measurements in shock-induced flows. *AIAA J.*, 23:1172–1178, 1985.

B.F.A. van Hest. *Laminar-turbulent transition in boundary layers with adverse pressure gradient*. PhD thesis, Delft University of Technology, the Netherlands, 1996.

B.F.A. van Hest, D.M. Passchier, and J.L. van Ingen. The development of a turbulent spot in an adverse pressure gradient boundary layer. In *Proceedings, IUTAM Symposium, Symposium on Turbulence*, Sendai, 1994.

C.A. Vergers. *Electrical noise measurement and technology*. TAB Books, 1987.

R.J. Volino and T.W. Simon. Bypass transition in boundary layers including curvature and favorable pressure gradient effects. *NASA CR 187187*, 1991.

D.A. Walker and M.D. Walker. Experimental comparison of two hotwire techniques in supersonic flow. *AIAA J.*, 27:1074–1080, 1989.

I. Wygnanski, M. Sokolov, and D. Friedman. On a turbulent 'spot' in a laminar boundary layer. *J. Fluid Mech.*, 78:785–819, 1976.

I. Wygnanski, J.H. Haritonidis, and R.E. Kaplan. On a tollmien-schlichting wave packet produced by a turbulent spot. *J. Fluid Mech.*, 92:505–528, 1979.

M.Y. Zhang, F.K. Tsou, X.J. Chen, and S.J. Chen. Film cooling experimental technique using a ludwieg tube wind tunnel. *Exp. Therm. Fluid Sci.*, 6:186–195, 1993.

L.M. Zysina-Molozhen and V.M. Kuznetsova. Investigation of transition conditions in a boundary layer. *Teploenergetika*, 16:16–20, 1969.

# Appendix A

# Shock tube driven Ludwieg tube

## A.1  Set-up

The shock tube is a very frequently applied experimental facility with applications in chemistry, biology and physics. The combination of well defined conditions over a very wide range of Mach numbers and temperatures and its relatively simple construction, makes this set-up unique.

In spite of the manifold applications in a number of research branches, very few articles are available concerning application in detailed boundary layer transition research.

The shock tube set-up as employed (figure A.1) has been used as a driver of the Ludwieg tube. The set-up consists of a high pressure section (HPS, length 3 meters, diameter 0.14 $m$), a low pressure section (LPS, length 10 meters, area $0.1 \times 0.1\ m^2$), a test section (TS) with orifice (O), and a dump tank (DT) (volume is 0.43 $m^3$). The HPS can be detached easily from the LPS and is movable in order to replace the diaphragm (D) for each experiment. Diaphragms of 50 and 120 $\mu m$ thick Melinex were used, which can resist pressure differences of 2 and 6 bar, respectively. Opening is obtained by means of an electrically heated cross-wire. For higher pressure differences a 0.5 or 1 $mm$ thick aluminium diaphragm is used, which is carved at a certain depth. In the case of the aluminium membranes the pressure in HPS is slowly increased until the diaphragm spontaneously ruptures. The incision depth determines the pressure of rupture and consequently the experimental conditions. A disadvantage of the latter system is that the conditions can not be reproduced very accurately.

With a gas cylinder (GC) the HPS is pressurized at the desired pressure read from manometer (MM). Excess-pressure is reduced by a valve (V). The LPS can be evacuated with a vacuum pump (VP) below 100 $Pa$ and pressurized to the
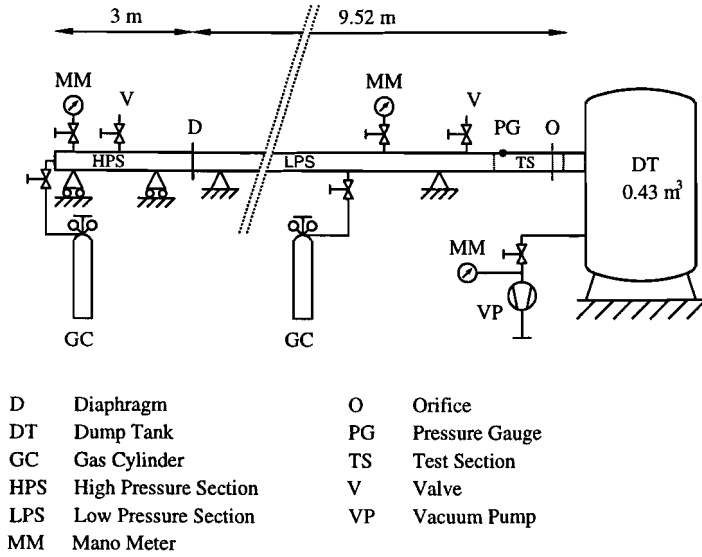
*Figure A.1: Schematic diagram of the experimental shock tube set-up.*

desired pressure with an arbitrary gas from a gas cylinder[1]. The LPS pressure can be adjusted within 100 $Pa$ using the manometer.

After the experiment is performed the set-up is taken at ambient pressure with the valve on the tube.

## A.2   Principle

The principle of a shock tube is based on the application of gas dynamical waves. Figure A.2 shows the space-time representation of wave patterns occurring in a shock tube. After the diaphragm has been ruptured a shock wave is generated that runs into the LPS, while an expansion wave runs into the HPS. The medium bounded by the two waves flows into the LPS. It has a constant velocity and contains a cold and a hot part, divided by the contact surface. The cold medium is the expanded high pressure gas (region 3), the hot medium is heated by the shock wave (region 2). The shock wave runs faster than the medium behind, thus causing an extension of region 2 with time. Regions 1 and 4 are the undisturbed LPS and HPS. When the incident shock reaches the orifice (smallest cross-sectional area in the tube) a new equilibrium is created. Due to the supercritical pressure ratio across the orifice, the flow becomes choked locally and becomes supersonic downstream of the orifice. As a consequence no disturbance returns from the

---

[1] For experiments with air the maximum pressure is the pressure from the environment.
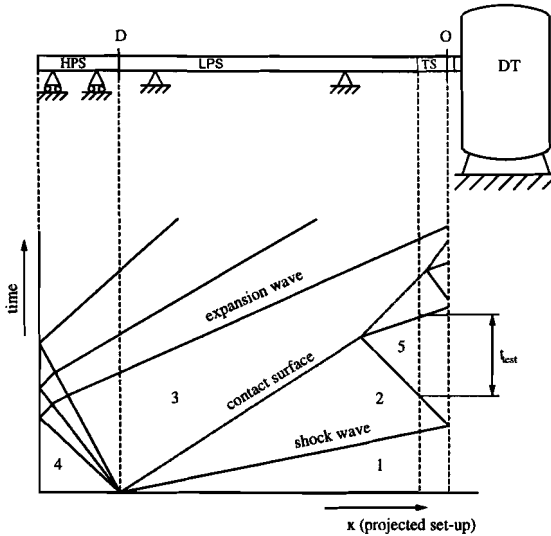
*Figure A.2: Space-time representation of wave patterns in an x,t-diagram for a shock tube set-up.*

DT. The new equilibrium makes that the upstream mass flow is corrected by a reflected shock wave moving upstream in the direction of the contact surface. The hot gas flow will be steady after this reflection (region 5) until the shock wave, reflected at the contact surface, disturbs this steady situation. The time that a steady flow is present at the TS is the test time $t_{test}$.

The performance of shock tube set-up with respect to research in boundary layer transition in subsonic flows, will be discussed in this appendix. Different aspects were studied. With experiments the prediction of flow conditions with one-dimensional inviscid gas-dynamical shock tube relations can be verified. Visualizations were performed to study the flow development around a complex geometry in time. Furthermore, quantitative heat flux measurements were carried out.

## A.3   Determination of flow conditions

With the application of 1-D inviscid conservation equations etc. [*Owczarek*, 1964] the flow conditions in different regions (2,3 and 5) can be computed. In figure A.3 both the theoretically predicted and measured pressure in front of the test section are shown for a shock tube experiment. The first pressure jump is the arrival of the incident shock, whereas the second jump is a result of the shock reflection at the test section. After this reflected shock has passed, a steady hot flow is
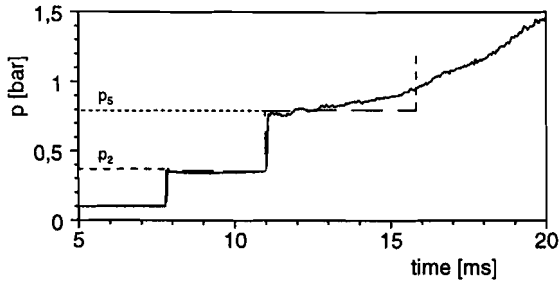
*Figure A.3: One-dimensional theory (dashed lines) compared with shock exper-*
*iments (solid lines),(Ar-air, $p_4 = 3.32 \times 10^5$ Pa, $p_1 = 1.02 \times 10^4$ Pa, dis-*
*tance diaphragm-orifice is 9.52 m, distance diaphragm-pressure gauge is 7.3 m,*
$T_1 = T_4 = T_{ambient} = 293K$, $M_5 = 0.178$, *test section TS1a)*

offered to the test section and the test time starts. This steady flow terminates
as a result of a second reflection of the reflected shock at the contact surface.
This should be expected as a third shock at the time that the vertical dashed line
is plotted. However, it is observed that there is no clear shock reflection. This
phenomenon will be discussed later. The conditions behind the initial shock can
easily be computed using the standard shock tube relations *Owczarek* [1964]. The
conditions after the different shock reflections can be determined iteratively. To
that end a balance is made using the different conservation equations together
with a prescribed flow Mach number behind the first shock reflection (the flow is
again choked, so the upstream Mach number after shock reflection, $M_5$, can be
computed with equation 3.3). The test time can be determined when the condi-
tions after the shock-contact surface interaction are computed. However, because
no clear shock reflection is observed, a good comparison can not be carried out.
It should be noted that the duration of the pressure plateau $p_5$, shown is longer
for the test section than for the place where the pressure is measured.

The comparison of the theoretically predicted pressure with the measured
pressure is shown in figure A.3. The difference is about 2% initially. A slightly
lower pressure after the first shock reflection is observed. This is due to viscous
dissipation, which has been extensively discussed by *Mirels and Braun* [1957],
*Mirels* [1963], *Mirels* [1964] and *Rudinger* [1961].

There is an increasing difference between the theoretically predicted and ex-
perimentally measured pressure in region 5. Where a pressure plateau $p_5$ is
expected (according to inviscid 1D theory), a continuously increasing pressure is
observed.

The increasing pressure causes changing flow conditions within the test sec-
tion during test time. This effect reduces the accuracy significantly. In the next
part the relation between the pressure increase and the Reynolds number, shock
strength and thermal gas properties will be discussed.

## A.3.1 Influence of unit-Reynolds number

Before the Reynolds contribution is discussed, it should be noted that the pressure signals are very reproducible. The signal does not depend on the type of diaphragm. Equal pressure signals have been obtained with $2mm$ thick aluminium diaphragms and $50\mu m$ thick Melinex diaphragms.

*Mirels and Braun* [1957] found that boundary layer growth induces a pressure increase. The boundary layer growth itself is a function of the Reynolds number. Hence, it can be expected that the pressure increase is a function of the Reynolds number. Figure A.4 shows three shock experiments with the same initial pressure ratio and different unit-Reynolds numbers in region 2: $2.2 \times 10^6$, $6.6 \times 10^6$ and $11.0 \times 10^6$ $[m^{-1}]$. The initial pressure ratio was 21.4 and a closed test section was used ($M_5 = 0$). From figure A.4 a slight influence of the unit-Reynolds number
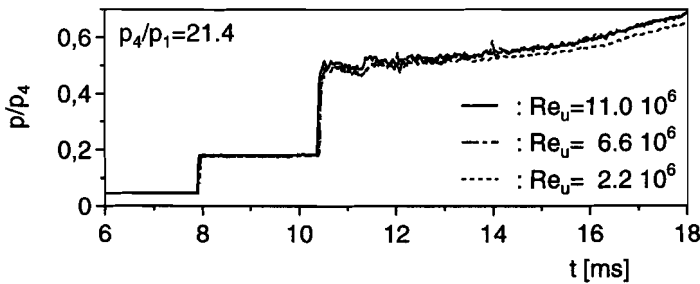


*Figure A.4: The scaled pressure increase (0.52 m before closed end) for fixed initial pressure ratio ($p_4/p_1 = 21.4$) and different unit-Reynolds numbers. Region 2: $Re_u = 2.2 \times 10^6$, $6.6 \times 10^6$ and $11.0 \times 10^6$ $[m^{-1}]$.*

can be observed. The lowest $Re_u$ number shows a slightly lower pressure at the end of the recording. However, the pressure differences in region 5, are hardly significant. The Reynolds number influence for experiments with pressure ratios equal to 11.4 and 33.7 shows comparable results.

## A.3.2 Influence of shock strength

A parameter that has an important effect on the pressure increase after the first shock reflection is the shock strength. This strength is determined by the initial pressure ratio, $p_4/p_1$, and the gases applied. Figure A.5 shows the pressure signal, scaled with the pressure immediately after the shock reflection, for experiments with different shock strengths. The initial pressure ratios are equal to 11.4, 20.4 and 33.7. From figure A.5 it can be concluded that the shock strength has an important effect on the pressure increase at the test section. The experiment, which uses an initial pressure ratio of 11.4, results in a relative pressure increase of 4 % after 6 $ms$. If the pressure ratio is 33.7, the relative pressure rise is 42 %.
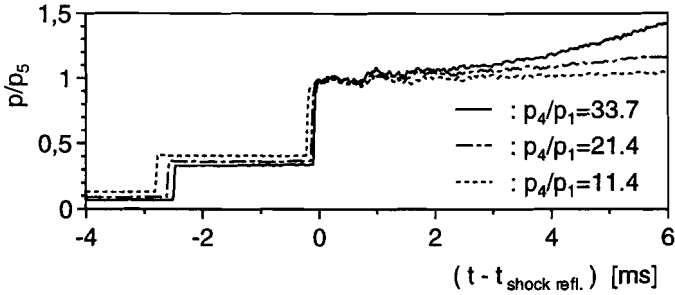
*Figure A.5: Normalized pressure (0.52 m before the tube's closed end) for different shock strengths: $p_4/p_1 = 11.4$, $20.4$ and $33.7$ ($N_2$-air).*

The test time, based on a 10 % pressure increase criterion, results in a value of 2.5 *ms* for the latter pressure ratio.

### A.3.3   Effect of boundary layer separation

For air (diatomic gas) it is known [*Bradley*, 1962] that shock reflection causes separation of the boundary layer for incident Mach numbers between 1.3 and 6.5. Monotomic gases, like argon and helium do not show this effect. Although the incident Mach number is lower than 1.3, a possible influence was checked, comparing the gases nitrogen and argon. The results of the experiment using the same Reynolds number with different shock strengths shows that no significant differences can be obtained. The same can be said for the experiment using the same shock strengths. It can be concluded that for the present range of conditions no significant difference was observed between experiments with argon and with nitrogen. This confirms results found earlier.

### A.3.4   Variation of flow conditions

The variation of the dynamic and thermodynamic state of the gas during the test-period is mainly determined by the pressure increase discussed before (figure A.3). For weaker shocks the variation is less than for stronger shocks. The variation also increases with increasing time. For a pressure ratio, $p_4/p_1$, equal to 11.4, the relative pressure increase in the test section is about 10 % after 14 *ms* for a flow with a Mach number, $M = 0.33$.

Inaccuracies due to errors in initial pressure adjustments in the HPS and the LPS,

together with errors in measuring the static pressure with the pressure gauge, are small compared to the inaccuracies mentioned before.

## A.3.5 Reproduction of experiments

The experiments show that the flow conditions can be easily reproduced. If the averaged pressures in region 5 of two experiments are compared, a relative difference of less than 0.2% is found. For this experiment the pressure in HPS was $2.45 \times 10^6$ $Pa$, the pressure in LPS was $3.52 \times 10^4$ $Pa$ with $Re_u = 5.4 \times 10^6$ $[m^{-1}]$ and $M_5 = 0.33$. The high accuracy of reproduction can be attributed to the accurate initial pressure adjustment and the choking condition at the orifice.

## A.3.6 Available range for Mach number, unit-Reynolds number and temperature difference

Using the results obtained before, a range can be given concerning the available conditions. The unit-Reynolds number was varied between $2.4 \times 10^6$ and $11.0 \times 10^6$. A wider range is feasible. The temperature difference mainly depends on the shock strength and has a value between $124$ $K$ and $300$ $K$. The Mach number, $M_5$, can be varied up to approximately 0.7 (no orifice in the test section). The latter value is the flow Mach number behind the incident shock. It should be noted that the Reynolds number, the Mach number and the temperature difference can be varied independently. The tested range is shown in figure A.6. The mass flux turbulence intensity in region 5 depends on the unit-Reynolds number and varies from 2 to 6 % [*Trolier and Duffy, 1985*].
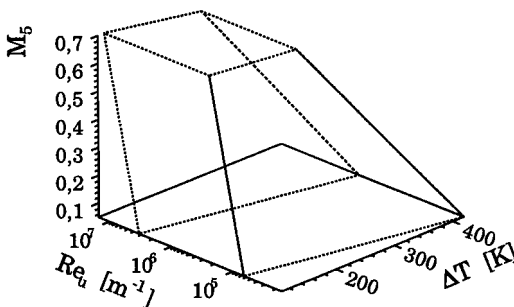


*Figure A.6: The three-dimensional range of the conditions that can be obtained with the shock tube.*

## A.4   Flow visualization and heat flux measurements

After a flow is initiated, some time is required to obtain a steady situation. Boundary layers grow, recirculation zones have to develop, etc. Depending on the geometrical complexity of the test object or test section, some time is required for flow development. When these times are comparable with the test time available, no time is left to perform measurements in a steady flow situation. In order to get an impression of these times two different test geometries were used. One complex geometry consists of a cascade of turbine blades and guiding blocks (test section TS2). With this geometry a flow visualization study is performed to study different flow phenomena at different times. To obtain the different phenomena clearly recognizable, the flow in this test section is chosen to be transonic (with subsonic flow upstream and supersonic flow downstream of the object). The orifice is the cascade itself. Figure A.7 shows shadow pictures at different times during the experiment. At $t = 0$ the incident shock wave moving from right to left enters the cascade. The flow is initiated by the shock and starts to develop. Different phenomena, like oblique shock waves and slip-lines in the supersonic flow behind the blades, see figure A.7, clearly indicate the time required. Between 4.5 and 9.5 $ms$ after the flow started, a steady flow is obtained according to the phenomena visualized.

A second study is performed with the test section TS3 discussed before. The heat flux to a flat plate is measured at different locations in the stream-wise direction. The instationary heat flux is directly related to the boundary layer thickness. Figure A.8 shows two different heat flux signals measured at the plate's leading and trailing edge. At $t = 0$ in figure A.8b the incident shock arrives causing a very thin boundary layer with the resultant high heat transfer rate. After about 1.2 $ms$ the reflected shock wave passes. At t=2 $ms$ a steady heat flux is obtained which indicates a fully developed boundary layer at the leading edge. Figure A.8b shows the heat flux at the trailing edge, the location with the largest boundary layer thickness. Since this sensor is situated directly in front of the upper orifice, it is difficult to distinguish the incident from the reflected shock wave. About 2.5 $ms$ are required to obtain a steady boundary layer. It can be concluded that the former, more complex, geometry needs more time to obtain a developed flow compared to the flow around a flat plate. Recirculation zones behind blades and guiding blocks slow down the flow development. For the flows considered, the time required for flow development is about 7 $ms$ for the complex geometry and about 3 $ms$ for the flat plate.

Figure A.9 shows the measured heat flux at 51 $mm$ from the tip of the flat plate over a longer period. At $t = 0$ $ms$ the incident shock arrives at the flat plate, the boundary layers are very thin and the heat flux is very high. The heat flux is peak-shaped in time. Within 1 $ms$ the reflected shock passes, causing a boundary layer that has to stabilize again. After about 2.5 $ms$ the boundary layer becomes steady and a constant heat flux is measured. This level is main-
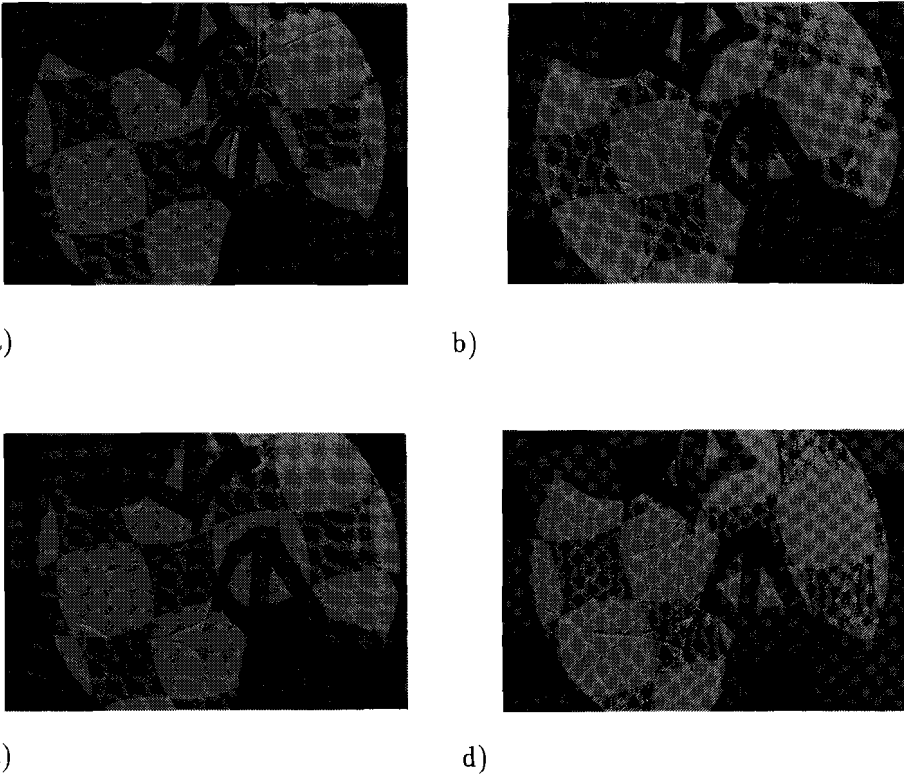
Figure A.7: Shadowgraph pictures showing the development in time of the flow in test section TS2 (a: t=0 (shock arrival), b: t=4.5 ms, c: t=9.5 ms and d: t= 20 ms). The flow is from right to left. For an explanation of phenomena in steady state see figure 3.11.

tained until after 7 ms a flow with higher turbulence intensity is offered. This turbulence is supposed to be generated at the tube wall as a result of shock wave - boundary layer interaction or interaction of the free stream with the reflected shock wave. The transition location shifts forwards. The thin film gauges measure a heat flux level that corresponds with a fully developed turbulent boundary layer. After 20 ms the test time is finished and a decreasing heat flux is observed.

## A.5  Conclusions of shock tube experiments

For the shock tube experiments, the initial difference between the measured and the predicted pressure in region 5 is about 2%. This difference increases during test time and depends on the shock strength. For a shock with initial pressure
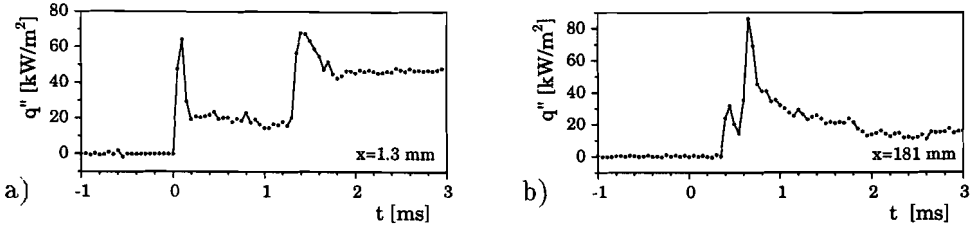
*Figure A.8: Heat flux development at $x = 11.0$ mm (a) and $x = 181.0$ mm (b) from leading edge of the plate (Test section TS3, $M_5 = 0.33$, $Re_u = 2.6 \times 10^6$ $m^{-1}$, $T_5/T_1 = 1.4$, $\gamma_4 = 1.4$).*

ratio $p_4/p_1$ of 11.4 the maximum available test time of the shock experiments is about $14 ms$. Within this time, the pressure increases smoothly by about 10%. For this pressure ratio the flow Mach number can be varied up to 0.7, the temperature increase is $125 K$, while the unit-Reynolds number can be varied at least from $1.6 \times 10^4 < Re_u < 1.5 \times 10^7$ $[m^{-1}]$. The error in pressure reproduction during the test time interval is less than 0.2% for a typical experiment of $M_5 = 0.33$ and $Re_u = 5.4 \times 10^6$ $[m^{-1}]$. It is found that the pressure increase in region 5 (the test region) is almost independent of the unit-Reynolds number in our experimental range. The shock strength, however, is found to be very important. Initial pressure ratios (for $N_2 - air$) above 11.4, lead to less constant conditions and shorter test times.

The lower limit with respect to the shock strength is determined by the required supercritical pressure ratio across the orifice after shock reflection. In the case of a non-choked flow, the pressure waves returning from the dump tank will affect the conditions in the test section.

Finally, it is found that the time required for flow development is about 3 $ms$, which is significantly smaller than the available test time. The turbulence intensity was not measured. Literature reports intensities varying from 2 % to 6% (depending on the unit-Reynolds number). It can be concluded from heat flux measurements that the turbulence intensity during the experiment is not constant. From heat flux measurements we found that about halfway the test time the intermittency increases suddenly, indicating a boundary layer transition. The increasing intermittency is assumed to be a result of the interaction of the travelling shock wave and entering flow.

## A.6    Ludwieg tube versus a shock tube driven Ludwieg tube

In this last section the performance of the Ludwieg tube has been compared with the performance of a shock tube as a driver for the Ludwieg tube.

Concerning the range of unit-Reynolds number and Mach number, both the
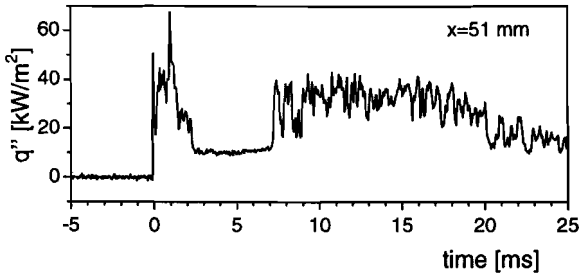
Figure A.9: Measured heat flux for a shock tube experiment at $x = 51$ mm from the leading edge of a flat plate ($Re_u = 3.89 \times 10^6$ $m^{-1}$, $T_5/T_1 = 1.43$, $p_4/p_1 = 7$, $M_5 = 0.33$ and $T_1 = 293$ K, Test section TS3).

Ludwieg tube and shock tube perform comparably. With both set-ups these two flow parameters can be varied independently. The shock tube even has a larger range available in the lower range of Reynolds numbers. However, these very low Reynolds numbers do not have an additional value, as can be seen in figure 3.4.

The available test time for the shock tube is 14 $ms$. About 3 $ms$ are required to obtain a steady flow. This results in an effective test time of 11 $ms$ compared to 50 $ms$ for the original Ludwieg tube. This implies that the latter set-up has about a 5 times more 'effective' test time than the shock tube. When these times are compared with the time scales of transition phenomena (the passage of a turbulent spot takes about 0.5 $ms$, in this flow regime), the shock tube test time is somewhat short, while the Ludwieg tube (two orders of magnitude above transition phenomena involved) supplies a sufficiently long test time. With respect to condition reproduction, both set-ups perform very well.

A difference in performance concerns the constancy of flow condition. With a slowly increasing pressure (10 %), the conditions in the shock tube are clearly less constant than the conditions in the Ludwieg tube (1% during 55 $ms$ for $M_t=0.33$). However, the heat flux levels in the Ludwieg tube are significantly lower than in the shock tube. First, the temperature difference (gas-wall) is coupled to the Mach number (depth of expansion), in contrast to the shock tube, in which the gas-to-wall temperature ratio can be varied independently. Second, the temperature difference is significantly smaller compared to the shock tube.

The conventional cold thin film technique should be improved using the Ludwieg tube set-up.

A very important matter is the control of free stream turbulence level. A proven technique is the application of an upstream turbulence grid that creates turbulence artificially. Considering the principle of shock-induced flows in the shock tube this will cause severe problems. Different shock reflections and interactions makes this turbulence generation technique very difficult. A second problem is caused by the fact that the natural turbulence level is in between 2% and 6% [*Trolier and Duffy*, 1985], which limits the range of turbulence level significantly on the lower side. The principle of flow generation in the Ludwieg tube is essentially different, making turbulence generating grids applicable as long as the area reduction of turbulence grid is less than that of the orifice.

With the creation of pressure gradients using contractions, some more freedom is obtained in the Ludwieg tube as well.

This comparison of experimental set-ups with respect to the adequacy for subsonic boundary layer transition research shows that the Ludwieg tube is a stronger candidate concerning test time, constancy of conditions and in the creation of free stream turbulence level. As a consequence of this conclusion the Ludwieg tube set-up was chosen to continue with.

# Appendix B

# Determination of flow conditions in test section TS3

Due to different orifice areas on the upper and lower side of the test section, test section TS3 will give rise to some difficulties with respect to flow condition determination. The Mach number above the plate is different from the Mach number on the lower side.

The pressure is recorded at only one location (above the plate). In order to compute the flow conditions at different locations in the test section, some extra information in the pressure signal had to be used.

The shock tube experiments were used, because this experiment gives the opportunity to make a distinction between different stages during the development of the flow. The expansion wave in the Ludwieg tube is too slow to observe the several stages. The thin film gauges are used to verify the computed propagation velocity of the reflected shock wave.

A typical pressure signal above the plate in the shock tube set-up is shown in figure B.1. Several stages can be recognized. At t= 0 $ms$ (stage a) the incident shock wave arrives. The pressure is instantaneously elevated to $p_2$. Due to the angle of the plate (2.0$^o$) the pressure rises somewhat as a result of weak shock reflections. The predicted pressure, $p_2$, corresponds very well with the pressure measured. The reflection of the incidental shock on the upper orifice causes the pressure $p_5'$ (stage b). This pressure peak is important. Because there is no any communication with the lower side, it is related to the Mach number on the upper side, $M_5'$. The $M_5'$ number is determined by fitting the theoretical pressure to the pressure obtained with the experiment, $p_5'$. The corresponding Mach number is the Mach number on the upper side. Its value is found to be equal to 0.33.

To verify this 'fit', the computed velocity of the reflected shock wave travelling over the plate is compared with the experimentally determined shock velocity, using the thin film gauges. In this comparison a difference of 2% was found.

Next, a drop to pressure $p_5$ is observed (stage c). This pressure is formed by
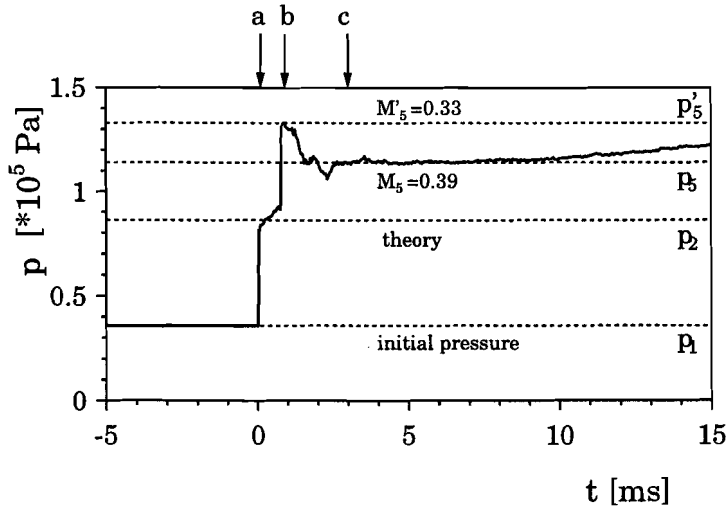
*Figure B.1: A typical pressure signal recorded above the plate in test section TS3. The different stages (indicated with a,b and c) are employed to determine the flow conditions above and in front of the plate.*

the 'effective' orifice area (which is a combination of the upper and lower area). Again the corresponding Mach number was determined. This results in a Mach number of 0.39. This value is somewhat higher than the upper Mach number because the lower area reduction is less.

The upstream Mach number of 0.39 determines the applied flow conditions like temperature, density and viscosity. This temperature is also related to the velocity above the plate.

These analyses were performed for different shock strengths and pressure levels, resulting in the same Mach numbers above and in front of the plate (the deviation is about 2%). Since an expansion wave is used in the Ludwieg tube, the several stages could not be recognized. However, the upstream Mach number was also found to be 0.39, which confirmed the value obtained with the shock tube.

With this method, the flow conditions in test section TS3 was determined with an accuracy that is satisfactory for this kind of geometry.

# Appendix C

# Pressure gauging and hot-wire anemometry

In this appendix the pressure gauging for the measurement of the static pressure during the experiment is briefly discussed, as well as the hot-wire anemometry for the free stream turbulence level measurements. This appendix concludes with a description of the data acquisition system applied.

## C.1 Pressure gauges

The static pressure at the tube wall is recorded with a quartz pressure transducer operated with a charge amplifier (Kistler 603B coated with a black Silastic 732 RTV coating). The resonance frequency is beyond 400 $kHz$ and has a rise time of 1 $\mu s$. The pressure gauge is calibrated carefully with a calibration set-up at several pressure levels and has a resolution of about 500 $Pa$.

## C.2 Hot-wire anemometry

Hot-wire anemometry (HWA) is applied to measure the turbulence intensity and relative mass flux variation during the test time [1]. The HWA is operated in constant temperature (CT) mode with a single wire perpendicular to the average velocity. The principle of the technique is based on measurement of the heat transfer from a thin hot wire towards the flow. In the case that it is possible to write the measured heat flux in terms of the instantaneous mass flux $\rho u$, turbulent fluctuations can be determined and consequently the turbulence level. In the range of experimental conditions ($0.09 < M < 0.5$ and $5.10^5 < Re_u <$

---

[1]The absolute mass flux rate is assumed to be known.
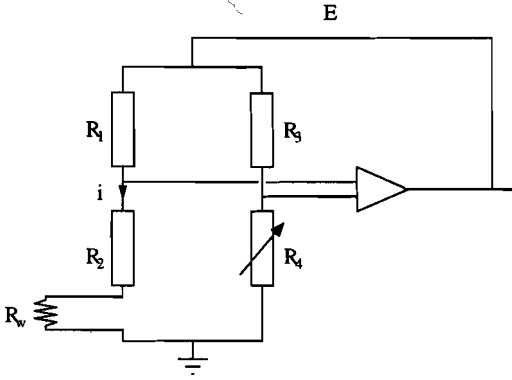
*Figure C.1: Diagram of the electrical circuit of the anemometer bridge.*

$2.10^7$) the heat transfer process is determined by forced convection only. The effects of radiative heat transfer and natural convection can be neglected, while instationary effects are eliminated by the CT-mode. Conductive losses at wire ends are less than [2] 15% for $l/d > 250$ and are eliminated in the calibration. Thus, the equilibrium is determined by the balance of heat production in the wire $P_{prod}$, and heat transfer by forced convection $P_{conv}$. The internal heat production is given by

$$P_{prod} = i^2 R_w = \frac{E^2 R_w}{(R_1 + R_2 + R_w)^2} \tag{C.1}$$

where $i$ is the electrical current through the wire, $R_w$ is the electrical resistance of the heated wire (figure C.1), $R_1$ is the anemometer bridge resistance, $E$ is the anemometer output voltage, and $R_2$ the probe (without wire) and cable resistance. The heat transfer due to forced convection is described by

$$P_{conv} = \pi k l \, (T_w - T_r) \mathcal{N}u \tag{C.2}$$

where $T_w$ is the temperature of the heated wire, $T_r$ is the recovery temperature (see equation 3.7), $k$ is the heat conductivity of fluid, $l$ is the wire length, and $\mathcal{N}u$ the Nusselt number. The Nusselt number is a function of the Reynolds number based on the wire diameter ($Re_d$), Prandtl number ($Pr$), Mach number ($M$), temperature loading factor ($\tau = \frac{T_w - T_r}{T_0}$ with $T_0$ the stagnation temperature), and $l/d$ ratio of the wire. As a result, $\mathcal{N}u = f(Re_d, Pr, M, \tau, l/d)$. At higher subsonic Mach numbers and a low wire-Reynolds number the flow can not be considered to be a continuum anymore. A useful dimensionless parameter in this range is the Knudsen number $Kn$, that relates the molecular mean free path to the object size and is given by

$$Kn = \frac{\lambda}{d} = \sqrt{\frac{\gamma \pi}{2}} \frac{M}{Re_d} \tag{C.3}$$

---

[2] For a 5 $\mu m$ tungsten wire and overheat ratio, $R_w/R_g$=1.8.

where $\lambda$ is the molecular mean free path, $d$ is the object dimension, $\gamma$ is ratio of specific gas heats, $M$ is the Mach number, and $Re_d$ is the Reynolds number based on object size. There will be a continuum flow for $Kn <0.01$, and free molecular flow if $Kn >1$, the range in between is the slip flow regime. For a 2.5 $\mu m$ wire, a Mach number of 0.36 and a unit-Reynolds number of $1 \times 10^6$ $m^{-1}$, the Knudsen number is 0.2 and thus in the slip flow regime.

The Knudsen number influences the heat transfer, which is represented by the Nusselt number. According to equation C.3 the Knudsen number is implicitly integrated into the list of parameters that influence the Nusselt number and is therefore taken into account in the calibration.

With the Ludwieg tube it is possible to keep $Pr, M, \tau, l/d$ and gas temperature constant, while $Re_u$ is varied as has been discussed in chapter 3. This implies that the Nusselt number in this experiment is a function of $Re_d$ only:

$$\mathcal{N}u = f(Re_d) \tag{C.4}$$

For the shape of this function King's law is frequently used [*Lomas*, 1986], which writes $\mathcal{N}u$ as

$$\mathcal{N}u = A + BRe^n \tag{C.5}$$

where $A$ and $B$ are empirical constants, and the exponent $n$ is chosen between 0.45 and 0.55. According to *Stainback and Nagabushana* [1993], *Fingerson and Freymuth* [1996] this relation may still be applied in the slip flow regime. The coefficients $A$ and $B$ can be different from the values found in the continuum flow regime.

In the calibration the gas temperature at constant Mach number is unchanged. Therefore, the dynamic viscosity is constant and the mass flux $\rho u$, may be written instead of $Re_d$. Using equations C.1, C.2 and C.5 and the knowledge that the recovery temperature is constant, a relation is obtained that is suitable for calibration purposes:

$$E^2 = \tilde{A} + \tilde{B}(\rho u)^n \tag{C.6}$$

where $\tilde{A}$ and $\tilde{B}$ are constants that must be determined from the calibration. These constants are specific to the Mach number under consideration. With this equation a relation between the measured heat transfer ($\propto E^2$) and the instantaneous mass flux $\rho u$, is obtained.

Figure C.2 shows a typical in-situ calibration example for a Mach number equal to 0.36, with a 2.5 $\mu m$-diameter wire at a constant overheat ratio of 1.7. The exponent $n$, is taken equal to 0.5. From this calibration the constants $\tilde{A}$ and $\tilde{B}$ are derived. According to *Bruun* [1995] the instantaneous mass flux may be calculated using equation C.6. An example was shown in figure 3.24. The probe voltage $E$, was measured with a sample frequency of 150 $kSamples/s$. The free stream turbulence level $Tu$, is calculated using the relation

$$Tu = \frac{\overline{(\rho u - \overline{\rho u})^2}^{1/2}}{\overline{\rho u}} \tag{C.7}$$
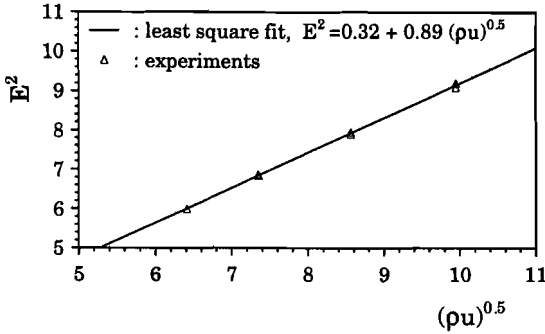
*Figure C.2: Calibration curve for constant Mach number and a varying unit-Reynolds number ($M=0.36$, $R_w/R_t=1.68$, $(T_{wire}-T_r) = 220[K]$, $d_{wire}=2.5\ \mu m$, grid1).*

where $\overline{\rho u}$ is the average over certain time space. Intervals of 1 *ms* were taken to eliminate effects introduced by the slightly changing mean flow as discussed in section 3.5. The average of all interval levels leads to the free stream turbulence level during a test run. The 12-bits resolution has been found to be sufficiently accurate, even for the lowest free stream turbulence level (a two times less accurate resolution resulted in an equal turbulence level).

For a representative measurement of the decaying turbulence in free stream flow, measurements should be performed up to the length scales that are still important. According to *Bruun* [1995] the wire length $l$, should be of the same length or smaller than the Taylor micro scale $\lambda$, which is defined as

$$\frac{\lambda}{L} = \left(\frac{15}{A}\right)^{1/2} Re_L^{-1/2} \qquad (C.8)$$

where $A \approx 1$ and $L$ is the largest eddy size or width of the flow ($L \approx 0.1\ m$). In the case that the wire length is smaller than half the Taylor micro scale ($l < \lambda/2$) the error in the measured free stream turbulence level should be smaller than 2%. Application to experimental conditions in the Ludwieg tube with $Re_u = 1.5 \times 10^6$ $m^{-1}$ and a flow width of 0.1 $m$, gives a Taylor micro scale $\lambda$ of about $1.0 \times 10^{-3}$ $m$. This implies that the hot-wire length must be 1 $mm$ or smaller. This was confirmed by an experiment with probe 1 ($l=2.5\ mm$) and probe 2 ($l=0.6\ mm$) at equal Mach and unit-Reynolds numbers. Whereas probe 2 shows a straight line in the inertial range, probe 1 shows a stronger decay. Eddies that participate in the energy spectrum and still contribute to the free stream turbulence level are not fully measured. This results in a lower free stream turbulence level (underprediction by 30 % compared to probe 2).

Another comparison concerns the effect of unit-Reynolds number on the power spectrum. An example is shown in figure C.3, representing an experiment with probe 2. The Mach number has been kept unchanged while two different unit-
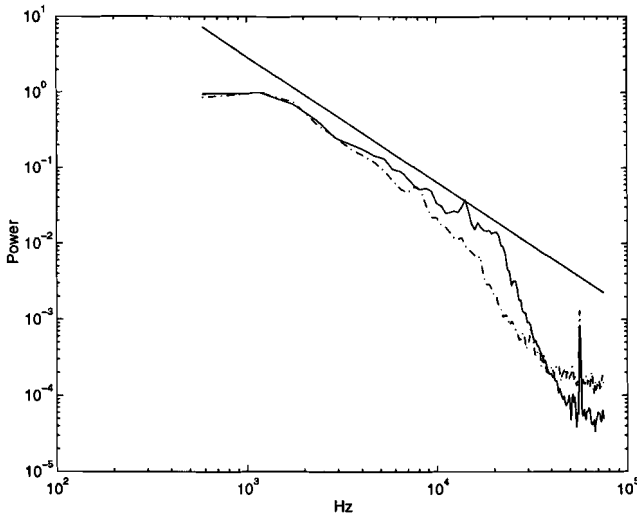
*Figure C.3: Power spectrum of ρu for different Reynolds numbers and equal Mach number (rescaled with respect to the maximum value). solid line: $Re_u = 2.4 \times 10^6$, dashed line: $Re_u = 6.9 \times 10^5$ (M=0.18, $R_w/R_t$=1.6, $T_w - T_r = 210[K]$, $d_{wire}$=2.5 μm, probe 2, grid 4).*

Reynolds numbers have been chosen. The solid line is the experiment with unit-Reynolds number equal to $2.4 \times 10^6$ $m^{-1}$. The (-5/3)-line (straight line above) is followed in the inertial range up to a frequency of 20 $kHz$, above this value the response frequency of the CT anemometer shows its limitations, resulting in a fast decay in power. The free stream turbulence level of this experiment is 4.7 %. The experiment with a more than three times lower unit-Reynolds number is presented by the dashed line. This experiment shows a faster decay compared to the less viscous experiment. This results in a lower free stream turbulence level ($Tu$=3.5 %). It should be noted that the differences in free stream turbulence are less pronounced at lower free stream turbulence levels (figure 3.25).

According to *Bruun* [1995] the response frequency of a CT anemometer is Reynolds number dependent. Lower Reynolds numbers give a lower response frequency. This can be observed in this experiment too.

It was verified whether the cut-off above 20 $kHz$ has some influence on the final free stream turbulence level measured. A numerical low-pass sharp cut-off filter was used that removed all frequencies above a certain frequency. The turbulence level obtained after filtering the frequencies above 8 $kHz$ already was 96% of the non-filtered turbulence level. This percentage increased to 98% at 10 $kHz$, which shows that the contents above 10 $kHz$ hardly contributes to the final free stream turbulence level. Therefore, it can be concluded that the limited response frequency of the CT anemometer has a negligible effect on the free stream turbulence level measured.
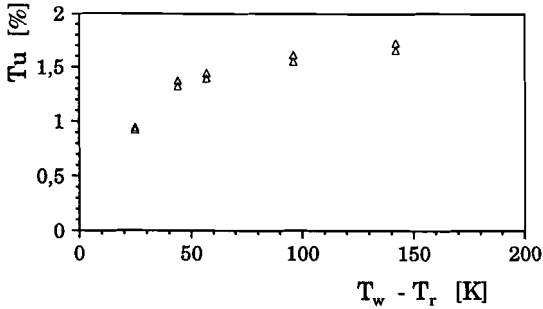
*Figure C.4: Effect of temperature difference $(T_w - T_r)$, on free stream turbulence level.*

With hot-wire measurements in compressible turbulent flow, the mass flux- and temperature fluctuations are always measured together. A property of the expanded flow in a Ludwieg tube is that gas temperature and grid temperature are different. As a result of heat transfer from grid to fluid, temperature fluctuations are introduced that can hardly be quantified. The sensitivity of the anemometer output voltage with respect to mass flux and temperature fluctuations can be strongly controlled by means of the temperature difference between hot-wire and gas flow [*Stainback and Nagabushana*, 1993, *Walker and Walker*, 1989]. The effective influence of the temperature difference on the free stream turbulence level was measured. This is shown in figure C.4. The free stream turbulence intensity obtained stabilizes for temperature differences above about 150 $K$. Therefore, all free stream turbulence measurements were performed at a temperature difference of at least 210 $K$.

The difference between mass flux variations and velocity fluctuations is very small. Estimations show that the velocity fluctuations should be less than 4% larger than the mass flux variations for a Mach number of 0.36. This difference can be neglected. For lower Mach number the difference should be even less.

## C.3   Data acquisition

Data were acquired with a data acquisition system consisting of a 486DX-PC with two different National Instruments I/O-boards. This system is controlled by a graphical interface: Labview. The first board (AT-MIO-64F-5) has 12 bits over a maximal range of $\pm 5$ $V$. Internal amplification with an adjustable gain between 0.5 and 100 extends the range from $\pm 50$ $mV$ (resolution is $2.44 \times 10^{-5}$ $V$) to $\pm 10$ $V$ (resolution is $4.88 \times 10^{-3}$ $V$). The gain error is $\pm 0.004\%$. A maximum of 64 single-ended channels can be monitored with a maximum sampling rate of 230 $ksamples/s$ (Bandwidth amplifier: -3$dB$ at 280 $kHz$). The off-set error is less than $\pm 10$ $\mu V$.

The second board (AT-MIO-16E1) has an equal range and number of gain factors as the former one. The maximum sampling rate is $1.25 MSamples/s$ and 16 single-ended channels can be read (Bandwidth amplifier: -3$dB$ at 1.6 $MHz$).

Futhermore, it is important to note that the scan frequency applied in measurements with test section TS3 was 20 $kHz$. This was the maximum frequency available at that time for 11 channels (board 2 was not yet available). To determine the arrival and departure of passing turbulent spots, the minimum required frequency is 20 $kHz$. Therefore, the low pass filter was designed to start from 30 $kHz$.

The electronic circuit applied in test section TS4 contained a low-pass filter from 30 $kHz$, which was half the measuring frequency. However, due to unstable behaviour during experiments the low-pass filter had to be removed. At that moment no time was left to build a new electronic system. For new experiments this will be done.

# Nomenclature

## Symbols

| | | |
|---|---|---|
| $A$ | Area | $[m^2]$ |
| $A$ | Fit constant | $[-]$ |
| $\tilde{A}$ | Calibration constant | |
| $b$ | Rod diameter | $[m]$ |
| $B$ | Fit constant | $[-]$ |
| $\tilde{B}$ | Calibration constant | |
| $c$ | Heat capacity | $[J/kgK]$ |
| $c$ | Velocity of sound | $[m/s]$ |
| $C$ | Constant | $[V]$ |
| $C_{le}$ | Ratio of leading edge velocity to $u$ | $[-]$ |
| $C_{te}$ | Ratio of trailing edge velocity to $u$ | $[-]$ |
| $C_{\pm}$ | Characteristics | |
| $d$ | Diameter | $[m]$ |
| $E$ | Voltage | $[V]$ |
| $F(\gamma)$ | Transformation function | |
| $g(H/w)$ | Function in heat conduction problem | $[-]$ |
| $h$ | Thin film thickness | $[m]$ |
| $H$ | Substrate thickness | $[m]$ |
| $i$ | Electrical current | $[A]$ |
| $k$ | Thermal conductivity | $[W/mK]$ |
| $Kn$ | Knudsen number | $[-]$ |
| $l$ | Length of thin film gauge or hotwire | $[m]$ |
| $L$ | Length between PG and far tube-end | $[m]$ |
| $L$ | Largest eddy size | $[m]$ |
| $L_t$ | Transition length | |
| | (between $\gamma = 0$ and $0.99$) | $[m]$ |
| $m$ | Mesh size | $[m]$ |
| $M$ | Mach number, $u/c$ | $[-]$ |
| $n$ | Normal direction | |
| $n$ | Turbulent spot production rate | $[1/ms]$ |
| $\hat{n}$ | Non-dimensional spot formation rate | $[-]$ |
| $\mathcal{N}u$ | Nusselt number | $[-]$ |
| $p$ | Pressure | $[N/m^2]$ |
| $P$ | Point in $(x, z, t)$-space | |
| $P$ | Power | $[W]$ |
| $Pr$ | Prandtl number | $[-]$ |
| $q^"$ | Heat flux per unit area | $[W/m^2]$ |
| $r$ | Recovery factor | $[-]$ |

| | | |
|---|---|---|
| $R$ | Cone of dependence | |
| $R$ | Electrical resistance | $[\Omega]$ |
| $R$ | Gas constant | $[J/kgK]$ |
| $Re$ | Reynolds number | $[-]$ |
| $Re_u$ | Unit-Reynolds number, $u/\nu$ | $[m^{-1}]$ |
| $R_1$ | Anemometer bridge resistance | $[\Omega]$ |
| $R_2$ | Probe (without wire) and cable resistance | $[\Omega]$ |
| $St$ | Stanton number | $[-]$ |
| $t$ | Time | $[s]$ |
| $T$ | Temperature | $[K]$ |
| $Tu$ | Free stream turbulence level, $(\sqrt{\overline{(\rho u - \overline{\rho u})^2}})/(\overline{\rho u})$ | $[\%]$ |
| $u$ | Free stream velocity | $[m/s]$ |
| $u'$ | Fluctuating velocity in x-direction | $[m/s]$ |
| $v'$ | Fluctuating velocity in y-direction | $[m/s]$ |
| $V$ | Volume | $[m^3]$ |
| $w$ | Thin film width | $[m]$ |
| $W$ | Substrate width per sensor | $[m]$ |
| $x$ | Stream-wise coordinate | $[m]$ |
| $y$ | Coordinate normal to surface | $[m]$ |
| $z$ | Lateral coordinate | $[m]$ |

## Greek symbols

| | | |
|---|---|---|
| $\alpha$ | Spreading angle | $[^o]$ |
| $\alpha$ | Plate angle | $[^o]$ |
| $\alpha$ | Temperature coeff. of $\chi$ | $[K^{-1}]$ |
| $\gamma$ | Intermittency | $[-]$ |
| $\gamma$ | Ratio of specific heats, $c_p/c_v$ | $[-]$ |
| $\gamma^*$ | Instantaneous intermittency | $[-]$ |
| $\delta$ | Boundary layer thickness | $[m]$ |
| $\delta$ | Thermal penetration depth | $[m]$ |
| $\delta^*$ | Boundary layer displacement thickness | $[m]$ |
| $\Theta$ | Boundary layer momentum thickness | $[m]$ |
| $\lambda$ | Transition length (between $\gamma$=0.25 and 0.75) | $[m]$ |
| $\lambda$ | Molecular mean free path | $[m]$ |
| $\lambda$ | Taylor micro scale | $[m]$ |
| $\lambda_\Theta$ | Pressure gradient parameter | $[-]$ |
| $\mu$ | Dynamic viscosity | $[Ns/m^2]$ |
| $\nu$ | Kinematic viscosity | $[m^2/s]$ |

| $\xi$ | Tolerance parameter | [-] |
|---|---|---|
| $\xi$ | Non-dimensional stream-wise coordinate | [-] |
| $\rho$ | Density | $[kg/m^3]$ |
| $\sigma$ | Spot propagation parameter | [-] |
| $\sigma$ | Solidity (ratio of grid area (blocked space) and tube area) | [-] |
| $\tau$ | Non-dimensional time, $(t - t_{le})/(t_{te} - t_{le})$ | [-] |
| $\tau$ | Temperature loading factor | [-] |
| $\chi$ | Resistivity | $[\Omega m]$ |

## Subscripts

| | |
|---|---|
| $b$ | Bottom |
| $conv$ | Convection |
| $diss$ | Dissipation |
| $e$ | End of transition, $\gamma$=0.99 |
| $exp$ | Experimental |
| $g$ | Gauge |
| $i$ | Initial condition |
| $l$ | Laminar |
| $le$ | Leading edge of turbulent spot |
| $m$ | Measured |
| $or$ | Orifice |
| $prod$ | Production |
| $r$ | Recovery |
| $s$ | Slot |
| $s$ | Surface |
| $sub$ | Substrate |
| $t$ | Test condition in tube |
| $te$ | Trailing edge of turbulent spot |
| $tr$ | Start of transition, $\gamma$=0 |
| $turb$ | Turbulent |
| $w$ | Wall |
| 0 | Reference situation |
| 1 | Initial situation in LPS |
| 2 | Situation between contact surface and incidental shock wave |
| 3 | Situation between expansion wave and contact surface |
| 4 | Initial situation in HPS |
| 5 | Situation after reflected shock wave |

## Abbreviations

| | |
|------|----------------------------|
| CP   | Constant property          |
| CP   | Constant property          |
| CT   | Constant temperature       |
| D    | Diaphragm                  |
| DT   | Dump tank                  |
| GC   | Gas cylinder               |
| HPS  | High pressure section      |
| LPS  | Low pressure section       |
| MM   | Mano meter                 |
| O    | Orifice                    |
| PG   | Pressure gauge             |
| RTD  | Resistance temperature device |
| T    | Tube                       |
| TS   | Test section               |
| V    | Valve                      |
| VP   | Vacuum pump                |

# Summary

The work presented in this thesis focuses on heat transfer measurements in transitional boundary layers. Since the heat transfer rates are strongly related to the type of boundary layer, there is a great demand for knowledge on transition under the conditions typical for the flow in gas turbines. Limited knowledge is available on the influence on the transition process of high levels of free stream turbulence ($1\% < Tu < 10\%$) and higher subsonic Mach numbers ($0.3 < M < 1.0$). These conditions feature turbine flow.

A facility that can be used for this purpose, is the so-called Ludwieg tube. Up till now this kind of facility has not been used for experiments on boundary layer transition in subsonic flows. In the present study it was shown that it is possible to perform accurate transition experiments with a Ludwieg tube. This set-up generates a well-defined flow using gasdynamical waves. The reproduction accuracy of the flow conditions is very high, and the conditions during each experiment are constant. Furthermore, it is possible to vary the unit-Reynolds number, Mach number, and free stream turbulence level independently over a wide range. The test time available ($\approx 50\ ms$) is long enough to perform accurate transition experiments. In comparison to the Isentropic Light Piston Tunnel, the conditions in the Ludwieg tube are more constant, whereas the costs of the set-up are several times less. A disadvantage of the Ludwieg tube is the relatively low heat flux level, leading to less accurate heat transfer measurements. For this reason the existing cold thin film heat flux measuring technique was improved. With the optimization strategy a significant improvement was obtained with respect to the signal-to-noise ratio.

Experiments from literature show that the geometrical shape of a turbulent spot is self-similar. From the heat transfer measurements performed at the wall, it turned out that there is also a self-similarity for the heat flux. Besides that, the calmed region appears to play an essential role in the total heat flux of an individual turbulent spot.

The data set available in literature regarding transition measurements on a flat plate subjected to a subsonic Mach number and free stream turbulence level was extended. From the literature, data are available at a Mach number equal to about 0.2 with a free stream turbulence level of 1.3%, and these values are elevated to a flow with $M=0.36$ and $Tu=4.0\%$. For these Mach numbers a negligible influence of compressibility is found on the spot propagation, spot growth, spot formation rate, transition length, and transition onset. The transition onset is strongly dependent on the free stream turbulence level. A higher turbulence intensity leads to earlier transition. It is concluded from the present experiments that the transition onset is not affected by the turbulence level only, but also by the turbulence structure generated by a specific grid.

# Samenvatting

Het onderzoek in dit proefschrift richt zich op warmteoverdrachts metingen in grenslagen. Omdat de warmteoverdracht sterk gekoppeld is aan het karakter van de grenslaag is er dringend behoefte aan kennis over transitie voor de condities die karakteristiek zijn voor de stroming in gas turbines. Er is weinig bekend over de invloed op het transitie proces van een aanstroming met hoge turbulentie intensiteit en bij hogere subsone Mach getallen. Juist deze condities kenmerken de stroming in gas turbines.

In dit werk wordt voor het eerst een Ludwieg buis voor dit doel gebruikt. Er wordt aangetoond dat het mogelijk is nauwkeurige transitie experimenten uit te voeren met deze opstelling. De reproduceerbaarheid van de stromings condities is zeer goed en de condities zijn constant. Verder kan het eenheids-Reynolds getal, het Mach getal en het turbulentie niveau van de hoofdstroming over een groot bereik onafhankelijk worden gevarieerd. De beschikbare test tijd ($\approx$ 50 $ms$) is voldoende lang om nauwkeurige transitie experimenten uit te voeren. In vergelijking met de Isentropic Light Piston Tunnel zijn de condities in de Ludwieg buis constanter, terwijl de kosten van de opstelling enkele malen lager zijn. Een nadeel van de Ludwieg buis is de relatief lage warmteoverdracht. Dit levert een minder nauwkeurige warmteoverdrachts meting op. Daarom is de bestaande warmteoverdrachts meettechniek met 'cold thin film gauges' verbeterd. Zo is de signaal ruis verhouding wezenlijk verbeterd.

Experimenten uit de literatuur geven een geometrische gelijkvormigheid van de 'turbulent spot' te zien. Het blijkt uit de verrichte warmteoverdrachts metingen aan de wand dat ook de warmteoverdracht gelijkvormig is. De 'calmed region' speelt een wezenlijke rol in de warmteoverdracht van een individuele turbulent spot. De beschikbare data in de literatuur over transitie metingen aan een vlakke plaat, bij subsone Mach getallen en hoge aanstroom turbulentie intensiteit, zijn uitgebreid. Vanaf een stroming met een Mach getal van ongeveer 0.2 met een turbulentie niveau van 1.3 % zijn de waarden opgevoerd tot $M$=0.36 en $Tu$=4.0 %. Voor deze Mach getallen is er een verwaarloosbare invloed van compressibiliteit gevonden op de spot voortplanting, spotgroei, spotproduktie, transitielengte en transitiestart. De huidige experimenten geven aan dat de transitiestart niet alleen wordt beinvloed door het turbulentie niveau, maar ook door de turbulentiestruktuur gegenereerd door specifieke grids.

# Nawoord

Veel gaat er vooraf aan het schrijven van een proefschrift. Het is niet alleen de promovendus die zorgt voor de afronding. Velen hebben hierin een bijdrage geleverd. Allereerst bedank ik Anton voor zijn stimulerende werkwijze. Veel dank ben ik verschuldigd aan Rick. Zijn pragmatische manier van aanpak is erg leerzaam geweest. Een zeer grote bijdrage werd geleverd door de sectie Gasdynamica en Aeroakoestiek van de faculteit Technische Natuurkunde. Ik dank Rini hartelijk voor het ter beschikking stellen van de expertise en diverse experimentele opstellingen. De samenwerking met zijn groep was altijd uiterst plezierig. Verder hebben zijn kritische opmerkingen veel toegevoegd aan het proefschrift. Jan Willems en Harm de Jager wil ik dank zeggen voor hun nooit aflatende behulpzaamheid bij de experimenten met de schok- en Ludwiegbuizen. Steeds kon ik terug vallen op hun brede ervaring.

Prof. van Heijst en prof. Nieuwstadt dank ik voor het werk dat zij verrichtten als leden van de kerncommissie. Verder dank ik Rian en Marjan die op het secretariaat een centrale post innemen. Ook ben ik dank verschuldigd aan Frits, Peter, Lambert en Ad.

Veel werk is verzet door studenten in het kader van het afstuderen of een stage. Antoine, Rene, Bart, Johan van den Oever, Johan Barel, Remco, Victor, Bas, Ron en Martin dank ik allen voor hetgeen zij gedaan hebben.

Binnen de sectie heerste een prettige werksfeer. Dat kwam bijvoorbeeld tot uitdrukking in de vele goede discussies met mijn collega's. Apart vermeld ik Peter Minev. Ik denk met plezier terug aan de vaak diepvoerende gesprekken. Ook de collega's van de gezellige lunch groep Jacob, Rob Bastiaans, Jos, Rob Schook, Douwe, Gert en Ton bedank ik voor de vaak levendige discussies. Hierbij noem ik ook Wim van Leeuwen. Onder de menige kilometers die we als carpoolers aflegden kwamen regelmatig nieuwe ideeen naar boven.

Buiten mijn werkomgeving speelden ook mijn ouders, broer en zussen een rol met hun voortdurende belangstelling. Zeer groot is het aandeel geweest van mijn vrouw Trijntje. Haar continue ondersteuning was zeer belangrijk, met name in de laatste maanden.

Maar boven alles heeft God alles aangedragen wat nodig was zodat ik mijn werk kon verrichten. Voor deze daden schieten eigen woorden tekort.

Jankees Hogendoorn                                   Wijk en Aalburg, maart 1997.

# Curriculum vitae

| | |
|---|---|
| 4 juni 1970 | Geboren te Rotterdam |
| 1982–1988 | VWO-B |
| | Willem van Oranje College te Waalwijk |
| 1988–1993 | TU werktuigbouwkunde |
| | Technische Universiteit Eindhoven |
| 1993–1997 | Assistent in Opleiding |
| | binnen de sectie |
| | Werktuigkundige Energietechnologie |
| | Technische Universiteit Eindhoven |
| 1997– | Krohne Altometer te Sliedrecht |

Stellingen


behorende bij het proefschrift


HEAT TRANSFER MEASUREMENTS
IN SUBSONIC
TRANSITIONAL BOUNDARY LAYERS


van


C.J. Hogendoorn

I. De Ludwieg buis is een geschikte experimentele opstelling voor nauwkeurig onderzoek naar grenslaag transitie bij subsone stromingen met hoge aanstroom turbulentie intensiteit. (Dit proefschrift)

II. Omdat de 'calmed region' een essentiële bijdrage levert in de warmte-overdracht veroorzaakt door een 'turbulent spot', dient deze te worden meegenomen in de modelvorming. (Dit proefschrift)

III. Voor de dissipatie flux in een koude-dunne-film-sensor geldt dat niet de absolute waarde (Epstein en Guenette, 1986), maar de verandering tijdens de meting, het criterium vormt voor de toelaatbare dissipatie. (Dit proefschrift)

IV. Het welslagen van experimenteel onderzoek is sterk afhankelijk van het goed op elkaar afstemmen van verschillende meettechnieken. (Dit proefschrift)

V. Daar het eigenlijke doel al te gemakkelijk uit het oog wordt verloren, geldt met name voor het gebruik van CFD: 'Bezint eer ge begint'.

VI. Een voorwaarde voor het gebruik van alternatieve energie op grote schaal is het economisch voordeliger zijn of de verplichting tot het gebruik er van.

VII. Wat men hoort is met de huidige techniek niet te voorspellen.
(o.a. Reformatorisch Dagblad, 5 april 1997)

VIII. Het uitlaten van honden is een duistere activiteit.

IX. De structuur van orgelcomposities heeft zich na de 18e eeuw niet verder verdiept.

X. De taak van huisvrouw in een gezin wordt ten onrechte sterk ondergewaardeerd. Dit werk is niet alleen zwaar maar vormt bovendien een van de bouwstenen van de samenleving.

XI. De Nederlandse benaming van getallen boven de 20 leidt tot verwarring en kan beter worden vervangen door het Engelse model.